الجمهورية الجزائرية الديمقراطية الشعبية

People's Democratic Republic of Algeria

وزارة التعليم العالي والبحث العلمي

Ministry of Higher Education and Scientific Research

Ziane Achour University of Djelfa

Faculty of Exact Sciences and Computer Science

Physics department

Order n°:……

THESIS

presented to obtain

3rd Cycle doctoral degree

Option: Physics

Specialty: Materials Physics

Presented by:

DJALAB Yacine

Study of the physical properties of zinc-based semiconductors $ZnO_{1-y}X_y$ (X=S, Se, Te), for optoelectronic applications.

Defended on: 26 / 06 /2024

Jury members:

First & Last name	**Degree**	**Institution**	**Role**
KHARROUBI Mohamed	Prof.	University of Djelfa – Ziane Achour	President
MOUSSA Rabah	MCA	University of Djelfa – Ziane Achour	Supervisor
MAACHE Mostefa	Prof.	University of Djelfa – Ziane Achour	Co-Supervisor
GUEDDOUH Ahmed	Prof.	University of Laghouat – Amar Telidji	Examiner
DEROUICHE Yazid	Prof.	University of Djelfa – Ziane Achour	Examiner
BOUREZG Yousf Islem	MCA	University of M'Sila – Mohamed Boudiaf	Examiner

University year: 2023/2024

Dedication

To my beloved parents

To my brothers and sisters

To my friends and all those who are dear to me

Yacine

Acknowledgement

I would like to thank first of all our God, **ALLAH** the Almighty, who is always with me in the easy and difficult moments of life.

The research work developed in this thesis was carried out within the Physico-Chemistry of Materials and Environment Laboratory (**LPCME**) at Ziane Achour University, Djelfa.

I would like to express my deep gratitude and warm thanks to **Dr. RABAH Moussa**, professor at Ziane Achour University, Djelfa for agreeing to direct my work. I thank him for his advice and his human qualities, his scientific and fruitful discussions. He never deprives me of his support, whether technical or material.

My most sincere thanks also go to **Prof. MAACHE Mostafa**, professor at Ziane Achour University, Djelfa, who, by acting as co-director, greatly enriched my work. His advice and comments have been very useful. I also thank him for his constant availability and support during these years. I could not have asked for better PhD supervisors.

I would also like to offer my thanks, my respect and my gratitude to **Prof. KHARROUBI Mohamed,** professor at University of Ziane Achour, Djelfa for the honor he gave me, for agreeing to chair the jury.

I also wish to offer my thanks and sincere appreciation to **Prof. GUEDDOUH Ahmed**, professor at University of Amar Telidji, Laghouat, **Prof. DEROUICHE Yazid**, professor at University of Ziane Achour, Djelfa, **Dr. BOUREZG Yousf Islem**, professor at University of Mohamed Boudiaf, M’Sila who agreed to examine and judge this modest work.

Finally, I truly want to thank my parents, relatives, friends and all those who have contributed directly or indirectly to the accomplishment of this work.

Abstract

In this thesis, the structural, electronic, optical and elastic properties of the ternary alloys $ZnO_{1-x}S_x$, $ZnO_{1-x}Se_x$ and $ZnO_{1-x}Te_x$ for x = 0.25, 0.5 and 0.75 were studied theoretically, as well as their binary constituents ZnO, ZnS, ZnSe and ZnTe. The wurtzite crystal structure was the primary focus of this study. The Wien2k package, which is based on the full-potential linearized augmented plane wave (FP-LAPW) approach within the confinements of density functional theory (DFT), was utilized to perform the calculations. The exchange-correlation potential was addressed using the local density (LDA), Wu-Cohen (WC-GGA) and Perdew-Burke-Ernzerhof (PBE-GGA) approximations. More precise electronic properties calculations were made using the Becke-Johnson potential (TB-mBJ) method.

In terms of the structural properties, we discover that the bulk modulus and lattice constants deviates slightly from Vegard's law. Additionally, the electronic properties show that the materials under study have improved bandgap energy values using (TB-mBJ) approximation. Also, our findings demonstrate that every material under investigation is a semiconductor with direct bandgap. Furthermore, the optical parameters curves shift toward lower energies as the composition x increase. We also came to the conclusion that every material under study satisfies the stability criteria and is elastically stable in the Wurtzite structure.

Keywords: ZnO, Semiconductors, DFT, FP-LAPW, Wien2k, Ab-initio, Ternary alloys.

Résumé

Dans cette thèse, les propriétés structurales, électroniques, optiques et élastiques des alliages ternaires $ZnO_{1-x}S_x$, $ZnO_{1-x}Se_x$ et $ZnO_{1-x}Te_x$ pour x = 0.25, 0.5 et 0.75 ont été étudiées théoriquement, ainsi que leurs constituants binaires ZnO, ZnS, ZnSe et ZnTe. La structure cristalline de la wurtzite était au centre de cette étude. Le package Wien2k, basé sur l'approche d'onde plane augmentée linéarisée à potentiel totale (FP-LAPW) dans les limites de la théorie fonctionnelle de la densité (DFT), a été utilisé pour effectuer les calculs. Le potentiel de corrélation d'échange a été abordé à l'aide de l'approximations de la densité locale (LDA), de Wu-Cohen (WC-GGA) et de de Perdew-Burke-Ernzerhof (PBE-GGA). Des calculs plus précis des propriétés électroniques ont été effectués à l'aide de la méthode du potentiel de Becke-Johnson (TB-mBJ).

En termes de propriétés structurelles, nous découvrons que le module de compressibilité et les paramètres de maille s'écartent légèrement de loi de Vegard. De plus, les propriétés électroniques montrent que les matériaux étudiés ont amélioré les valeurs d'énergie de bande interdite en utilisant l'approximation (TB-mBJ). En outre, nos résultats démontrent que chaque matériau étudié est un semi-conducteur à bande interdite directe. De plus, les courbes des paramètres optiques se déplacent vers des énergies plus basses avec l'augmentation de composition x. Nous sommes également arrivés à la conclusion que chaque matériau étudié satisfait aux critères de stabilité et est élastiquement stable dans la structure Wurtzite.

Mots-clés: ZnO, Semiconducteurs, DFT, FP-LAPW, Wien2k, Ab-initio, Alliages ternaires.

ملخص

في هذه الأطروحة، أجرينا دراسة نظرية حول الخصائص البنيوية والإلكترونية والبصرية والمرونية للسبائك الثلاثية $ZnO_{1-x}S_x$، $ZnO_{1-x}Se_x$ و$ZnO_{1-x}Te_x$ من أجل $x = 0.25, 0.5, 0.75$ بالإضافة إلى مركباتهم الثنائية ZnO، ZnS، ZnSe وZnTe. طبقت هذه الدراسة في البنية البلورية السداسية المعروفة باسم wurtzite. تمت هذه الحسابات باستخدام طريقة الأمواج الخطية المزيدة (FP-LAPW) وذلك باستعمال برمجية wien2k في إطار نظرية الكثافة الدالية (DFT). من أجل كمون التبادل والتعالق، تم استخدام تقريب الكثافة المحلية (LDA)، والتقريبين المبنيين على تقريب التدرج المعمم (PBE-GGA) و (WC-GGA). تم كذلك استعمال تقريب (TB-MBJ) لحساب الخواص الالكترونية بدقة أكبر.

بالنسبة للخصائص البنيوية، نلاحظ أن المواد التي درسناها تظهر انحرافًا عن قانون فيجارد بالنسبة لثوابت الشبكة ومعامل الانضغاطية. أيضاً في الخصائص الإلكترونية، يمكننا ملاحظة أن قيم طاقة الفجوة الطاقية للمواد قد تم تحسينها بواسطة تقريب (TB-MBJ). ووفقًا لحسابتنا، جميع المواد المدروسة هي شبه موصلات ذات فجوة طاقية مباشرة. علاوة على ذلك، منحنيات الثوابت البصرية تنتقل نحو الطاقات الأدنى مع زيادة التركيز x. وفي الأخير، خلصنا إلى أن شروط الاستقرار لجميع المواد المدروسة تمت الامتثال لها وأنها مستقرة مرونياً في البنية السداسية.

الكلمات المفتاحية: أكسيد الزنك، أشباه الموصلات، DFT، FP-LAPW، Wien2k، Ab-initio، السبائك الثلاثية.

Table of content

List of figures

List of tables

General Introduction

Scientists worldwide have shown a keen interest in Group II-VI semiconductors, thanks to their potential to replace Group III-V semiconductors in a wide array of applications, especially in the optoelectronic industry. These semiconductors, characterized by their large bandgap, hold promise in the development of optoelectronic devices designed to function within the blue to near-ultraviolet (UV) spectrum. Among this class of compounds, particular attention has been devoted to exploring the applications of the zinc oxide (ZnO) binary compound. Zinc oxide stands out as a material of extensive study due to its flexibility. It is the perfect material for a variety of optoelectronic applications because of its unique qualities, which include a wide bandgap of 3.37 eV at 300 K, a substantial exciton binding energy of 60 meV, exceptional optical conductivity, susceptibility to easy surface modification in both acids and alkalis, piezoelectric attributes, and a high electron mobility of 300 cm^2/Vs **[1-2]**. These applications include solar cells, light-emitting diodes, UV lasers, transparent thin-film transistors, transparent electrodes, and even medicinal applications **[3-7]**. Although the ZnO compound is metastable in the wurtzite crystalline phase WZ (B4) at ambient conditions, it may also form other crystal structures, such as rocksalt RS (B1) and zinc blende ZB (B3), when subjected to high strain on a cubic substrate **[3]**. The stable wurtzite structure for ZnO is confirmed by first principle investigations, and the equilibrium transition energy between both WZ (B4) and RS (B1) phases is found to be between 8.22 and 15 GPa **[8-12]**. The ZnO bandgap needs to be adjusted to take visible and UV light emissions into consideration. Consequently, attempts are being undertaken to design ZnO-based materials' bandgap.

Semiconductor materials often require bandgap engineering to align with specific application requirements, and alloying serves as a commonly employed technique for this purpose. An illustrative example involves substituting magnesium ‘Mg’ for zinc ‘Zn’, a method that results in the ternary alloy Mg_xZnO_{1-x}. This alloy exhibits an increasing bandgap as the magnesium content rises **[13-14]**. On the other hand, the elaboration and characterization of the $Cd_yZn_{1-y}O$ ternary alloy demonstrate that its bandgap energy decreases as the composition of cadmium ‘Cd’ increases, rendering it a promising choice for optical and solar cell applications **[13,15]**. Nevertheless, the toxicity associated with cadmium necessitates the exploration of alternative materials. One such alternative resides in chalcogenide atoms, namely sulfur ‘S’ selenium ‘Se’ and tellurium ‘Te’. The alloys $ZnO_{1-x}Y_x$ (where Y=S, Se, and Te) belong to the category of highly mismatched alloys (HMAs). These alloys involve substituting ‘O’ with chalcogenide atoms, which are notably larger and less electronegative than ‘O’ atoms. This substitution perturbs the band structure, offering distinct possibilities. However, synthesizing such HMAs can prove challenging due to the disparities in atomic size and electronegativity.

$ZnO_{1-x}S_x$, a ternary semiconductor with a wide bandgap, has recently piqued the interest of researchers. With a substantial energy band gap ranging from 2.60 eV to 3.60 eV **[16-17]**. $ZnO_{1-x}S_x$ has become a competitive alternative to toxic CdS in n-type window/buffer components for solar cells due to its n-type conductivity. In fact, it has been effectively used as a pane layer in solar cells based on CIG/CIGS **[18-19]**, CIG/CZTS **[20-21]** and SnS **[22-23]**, leading to improved solar cell performance.

Numerous theoretical investigations into $ZnO_{1-x}Se_x$ alloys have been documented **[24-26]**. These studies explore the impact of selenide atomic compositions on the structural and optical properties of ternary $ZnO_{1-x}Se_x$ alloys using the DFT method implemented through the VASP package and the partially self-consistent $scGW_0$ approach **[25]**. These findings reveal the potential to tailor the bandgap of $ZnO_{1-x}Se_x$ ternary alloys to suit solar cell and energy applications. Moreover, experimental growth of $ZnO_{1-x}Se_x$ ternary alloys has been achieved through radical source molecular beam epitaxy (RS-MBE) **[27]**. Additionally, the pulsed laser deposition technique (PLD) has been employed to deposit $ZnO_{1-x}Se_x$ films with varying selenium compositions on sapphire substrates (001).

$ZnO_{1-x}Te_x$ thin film compounds have been the subject of early research by Sánchez **[28-29]**, which has demonstrated the viability of doping ZnO with ‘Te’ mole fractions in the wurtzite structure. This study also raises the possibility of the formation of other ‘Te’ solid phases with higher ‘Te’ contents, which would lower the bandgap by incorporating ‘Te’ atoms into the ZnO crystal structure. Moreover, using molecular beam epitaxy (MBE), significantly discordant $ZnO_{1-x}Te_x$ alloys have been produced, exhibiting critical characteristics for solar cell applications. The temperature dependence of the bandgap energies was assessed using the photoreflectance technique **[30]**. Absorption measurements reveal that the optical bandgap of $ZnO_{1-x}Te_x$ ($x>0.34$) alloys decreases with an increase in Tellurium content **[31]**.

Ab-initio calculations are highly effective techniques that accelerate the process of discovering new materials, enhancing material performance, and deepening our comprehension of the fundamental aspects of the physical world. Density Functional Theory (DFT) occupies a significant position among the ab-initio methodologies that are driving advancements in the field of solid-state physics. The approach, originally formulated by Hohenberg, Kohn, and Sham between 1964 and 1965, and subsequently recognized with the Nobel Prize in 1998 awarded to W. Cohen, presents numerous benefits. The method is known for its easy integration, its ability to provide accurate predictions across diverse materials, and its suitability for extensive systems. Therefore, Density Functional Theory (DFT) has become an essential and powerful tool in scientific research, demonstrating its usefulness across various branches of physics, such as condensed matter physics, liquid studies, plasma research, surface analysis, and nanostructures. Additionally, (DFT) has extended its impact into interdisciplinary fields like biology and chemistry.

The extensive utilization of Density Functional Theory (DFT) has been closely associated with the advancements in massively parallel computing that have occurred in recent times. Consequently, modern science has the capacity to manipulate a multitude of atoms in their computations through the use of efficient algorithms on high-performance computing clusters, thereby creating novel opportunities for exploration and invention.

This thesis aims to improve understanding of the structural, electronic, and optical characteristics of the binary elements ZnO, ZnS, ZnSe, and ZnTe as well as the ternary alloys $ZnO_{1-x}S_x$, $ZnO_{1-x}Se_x$, and $ZnO_{1-x}Te_x$. This will be accomplished out via a theoretical study that makes use of density functional theory (DFT) and the full potential linearized augmentation plane wave technique (FP-LAPW). Following this introductory section, the thesis is structured into three distinct chapters. In the first chapter, an extensive bibliographic investigation is conducted, where we define the materials under study and their physical properties are discussed. The second chapter discusses the use of density functional theory (DFT) and introduces the ab-initio approach (FP-LAPW) as a means to investigate the properties of the materials under consideration. Also, we have provided a comprehensive description of the various approximations employed, as well as an overview of the Wien2k code. In the third chapter, the results of our computational calculations regarding to the properties of the binary compounds and the ternary alloys were presented. Finally, the key findings obtained are summarized in a general conclusion.

References

[1] Y Liu et al., **Mater. Lett.** 62 (17), 2783 (2008).
[2] T Yang et al., **ACS Sensors** 2 (7), 1051 (2017).
[3] Ü Özgür et al., **J. Appl. Phys.** 98 (4) (2005).
[4] V Pawar et al., **Phys. Rev. Appl.** 9 (5), 054001 (2018).
[5] A Sáenz-Trevizo et al., **Mater. Res.** 19, 33 (2016).
[6] A Samavati et al., **J. mater. sci. eng., B** 263, 114811 (2021).
[7] M Sowjanya et al., **Acta Phys. Pol. A** 137 (3) (2020).
[8] S Limpijumnong and S Jungthawan, **Phys. Rev. B** 70 (5), 054104 (2004).
[9] K Sarasamak et al., **Phys. Rev. B** 82 (3), 035201 (2010).
[10] SZ Karazhanov et al., **Phys. Rev. B** 75 (15), 155104 (2007).
[11] H Liu et al., **Phys. Rev. B** 71 (21), 212103 (2005).
[12] MK Yaakob et al., **Integr. Ferroelectr.** 155 (1), 15 (2014).
[13] T Makino et al., **Appl. Phys. Lett.** 78 (9), 1237 (2001).
[14] S Choopun et al., **Appl. Phys. Lett.** 80 (9), 1529 (2002).
[15] K Sakurai et al., **J. Cryst. Growth** 237-239, 514 (2002).
[16] L Zhang et al., **J. Alloys Compd.** 617, 413 (2014).
[17] BK Meyer et al., **Appl. Phys. Lett.** 85 (21), 4929 (2004).
[18] T-M Hsieh et al., **J. Power Sources** 246, 443 (2014).
[19] C Bugot et al., presented at the 2015 IEEE 42nd Photovoltaic Specialist Conference (PVSC), 2015 (unpublished).
[20] HK Hong et al., **Sol. Energy Mater. Sol. Cells** 155, 43 (2016).
[21] KX Steirer et al., **Phys. Chem. Chem. Phys.** 17 (23), 15355 (2015).
[22] P Sinsermsuksakul et al., **Appl. Phys. Lett.** 102 (5) (2013).
[23] HH Park et al., **Prog Photovolt** 23 (7), 901 (2015).
[24] M Rashid et al., **Chin. Phys. B** 22 (8), 087301 (2013).
[25] G Baldissera and C Persson, **J. Appl. Phys.** 119 (4) (2016).
[26] R Manotum et al., **J. Electron. Mater.** 46 (12), 6856 (2017).
[27] K Iwata et al., **J. Cryst. Growth** 251 (1), 633 (2003).
[28] O Sánchez et al., **MRS Adv.** 2 (53), 3111 (2017).
[29] O Sánchez and M Hernández-Vélez, **Coatings** 11 (5), 570 (2021).
[30] T Tanaka et al., **J. Appl. Phys.** 125 (24) (2019).
[31] M Ting et al., **J. Appl. Phys.** 125 (15) (2019).

Chapter I Literature about ZnO-based semiconductor alloys

I.1 Introduction

II-VI semiconductors gained the interest of researchers due to their prominent optoelectronic properties. Some common II-VI semiconductors include zinc oxide (ZnO), magnesium oxide (MgO), cadmium sulfide (CdS) and zinc selenide (ZnSe). Because of their wide bandgap, these semiconductors are beneficial for making optoelectronic devices that operating in the blue to near ultraviolet (UV) range such as transistors, photodetectors, conducting films, light emitters, sensors, …etc **[1-4]**.

Due to its wide range of applications, the ZnO binary compound is one of the most studied materials. Its unique characteristics, such as its wide bandgap of 3.33 eV at room temperature, low toxicity, high electron mobility of 300 $cm^2/V.s$, high melting temperature of 2248 K, and large piezoelectric constants, make it ideal for a number of optoelectronic applications, including transparent thin film transistors, transparent electrodes, solar cells, and light-emitting diodes **[5-9]**.

In semiconductor materials, alloying is one of the most common methods for improving electronic, optical and other properties via changing the structural/lattice parameters and therefore tailoring the bandgap to meet specific application requirements. For instance, the study of substituting zinc (Zn) with magnesium (Mg) has shown that the band gap of the ternary alloy Mg_xZnO_{1-x} widens as the composition of 'Mg' increases **[10-11]**. Additionally, it was discovered during the development and characterization of the $Cd_yZn_{1-y}O$ ternary alloy that the band gap energy reduced as the amount of cadmium (Cd) increased **[10,12]**. This ternary alloy is well suited for optical and solar applications. However, because the cadmium is toxic atom, it is critical to find other materials.

In this first chapter, the basic concepts of semiconductors formed from elements II-VI of the periodic table will be presented in a manner as simple as possible so that they can be understood and translated into measurable quantities. Also, we give a brief description to the fundamental properties of $ZnO_{1-x}S_x$, $ZnO_{1-x}Se_x$ and $ZnO_{1-x}Te_x$. Specifically, how the structure, electronic, and optical properties of semiconductors change as a function of composition x under normal conditions.

I.2 Generalities on II-VI semiconductors

The II-VI semiconductors are compounds formed from elements of groups II and VI of the periodic table, they have properties very similar to those of compounds of groups III-V and IV. Furthermore, they are known for their direct wide bandgap and come with a variety of lattice constants. They mainly exhibit an ionic bond, which is caused by the transfer of electronic charge from atoms in group II to atoms in group VI. As a result, the coulomb interaction between the ions increases, as does the energy gap in the electronic band structure. Due to these factors, it has become increasingly popular in recent years to use II-VI semiconductors for optoelectronic applications in the blue to near ultraviolet ranges.

I.2.1 Crystal structure

Like other II-VI semiconductors, compounds formed from Zinc (Zn) on the one hand and chalcogens (O, S, Se and Te) on the other hand crystallize in two structures: zinc blende (ZB) and wurtzite (WZ). These phases depend on the thermodynamic conditions. Under ambient conditions, the thermodynamically stable structure for ZnO is wurtzite. While the other three compound ZnS, ZnSe and ZnTe prefer the zinc blende structure, they can transform to wurtzite structure in higher temperatures degrees **[13]**.

The wurtzite (hexagonal) phase and the zinc blende (cubic) phase are very similar. They have the same number of first and second neighbors of an atom. Both structures consist of tetrahedral coordinated atoms. A hexagonal structure is transformed into a cubic structure by a rotation of the tetrahedron by 60° around the axis [0001] **[14]** (see **Figure I.1**). The primary difference between the two structures is the plane stacking order, which in the wurtzite structure is ABABAB… for (0001) planes, while in the zincblende structure it is ABCABC… for (111) planes. In this work, binary and ternary materials are studied in the wurtzite structure.

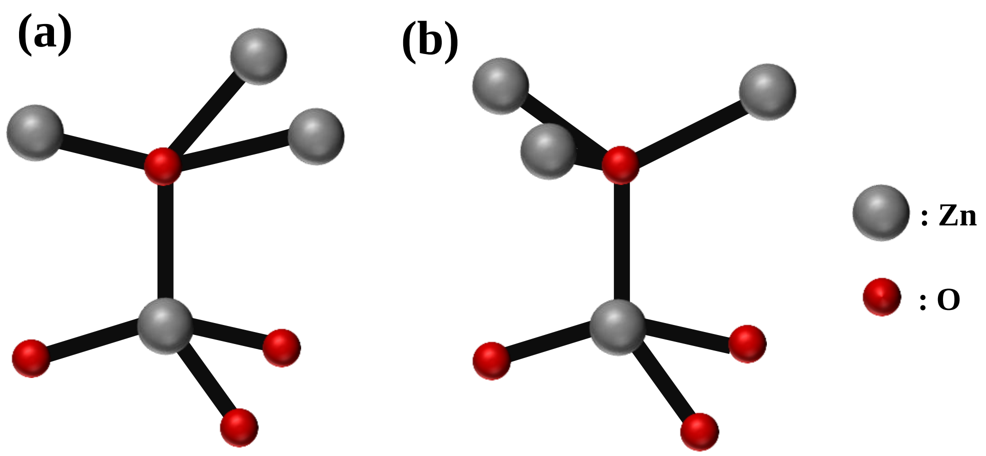

Figure I.1 Arrangement of atoms in: (a) the zinc blende phase and (b) the wurtzite phase.

a. Zinc blende structure

The zinc blende structure, also known as phase (B3), is characterized by its cubical lattice arrangement. In terms of symmetry, this structure belongs to the $\bar{F}43m$ space group in the Hermann-Mauguin notation and T_d^2 in the Schoenflies notation. To provide a visual representation, **Figure I.2** presents a schematic illustration showcasing the zinc blende structure.

The crystal lattice of zinc blende can be deconstructed into two interpenetrating face-centered cubic sublattices. One sublattice is composed of atoms from element II, while the other sublattice consists of atoms from element VI. These two sublattices are shifted relative to one another along the diagonal of the cube by a displacement of $(\frac{a}{4}, \frac{a}{4}, \frac{a}{4})$, where *a* represents the lattice parameter. Consequently, each atom resides at the center of a regular tetrahedron, with the vertices occupied by an atom of the opposite species **[15]**.

The unit cell serves as the fundamental building block from which the entire crystal can be reassembled through a series of translations. In the zinc blende structure, the unit cell contains one atom of each type. Specifically, the anions occupy the position (0, 0, 0), while the cations are located at (0.25, 0.25, 0.25).

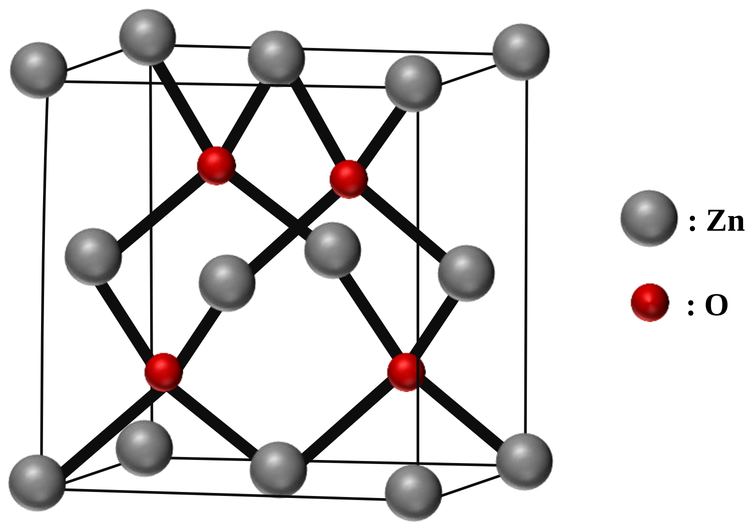

Figure I.2 Zinc blende crystal structure.

b. Wurtzite structure

The wurtzite structure or the phase (B4) is characterized by a hexagonal lattice. The space group of this structure is P6₃mc in the Hermann-Mauguin notation and C_{6v}^{4} in the Schoenflies notation. **Figure I.3** displays a schematic illustration of the wurtzite structure. The structure may be constructed using two overlapping sublattices organized in a hexagonal close-packed (hcp) arrangement. A single type of atom makes up each sublattice, and they are displaced from one another along the threefold *c*-axis by a distance denoted by the parameter *u*. this internal parameter is equal to 3/8 in an ideal wurtzite structure. The hexagonal lattice of the Wurtzite structure is characterized by three lattice constants *a*, *c*, and *u* where *a* represents the lattice parameter for the side length of the hexagon in the (0001) plane. It defines the length of one side of the hexagonal unit cell, and *c* corresponds to the lattice parameter for the height of the unit cell along the [0001] axis. The ratio of lattice parameters *c* and *a* in an ideal wurtzite structure is 8/3. The internal parameter *u* is the bond length parallel to the c-axis to the *c* lattice parameter ratio. Within the wurtzite unit cell, there are four atoms positioned as follows: (0,0,0) and (2/3,1/3,1/2) for the anions, and (0,0,5/8) and (2/3,1/3,1/8) for the cations. It is worth mentioning that the *c/a* ratio and the *u* parameter have a substantial connection. When the *c/a* ratio decreases, the *u* parameter tends to increase **[14]**. Even when the tetrahedral angles are distorted due to long-range polar interactions, this formula ensures that the four tetrahedral lengths remain essentially constant.

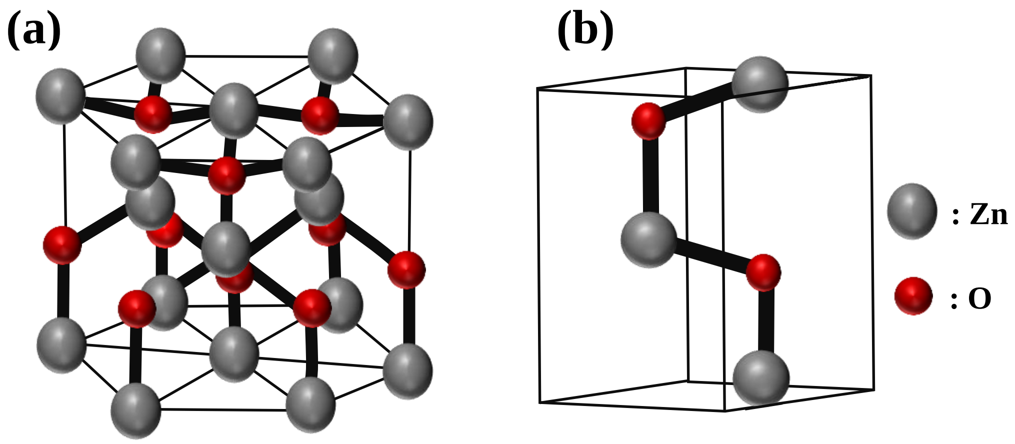

Figure I.3 Wurtzite crystal structure: (a) conventional cell. (b) unit cell.

I.2.2 Atomic bonding in II-VI semiconductors' alloys

The semiconductors investigated in this study belongs to the II-VI group, meaning they consists of an element from column II and an element from column VI of the periodic table, following Mendeleev's classification. Specifically, the II element is represented by the zinc atom, which possesses two valence electrons in an *s* orbital. Its electronic configuration is [Zn] = [Ar]3*d*10-4*s*2. On the other hand, the VI element represents the chalcogenide atoms, which have six valence electrons in a *p* orbital. The bonding between II and VI atoms in the II-VI semiconductor is covalent in nature, resulting from the sp^3 hybridization of atomic orbitals. Moreover, because chalcogenide atoms are very electronegative, an ionic bond is also present. The II-VI bond is therefore iono-covalent **[16]**. The iconicity will give II-VI materials their remarkable properties, the good ones (wide band gap, strong Coulomb interactions) as well as the less good ones (low rigidity). While the covalent bond will give them the structural properties since it requires each anion to be at the center of a tetrahedron formed by the cations and vice-versa **[17]**. The resulting maximum compactness crystalline structure (34%) is either cubic (zinc blende), or hexagonal (wurtzite).

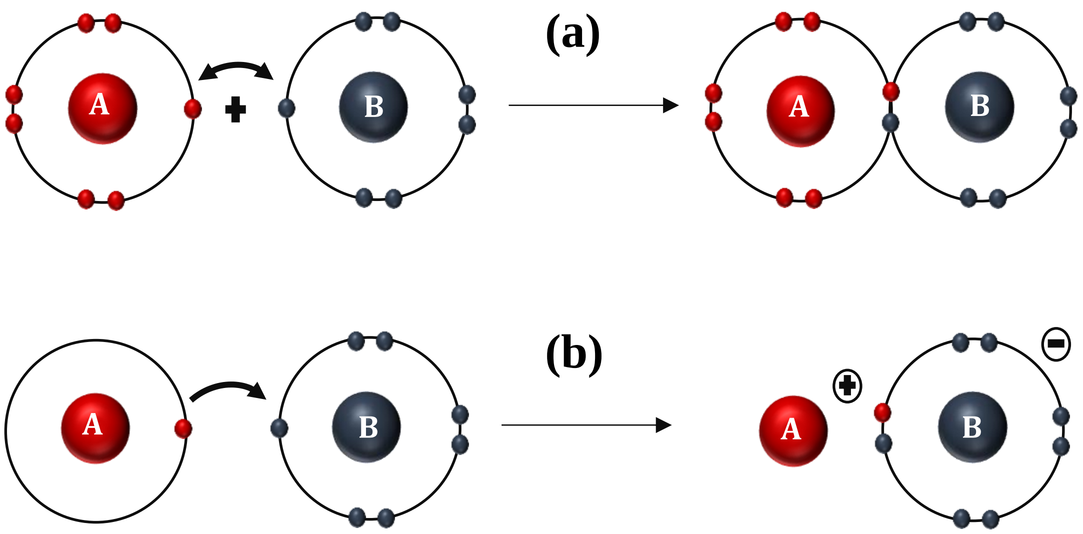

Figure I.4 Atomic bonding in II-VI semiconductors: (a) covalent bond. (b) ionic bond.

I.2.3 The first Brillouin zone

The Brillouin zone notion is crucial in solid-state physics because it helps us understand the basic concepts behind electronic energy bands. Brillouin zones are primitive Wigner-Seitz cells within the reciprocal lattice. In reciprocal space, the smallest enclosed volume surrounded by planes that act as perpendicular bisectors of the lattice vectors starting from the reference point is referred to as the first Brillouin zone **[18]**. When examining the electrical structure of solids, it is essential to comprehend the idea of Brillouin zones. The second and third Brillouin zones, for example, are different areas with the same volume that are gradually further away from the reference point. These are, however, less often used. The first Brillouin zone is hence frequently referred to as the Brillouin zone. In the case of the zinc-blende structure, the first Brillouin zone exhibits a truncated octahedral shape, with its six faces originating from the cube (refer to **Figure I.5**). On the other hand, the first Brillouin zone for the wurtzite structure takes on a hexagonal form. Both structures possess a center of symmetry denoted as Γ at the origin. These first Brillouin zones are characterized by symmetry points and symmetry lines, which can be determined using group theory, and they play a crucial role in the theory of band structures **[19]**. The symmetry lines represent axes extending from the origin to the boundaries of the Brillouin zone, and the points where these symmetry lines intersect the boundaries of the first Brillouin zone are known as high symmetry points.

I.2.4 Direct and indirect gap semiconductor

The energy bands give the possible energy states for electrons depending on their wave vector. Thus, the first Brillouin zone is represented in reciprocal space and, to simplify, in the directions of highest symmetry. They break down into valence bands and conduction bands. It is the lowest valence band, the highest conduction band, and the forbidden band or gap which separates them which mainly determine the transport properties of the semiconductor **[18]**. The band structures represented in the **Figure I.6** show two fundamental cases of semiconductor. When the valence band maximum and conduction band minimum are situated at a value near to the wave number k on the diagram E(k), we say that the semiconductor has a direct gap. On the opposite hand, when the valence band maximum and conduction band minimum are positioned at different values of the wave number k on the E(k) diagram, we speak of an indirect gap semiconductor. In direct gap

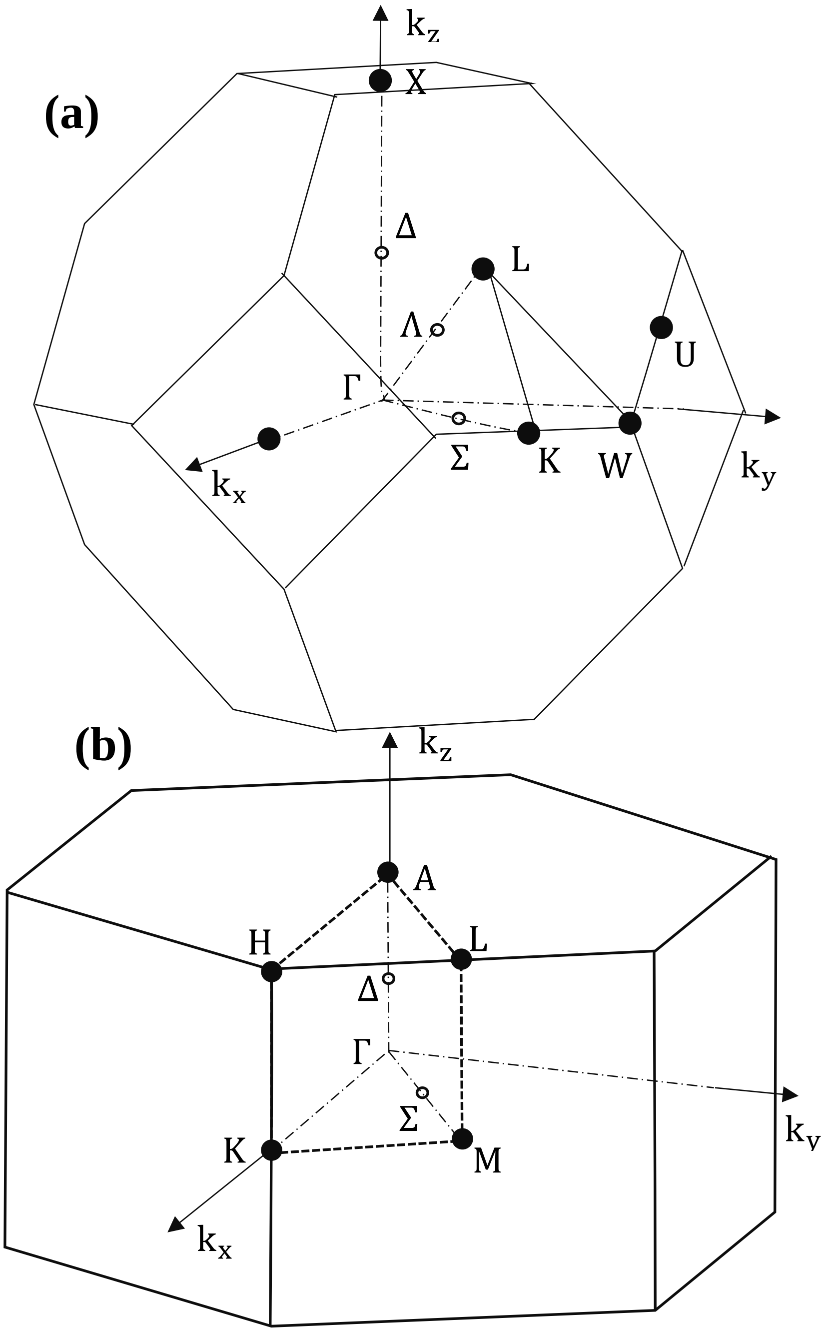

Figure I.5 First Brillouin zone for: (a) zinc blende. (b) wurtzite.

semiconductors, the central minimum of the conduction band corresponds to electrons of low effective mass, therefore very mobile. On the other hand, those which have an indirect gap, their conduction band corresponds to electrons of large effective mass, therefore having a low mobility. This distinction between direct and indirect gap semiconductor materials is important, particularly for optoelectronic applications which involve both electrons and photons. Indeed, during the transition of an electron from the BV to the BC or the electron-hole recombination, it is necessary to conserve the energy (scalar relation) and the momentum (vector relation). The minimum energy transition between these two bands can take place without a wave vector change in direct-gap semiconductors, which allows the absorption and emission of light much more efficiently than in materials with indirect gap. This difference guides the choice of materials for optoelectronic applications.

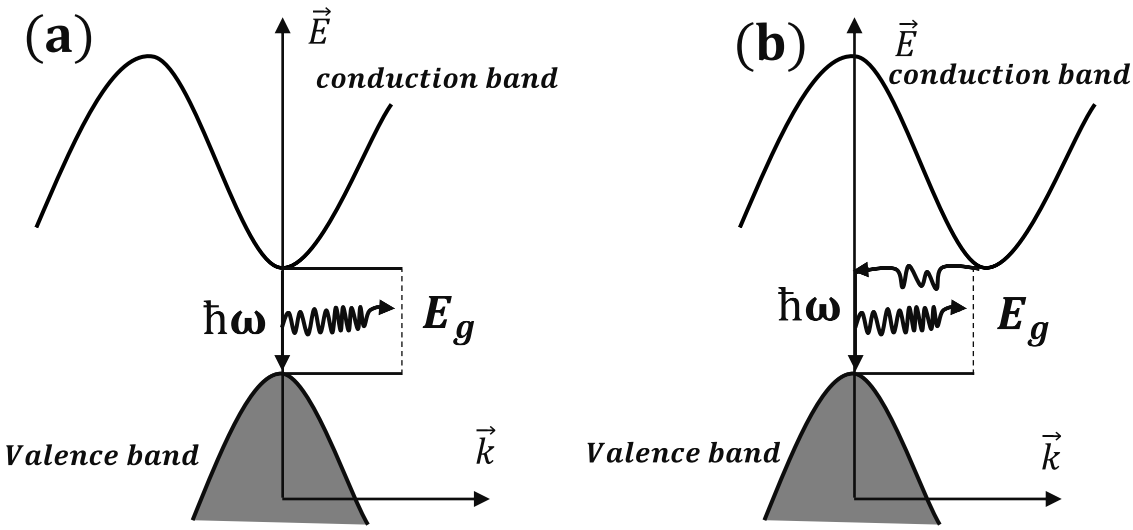

Figure I.6 band structure of semiconductors: (a) direct gap. (b) indirect gap.

I.3 Generalities on Semiconductors alloys

The technological need for new materials with special characteristics and properties led to the idea of mixing materials to have what is called "alloys". Materials made of two or more different elements are called alloys. A binary alloy has two components, a ternary alloy has three, and a quaternary alloy has four. In general, the characteristics of the alloying material are quite different from those of its components. There was a time when the word alloy was only reserved for metals, yet this definition very quickly became associated with other materials, in particular ceramics and polymers. Soon after the development of modern techniques of crystal growth and purification of semiconductors, several binary, ternary and quaternary alloys were produced. The use of these in the fields of microelectronics and optoelectronics has encouraged researchers to develop the theoretical as well as the experimental side. Indeed, the progress made by chemists, materials physicists and technologists has effectively contributed to the study and manufacture of new materials, among them III-V and II-VI semiconductor alloys **[20]**.

I.3.1 Classification of semiconductors alloys

Semiconductor alloys are categorized into many types based on the number of components [21]:

- Binary alloys of the form $\mathbf{A^{N}B^{8-N}}$:

$\mathbf{A^{I}B^{VII}}$: KBr, AgCl, CuBr, LiF, …

$\mathbf{A^{II}B^{VI}}$: ZnS, ZnO, ZnSe, CdS, CdSe, CdTe, HgTe, HgSe, ..

$\mathbf{A^{III}B^{V}}$**:** antimoniides, arsenides, phosphides, and nutrides of the elements: Aluminum, Gallium, Indium and Boron (AlAs, GaAs, InSb, BN, InP,……).

$\mathbf{A^{IV}B^{IV}}$: SiGe, SiC, …..

- Binary alloys of the form $\mathbf{A^{N}B^{10-N}}$:

$\mathbf{A^{IV}B^{VI}}$: PbO, PbS, PbTe, ……..

- Alliage binaire de la forme $\mathbf{A^{N}B^{7-N}}$:

$\mathbf{A^{I}B^{VI}}$: CuO, CuS, Cu_2O, ……

When the binary elements $\mathbf{A^{N}B^{8-N}}$ and $\mathbf{A^{N}C^{8-N}}$ are associated, two types of alloys can be formed:

- Anionic ternary alloy: $\mathbf{A^{N}B_{x}^{8-N}C_{1-x}^{8-N}}$.

- Cationic ternary alloy: $\mathbf{A_{x}^{N}B_{1-x}^{N}C^{8-N}}$.

These alloys are defined by the stoichiometric coefficient *x*. However, there is also another type of semiconductor alloy, which called quaternary materials. This particular form of semiconductor alloy can be identified by the existence of two stoichiometric coefficients, *x* and *y*, and is composed of four binary compounds. A particular interest has recently been brought to quaternary alloys mainly because of the advantage they offer to design devices with the desired physical properties. These alloys can be divided into two classes [22-23]:

- Quadratic solutions: these alloys have the form $\mathbf{A_{1-x}^{N}B_{x}^{N}C_{y}^{8-N}D_{1-y}^{8-N}}$.

- The triangular solutions in this class, two cases arise, the purely anionic solutions $\mathbf{A^{N}B_{x}^{8-N}C_{y}^{8-N}D_{1-x-y}^{8-N}}$ and the purely cationic solutions $\mathbf{A_{x}^{N}B_{y}^{N}C_{1-x-y}^{8-N}D^{8-N}}$.

Quadratic quaternary alloys were the first and most researched and studied, particularly $Ga_xIn_{1-x}As_yP_{1-y}$, $Ga_{1-x}In_xAs_ySb_{1-y}$. Nevertheless, triangular alloys seem to become just as important. The criteria concerning the agreement of the lattice parameters as well as the identity of the crystalline structures of the parent binary elements always remain valid in the case of quaternary alloys.

I.4 Basic properties of binary alloys (ZnX, X = O, S, Se, Te)

I.4.1 Structural properties

II-VI semiconductor alloys display greater structural variability than III-V compounds. Zinc blende properties are prevalent in most compounds, but wurtzite hexagonal structures are more common. Zinc blende may be observed under ambient conditions, but heating can convert it to wurtzite. The predominance of the wurtzite form is often associated with smaller anions, such as oxides, whereas larger anions, like tellurides, tend to stabilize the zinc blende phase. However, it is worth noting that there are exceptions to this trend, as seen in mercury sulphide (HgS), which exhibits the trigonal cinnabar phase as a representative example.

Unit cells have a lattice parameter, which is defined as the distance between two spots located at the corners of the cell. The lattice parameter is denoted by different letters, namely a, b, and c. In the case of a hexagonal lattice where two sides are equal, the lengths of the two lattice parameters are represented by a and c instead of b. The Greek letters α, β, and γ are employed to represent the angles associated with these lattice parameters.

When a foreign atom is introduced into a crystal lattice, it generally causes a variation in the crystal parameter which results in expansion or contraction of the lattice, depending on the size of the atoms. One of the major challenges in the choice of materials for the fabrication of heterostructures was always the illumination of dislocations due to the stresses formed by the lattice mismatch between the epitaxial layers. The lattice parameter for a number of the most easily epitaxial binary semiconductor compounds and they provided a basis for building more complex ternary and quaternary alloys, formed by the groups; IV, III-V and II-VI, are grouped together in **Table I.1** below **[24]**.

Table I.1 Crystal structure and lattice parameter for IV, III-V and II-V semiconductor groups at 300 K. Diamond d, zinc-blende zb, hexagonal h, wurtzite w, (rocksalt, NaCl) rs, orthorhombic or, and rhombohedral rh **[24]**.

System	**Material**	**Crystal structure**	**a (Å)**	**c (Å)**
IV	Diamond	d	3.5670	
	Si	d	5.4310	
	Ge	d	5.6579	
	Sn	d	6.4892	
	3C SiC	zb	4.3596	
	6H SiC	h	3.0806	15.1173
III-V	BN	zb	3.6155	
	BN	h	2.5040	6.6612
	BP	zb	4.5383	
	BAs	zb	4.7770	
	AlN	h (w)	3.1120	4.9820
	AlP	zb	5.4635	
	AlAs	zb	5.6614	
	AlSb	zb	6.1355	
	GaN	h (w)	3.1896	5.1855
	GaP	zb	5.4508	
	GaAs	zb	5.6533	
	GaSb	zb	6.0959	
	InN	h (w)	3.5480	5.7600
	InP	zb	5.8690	
	InAs	zb	6.0583	
	InSb	zb	6.4794	
II-VI	BeO	h (w)	2.6979	4.3800
	BeS	zb	4.8650	

BeSe	zb	5.1370	
BeTe	zb	5.6170	
MgO	rs	4.2030	
MgS	rs	5.2030	
MgSe	zb	5.9100	
MgTe	h (w)	4.5480	7.3900
ZnO	h (w)	3.2495	5.2069
ZnS	h (w)	3.8226	6.2605
ZnS	zb	5.4102	
ZnSe	zb	5.6692	
ZnTe	zb	6.1037	
CdO	rs	4.6860	
CdS	h (w)	4.1367	6.7161
CdSe	h (w)	4.2999	7.0109
CdTe	zb	6.4810	
HgO	or	3.5770 (a)	
		8.6810 (b)	
		2.4270 (c)	
		0.7450 (u)	
HgS	rh	4.1400 (a)	
		9.4900 (b)	
		2.2920 (c)	
		0.7200 (u)	
		0.4800 (v)	
HgSe	zb	6.0840	
HgTe	zb	6.4603	

I.4.2 Band structure

The nature of the gap in semiconductors is important in determining their interaction with electromagnetic radiation, thus influencing the functionality of optoelectronic components. The size of the band gap increases noticeably as we move from group IV elements to III-V and II-VI elements along the periodic table, whereas moving down the table causes the band gap to shrink **[25]**. **Figure I.7** displays pertinent information regarding the electronic band structure of ZnO in the wurtzite structure **[26]**. Furthermore, **Figure I.7(a)** demonstrates that at the center of the Brillouin zone, the maximum valence band coincides with its minimum conduction band, indicating a direct band gap. In addition, **Figure 1.7(b)** demonstrates that the valence band is characterized by *p*-like states, while the conduction band primarily consists of s-like symmetric states. The valence band can be broken up into three distinct bands as a result of the interplay between the crystal field and the spin orbit interactions **[27]**. These bands have a significant impact on the intrinsic absorption and emission spectra that are found close to the bandgap. These bands exhibit specific symmetries, with the upper valence sub-band referred to as the A-band ($\Gamma7$), corresponding to the heavy hole, the middle sub-band as the B-band ($\Gamma9$), corresponding to the light hole, and the lowermost sub-band as the $\Gamma7$ (C-band), originating from the crystal field effects. Notably, the spin-orbit splitting is approximately -8 meV, while the crystal-field splitting is around 42 meV **[28-29]**.

Table I.2 presents the bandgap energies of various II-VI materials at the Γ points of the Brillouin zone **[24]**. It is noteworthy that all the binary materials considered in this study exhibit direct bandgap characteristics, further highlighting their significance as semiconductors.

Table I.2 The bandgap energies of various II-VI materials **[24]**.

Material	Crystal structure	E_g(eV)
ZnO	zb	3.17
	h(w)	3.45
ZnS	zb	3.72
	h(w)	3.75
ZnSe	zb	2.721
ZnTe	zb	2.27

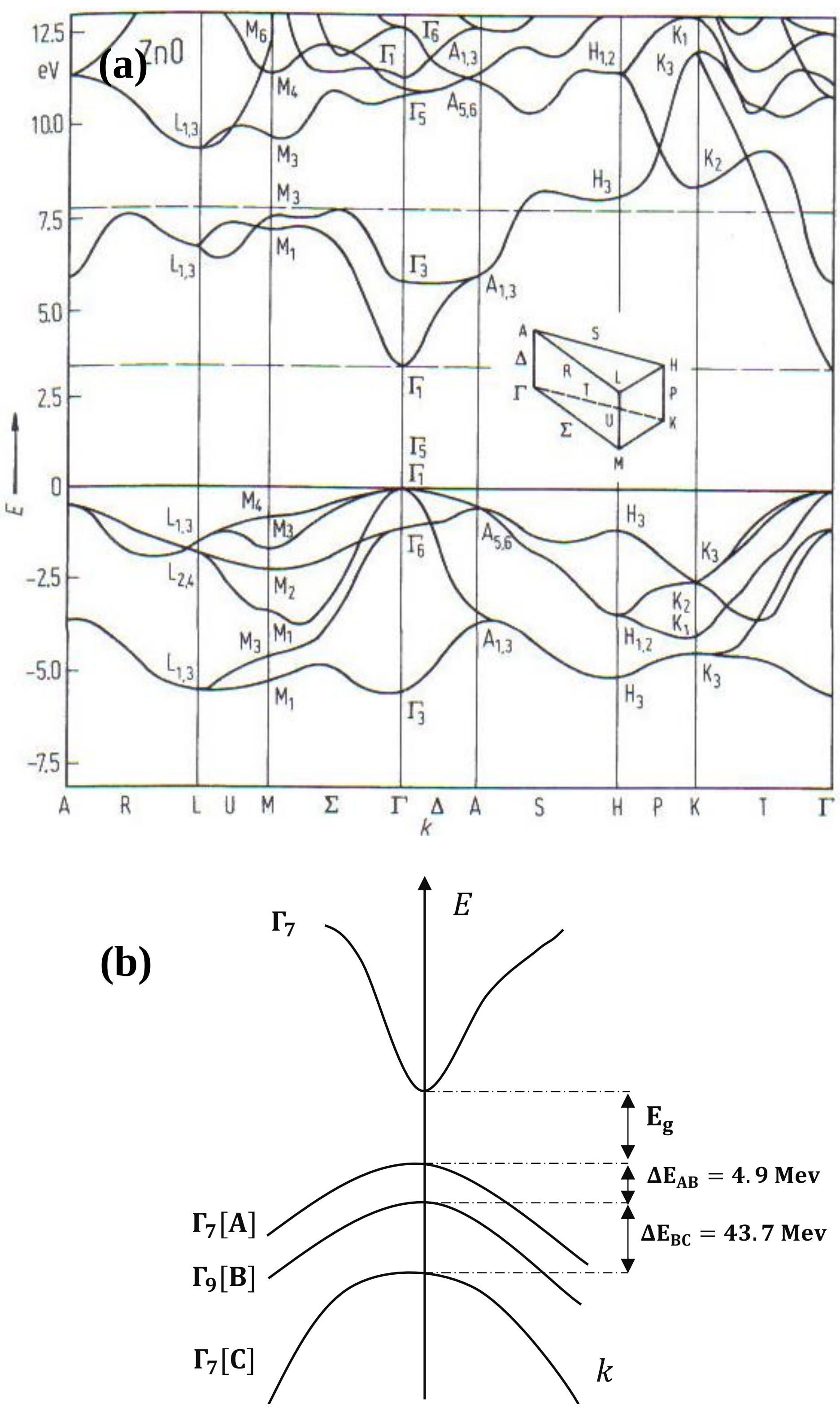

Figure I.7 Energy band structure of wurtzite ZnO: (a) using pseudo potential method [26]. (b) parabolic approximation.

I.5 Fundamental properties of ZnO-based ternary alloys

The ternary crystal $A_xB_{1-x}C$ is composed of the AC molecules with a molar fraction x and the BC molecules with a fraction (1-x). Thus, the physical property T(x) can be represented as a simple analytical interpolation of the properties of its binary compounds AC and BC **[30]**.

$$T(x) = xB_{AC} + (1-x)B_{BC} \equiv a + bx \qquad (I.1)$$

Where $a \equiv B_{BC}$ and $b \equiv B_{AC} - B_{BC}$. For the lattice parameter, the **Equation I.1** became:

$$a(x) = xa_{AC} + (1-x)a_{BC} \qquad (I.2)$$

This formula is called Vegard's law **[31]**. Nevertheless, certain material parameters deviate substantially from the linear relationship depicted in **Equation I.1** and exhibit an approximately quadratic dependence on x. In such a case, the ternary material parameter can be approximated very efficiently by the following formula:

$$T(x) = xB_{AC} + (1-x)B_{BC} + x(1-x)C_{AB} \equiv a + bx + cx^2 \qquad (I.3)$$

Where $a \equiv B_{BC}$, $b \equiv B_{AC} - B_{BC} + C_{AB}$ and $c \equiv -C_{AB}$. The parameter c is called bowing parameter. For example, we can write the gap energy of ternary alloy as follow **[32]**:

$$E_g(x) = xE_{AC} + (1-x)E_{BC} + x(1-x)C_{AB} \qquad (I.4)$$

I.5.1 $ZnO_{1-x}S_x$ alloy

In recent years, researchers have been exploring $ZnO_{1-x}S_x$ as a potential alternative to the toxic CdS compound commonly used as an n-type window/buffer material in solar cells. $ZnO_{1-x}S_x$ has been employed as a window/buffer layer in various solar cell types, including CIGS-based **[33-34]**, CZTS-based and SnS-based solar cells **[35-38]**, resulting in enhanced solar cell performance. ZnOS offers the flexibility to create graded band gap solar cells based on CdTe, either in combination with or without CdS, similar to the ones recently achieved using ZnS or incorporating CdZnS. This is achievable due to ZnOS's adjustable band gap properties **[39-42]**.

In their preliminary research, Yoo et al. **[43]** used the pulsed laser deposition (PLD) method to incorporate sulphur (S) to zinc oxide (ZnO). This was accomplished by alternately ablating ZnO and ZnS targets. The maximal solid solubility of 'S' was found to be restricted to 0.13 when single-phase wurtzite ZnOS alloy films were grown at 700 °C on c-sapphire substrates. Additionally, a nonlinear link between the ‘S’ content and the *c*-axis lattice constant and bandgap was seen. Zhang et al. **[44]** utilized a similar approach by employing a ZnS ceramic as the ablation target and introducing O_2 as the reactive gas. Their study showed that wurtzite ZnOS films produced on c-sapphire substrates have an extended sulphur (S) solubility. Interestingly, at 300 °C, the ‘S’ solubility surged to a high of 55.6 %. They successfully produced single-phase ZnOS alloy films with a wurtzite structure across the whole composition range by switching the substrate to glass and modifying the oxygen pressure. The band gap energy was also shown to have a linear connection with the ‘S’ composition, which allowed them to reduce it to a value of 2.63 eV. Similarly, He et al. **[45]** conducted a study where they achieved significantly enhanced sulfur (S) solubility by growing ZnOS films at a temperature of 750 °C on *c*-sapphire substrates. According to the study's conclusions, the sulfur solubility in wurtzite ZnOS with a high oxygen content reached 0.23, while the ‘O’ solubility in zinc-blend sulfur rich ZnOS was 0.06. These films showed an in-plane orientation relation, with hexagonal grains evenly dispersed across the whole surface and ZnOS [100] aligning parallel to sapphire [$1\bar{1}0$]. Whereas the bandgap of $ZnO_{1-x}S_x$ showed a nonlinear variation, with a bowing parameter of 2.91 eV, and a gap value reduced from 3.27 eV to a low of 2.92 eV at 0.18 x composition. Also, it was noted that the lattice constants a and c steadily expanded with increasing ‘S’ content.

The significant electronegativity of oxygen in wurtzite ZnO along the *c*-orientation causes the well-known phenomena of spontaneous electrostatic field to appear. This electrostatic field has the effect of spatially separating electrons and holes. As a result, it reduces recombination, which limits efficiency **[5]**. Different strategies have been used to eliminate spontaneous electrostatic fields in order to get around this constraint. Examples include cation-substituted MgZnO **[46-47]**, nonpolar pure ZnO **[48-49]**, and CdZnO **[50-51]**. In contrast, pulsed laser deposition (PLD) has just recently been investigated as a method for growing nonpolar $ZnO_{1-x}S_x$ films. Li et al. **[52]** grow *a*-plane $ZnO_{1-x}S_x$ films using pulsed laser deposition (PLD) technique to epitaxially on r-plane sapphire substrates at a temperature of 600 °C. They discovered that the addition of sulfur (S) to $ZnO_{1-x}S_x$ caused the crystal structure to expand, with the lattice constants rising as the sulfur composition did. They also discovered that the relationship between the *a*-plane $ZnO_{1-x}S_x$ films and the *r*-plane sapphire substrate was $ZnO_{1-x}S_x$ [0001] ‖ sapphire [1101] and $ZnO_{1-x}S_x$ [1100] ‖ sapphire [1120]. Additionally, they notice that the bandgap reduced from 3.22 eV to 2.66 eV going from sulfur composition of $x = 0$ to $x = 0.43$.

In the composition range from x = 0.12 to x = 0.28, Chen et al. **[53-54]** effectively produced single-phase wurtzite $ZnO_{1-x}S_x$ films with a non-polar *m*-plane orientation. The only temperatures at which this phase development was possible were those over 400 °C. They also determined the in-plane orientation relationship, which was ZnOS [0001] aligned with sapphire [1021] and ZnOS [1021] aligned with sapphire [1000]. The linear expansion of the lattice constants was as follows: $a=1.67x-0.25$ and $c=1.15x+0.17$. A polynomial fit equation, $E_g=3.22-0.0197x+0.0004x^2$, over the range of 0.12<x<0.28, where the bowing parameter equal to 0.0004 eV, might explain the observed rise in bandgap energy from 2.95 eV to 3.05 eV.

Meyer et al. **[55]** employed radio-frequency (RF) sputtering to deposit a series of samples using a ceramic ZnS target on glass and sapphire substrates, while varying the Ar/O_2 pressure ratio. Their research revealed wurtzite symmetry in the films and a linear change of the lattice constant with composition between 0 and 0.4. This implies that Vegard's law holds true for this composition range. Also, the composition-dependent band gap was evaluated. For x = 0.5, the gap energy was lowered down to around 2.7-2.8 eV, corresponding to a bowing parameter of 2.5 eV.

In a related experiment, Pan et al. **[56]** carried out the same investigation using glass and quartz as the substrate instead of sapphire. According to their findings, the zinc oxide films had a zinc blende structure with a preferred orientation along (111) within the sulfur-rich side (0.77<x<1) and a wurtzite structure with a preferred orientation along (002) in the oxygen-rich side (0<x<0.23). However, within the range of 0.23<x<0.77, the films were made of an amorphous $ZnO_{1-x}S_x$. The optical bowing parameter of the films, which is about 2.9 eV, showed a nonlinear dependency on the sulfur composition. Xu et al. **[57]** have also obtained similar results.

Baldissera et al. **[58]** conducted theoretical research on the bandgaps and lattice constants of $ZnO_{1-x}S_x$ alloys in the wurtzite and zinc-blende phases using Density Functional Theory (DFT) simulations. According to their observations, there was only a 0.3% deviation from linear behavior in the lattice constants' expansion in proportion to sulfur (S) content. In addition, comparable bowing behavior was seen in the computed bandgaps of ZB-$ZnO_{1-x}S_x$ and WZ-$ZnO_{1-x}S_x$. The bandgap of WZ-$ZnO_{1-x}S_x$ approached 2.5 eV at x = 0.5. Notably, predicted results are reasonably consistent with the experimental data that were previously provided.

When comparing formation energies at 0 K to identify the phase structure of WZ-ZnOS and ZB-ZnOS alloys, Zhu et al. [59] discovered that the wurtzite structure is more thermodynamically stable for sulfur (S)-rich alloys and the zinc-blende structure is more stable for oxygen (O)-rich alloys. The $ZnO_{1-x}S_x$ phase transition appears to take place between 0.2 and 0.25. The bandgap, valence band maximum (VBM) offset, and conduction band minimum (CBM) offset in ZnOS alloys were also calculated by Persson et al [60]. It has been found that the significant bandgap bowing in ZnOS alloys is due to a non-linear variation in both VBM and CBM with the ‘S’ content. Additionally, they suggested that *p*-type doping in ZnO-like alloys would be made possible by the upward shift of the valence band (VB) caused by the development of local ZnS-like states in the ZnO host. These alloys have lower formation energies and shallower acceptor states. **Figure I.8** shows several experimental findings of lattice constants and bandgap for the $ZnO_{1-x}S_x$ ternary alloy.

I.5.2 $ZnO_{1-x}Se_x$ alloy

The $ZnO_{1-x}Se_x$ alloy, belonging to the category of highly mismatched alloys (HMAs), exhibits unique semiconducting properties. This alloy undergoes a significant disruption in its band structure when larger and less electronegative selenium (Se) atoms replace oxygen (O) atoms. However, the synthesis of such highly mismatched alloys poses challenges due to the disparities in atom size and electronegativity. The energy band structure of these alloys is primarily governed by the interaction between the localized states of the minority component and the extended band states of the majority component [61]. In their experimental study, Iwata et al. [62] used molecular beam epitaxy (MBE) with a ZnO buffer layer at temperatures between 250 °C and 350 °C to conduct epitaxial growth studies on a-plane sapphire substrates for wurtzite ZnOSe alloy films. Within the limited range of Se content from 0 % to 1 %, they observed a little reduction in the alloy's bandgap. Using the same approach and RF-plasma excited oxygen, a deposition process obtained $ZnO_{1-x}Se_x$ films with a zinc-blende structure in the Se-riche compositions ($0.987 \le x \le 1$) on (001)-oriented GaAs substrates. The bandgap of the $ZnO_{1-x}Se_x$ film grown by molecular beam epitaxy (MBE) increased as the Se content increased from 2.52 eV to 2.68 eV [63-64]. During their examination, significant findings emerged as very localized oxygen states resulting from band anticrossing were discovered, positioned approximately at 220 meV above the conduction-band boundary of ZnSe. In a study conducted by Chen et al. [65], Se-rich $ZnO_{1-x}Se_x$ films were successfully synthesized on *c*-sapphire substrates using molecular beam epitaxy (MBE) along with a ZnSe buffer layer. This synthesis technique led to the

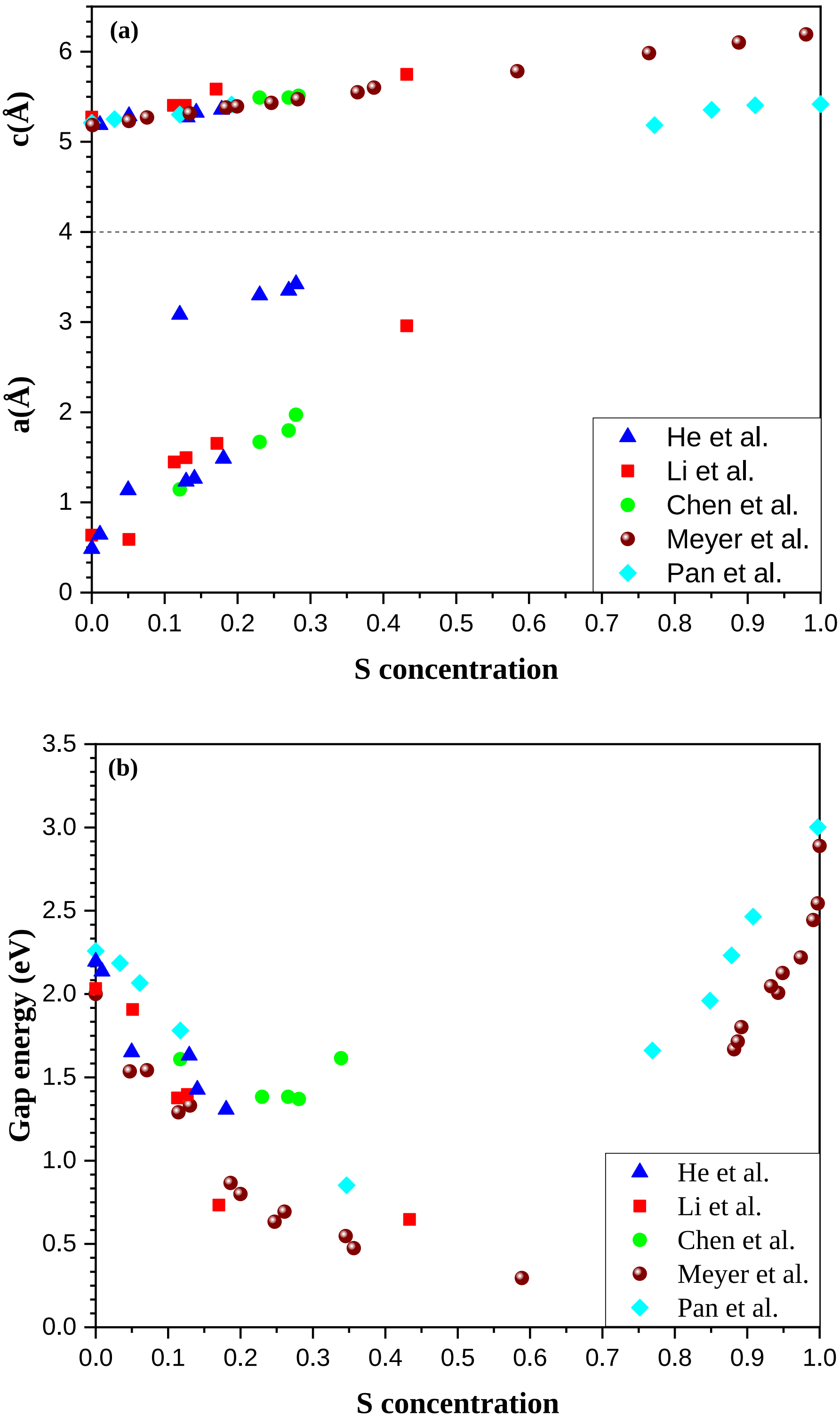

Figure I.8 Changes in: (a) lattice constants a and c. (b) bandgap energy as a function of 'S' content in the $ZnO_{1-x}S_x$ ternary alloys **[45, 52, 54-56]**.

achievement of an expanded bandgap reaching 2.05 eV, with an optimal Se content of x = 0.885. Furthermore, Mayer et al. **[66-67]** employed pulsed laser deposition (PLD) with separate ZnO and ZnSe targets to create O-rich ZnO1-xSex alloy films on c-sapphire substrates. By varying the 'Se' compositions from 0 % to 0.12 %, they were able to explore a wide range of compositions and their corresponding bandgap properties. Up to 2.05 eV (x = 0.12) of enlarged bandgap was successfully attained by them. According to a recent study by Lee et al. **[68]**, single-phase wurtzite $ZnO_{1-x}Se_x$ films were grown via PLD on *c*-sapphire substrates utilizing a Se-alloyed ZnO target. With rising Se content, they saw a narrowing of the bandgap and an expansion of the lattice. Additionally, Polity et al. **[69]** deposited O-rich $ZnO_{1-x}Se_x$ ($0<x<5\%$) and Se-rich $ZnO_{1-x}Se_x$ ($91.5\%<x<1$) films on c-sapphire substrates using the molecular seeding approach, exhibiting a strong bandgap bowing effect of 7 eV.

Experimentally determined bandgaps of $ZnO_{1-x}Se_x$ alloy films prepared by various procedures are presented in **Figure I.9**. As shown in the diagram, both O-rich and Se-rich sides have a limited compositional frame. Changing the quantity of oxygen in an alloy can cause the bandgap to shift from approximately 3,3 eV to 2,05 eV ($0<x<0.12$). Additionally, the bandgap of Se-rich alloys ($0.885<x<1.0$) can be altered between 2.05 and 2.82 eV. The close proximity of these experimental results to the BAC fitting curve indicates that theory and data are in good agreement. Theoretical projections indicate that $ZnO_{1-x}Se_x$ with a Se composition of x = 0.52 may obtain a smaller bandgap of approximately 1.63 eV; this opens up intriguing possibilities for tuning energy band structures.

Using the band-anticrossing (BAC) model, the bandgap energy of Se-rich ZnO_xSe_{1-x} alloys has been thoroughly characterized. Welna et al. **[70]** discovered the presence of a distinct band E_+ in ZnO_xSe_{1-x} alloys, lending credence to the conclusion that the BAC model effectively predicts the bandgap energy of ZnO_xSe_{1-x} alloys containing reduced oxygen. Zhao et al. **[71]** investigated the bandgap energy in Se-rich ZnO_xSe_{1-x} alloys and found that the contribution of the valence band maximum (VBM) to the bandgap reduction could be neglected in approximate calculations when the oxygen content was less than 0.12. Baldissera et al. **[58]** utilized density functional theory (DFT) and partially self-consistent $scGW_0$ approaches to investigate the structural and optical properties of $ZnO_{1-x}Se_x$ alloys. Their exhaustive investigation revealed that the lattice constants fluctuate with the composition of selenide atoms by as much as 0.5%. At low energies, a significant absorption coefficient was also detected. They made the astonishing prediction that the bandgap of the ternary $ZnO_{1-x}Se_x$ alloy could be reduced to levels suitable for solar energy utilization.

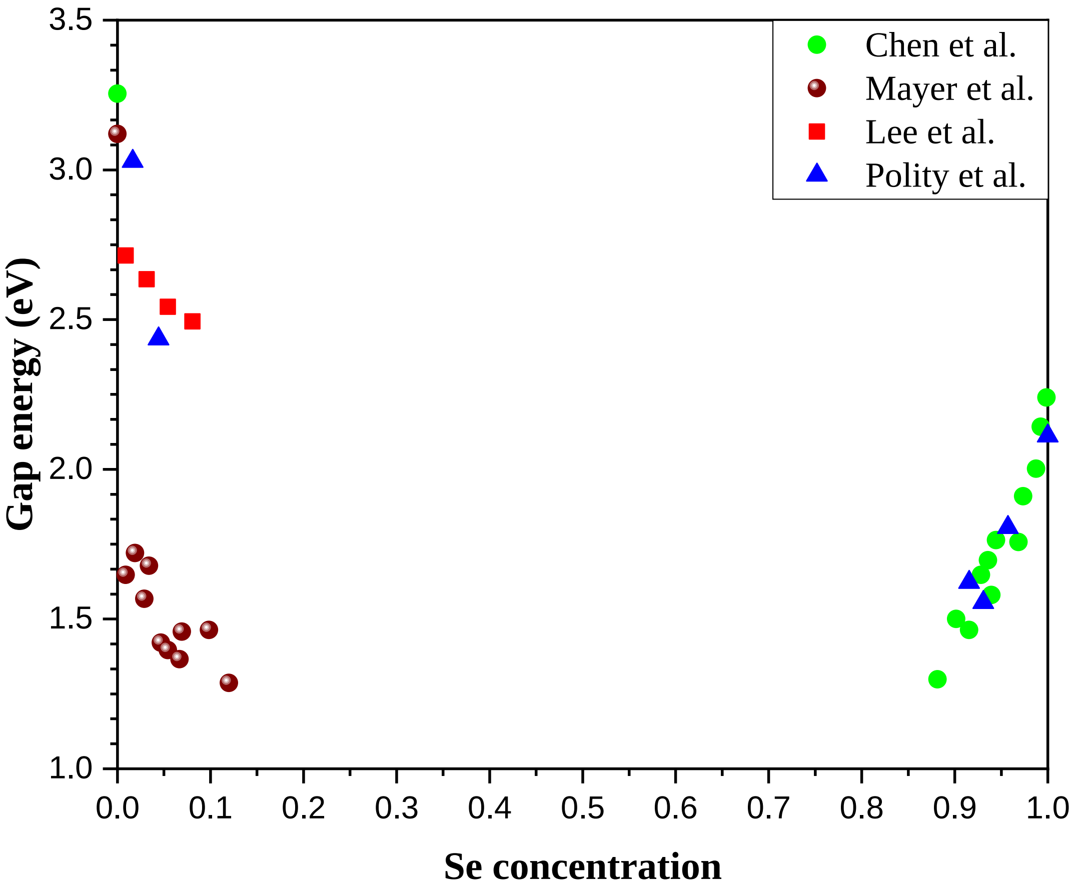

Figure I.9 Changes in bandgap energy as a function of 'Se' content in the $ZnO_{1-x}Se_x$ ternary alloys **[65-69]**.

I.5.3 $ZnO_{1-x}Te_x$ alloy

The flexibility of modifying the electronic band structure in $ZnO_{1-x}Te_x$ alloy was expected **[72]**, similar to the HMA material $ZnO_{1-x}Te_x$. The utilization of the band anticrossing (BAC) model proves to be a valuable approach in elucidating the relationship between alterations in band structure and variations in alloy composition **[73]**. The substitution of 'Te' in the ZnO lattice, characterized by a significantly higher electronegativity difference compared to 'Se' and 'O', was expected to exert a more pronounced influence on the electronic band structure. Consequently, this substitution was hypothesized to lead to a lesser decline in the bandgap. The synthesis of ZnOTe alloys was hindered by the significant challenge posed by the substantial disparity in atomic radii between tellerium (2.21 Å) and oxygen (1.4 Å) **[74]**. Consequently, the investigation of epitaxial growth of ZnOTe films has been limited to a small number of studies documented in the existing literature.

In their study, Nabetani et al. [75] effectively employed molecular beam epitaxy (MBE) to grow ZnTeO alloys on GaAs substrates oriented along the (001) crystal plane. The provision of oxygen was facilitated through an RF-plasma cell. A growth temperature of 300 °C was employed. An increase in the flow rate of O_2 resulted in the observation of a blue shift in the bandgap energy. The observed blue shift can be attributed to the repulsive interaction between the oxygen-induced energy states and the conduction-band edge of the ZnTe host material. In their study, Tanaka et al. [73] employed a molecular beam epitaxy (MBE) configuration to grow ZnTeO layers on ZnTe (001) substrates. The MBE setup incorporated a conventional radio frequency (RF) radical cell designed for oxygen. In the 'Te' sublattice, the researchers successfully synthesized alloys exhibiting significant substitutional oxygen compositions, reaching a maximum of 1.34 %. The optical transitions from the valence band to the conduction sub-bands were used to demonstrate the existing of anticrossing interaction between localized 'O' states and the extended conduction states of ZnTe. The observed energy position fluctuations of the sub-bands containing oxygen content were determined to be consistent with the calculations based on the Band Anticrossing (BAC) model. The characteristic feature of interacting two-level systems is the symmetrical shift observed in both E_- and E_+ states. Lee et al. [76] employed an RF magnetron sputtering technique to fabricate $ZnO_{1-x}Te_x$ films on *c*-plane sapphire substrates. The films were created using reactive gas mixtures consisting of argon and varying compositions of oxygen (0 %, 2 %, 4 %, 6 %, and 8 %). The experimental results indicate that as the oxygen composition increases, a transition in the phase of the $ZnO_{1-x}Te_x$ films is observed, shifting from a cubic structure to an amorphous structure. This transition is accompanied by an increase in the energy bandgap of the films, from 2.2 to 3.4 eV.

The study conducted by Ting et al. [77] extensively investigated $ZnO_{1-x}Te_x$ alloys, which exhibit a significant mismatch in composition, with a ZnTe mole fraction reaching up to 34 %. The researchers examined the synthesis, structural characteristics, electrical properties, and electronic band structure of the alloys utilizing the pulsed laser deposition (PLD) technique and the band anticrossing model. A direct energy gap was observed in $ZnO_{1-x}Te_x$ alloys with $x = 0.2$, with the minimum value being approximately 1.8 eV. According to calculations conducted using a modified BAC model that incorporated compositionally dependent coupling parameters, it was determined that the notable decrease in bandgap observed in $ZnO_{1-x}Te_x$ HMAs on the ZnO-rich side can be primarily attributed to the upward displacement of the valence band. This displacement is a result of the interaction between the valence band of ZnO and 'Te' states situated approximately 0.9 eV above it. The aforementioned conclusion was supported by empirical evidence demonstrating the upward displacement of the valence band. The initial investigations conducted by Sanchez et al. **[78]** examined the potential for doping ZnO in the wurtzite structure with a small fraction of Te (x = 0.04). These studies also proposed the presence of additional solid phases of 'Te' as the 'Te' content increased. Consequently, the incorporation of 'Te' atoms into the ZnO crystalline structure resulted in a decrease in the bandgap. Liu et al. **[79]** reported comparable results utilizing RF magnetron co-sputtering technique for the fabrication of thin films comprising the $ZnO_{1-x}Te_x$ alloy, encompassing a comprehensive range of compositions. The researchers made the observation that thin films composed of $ZnO_{1-x}Te_x$ HMAs exhibited distinct structural characteristics depending on their composition. Specifically, films with ZnO-rich compositions ($0<x<0.15$) displayed a wurtzite structure, while films with ZnTe-rich compositions ($x>0.9$) exhibited a zinc-blende structure. On the other hand, films with compositions falling within the range of $0.15<x<0.9$ were found to be amorphous.

The structural, electrical, and optical properties of ZnOTe alloys using special quasi-random structures (SQS) were theoretically examined by Noor et al. **[80]** in their paper. They found that the zinc blende phase of ZnOTe displayed a direct bandgap while the rock-salt phase displayed an indirect bandgap. Additionally, it was noted that the bulk modulus showed a linear decline with rising 'Te' content. However, the lattice parameters showed a linear rise in both phases. The thermodynamic characteristics of $ZnO_{1-x}Te_x$ alloys with compositions ranging from 0 to 1 were investigated by Long et al. **[81].** The cluster expansion method and a first-principles methodology were both used in this inquiry. Based on their investigation, it was shown that the formation energies of the wurtzite and zinc-blende phases were unusually high, preventing the formation of a stable phase in the ZnOTe alloys with large mismatches. They were only present during metastable stages, though. A different experimental bandgap values for $ZnO_{1-x}Te_x$ ternary alloys is depicted in **Figure I.10**

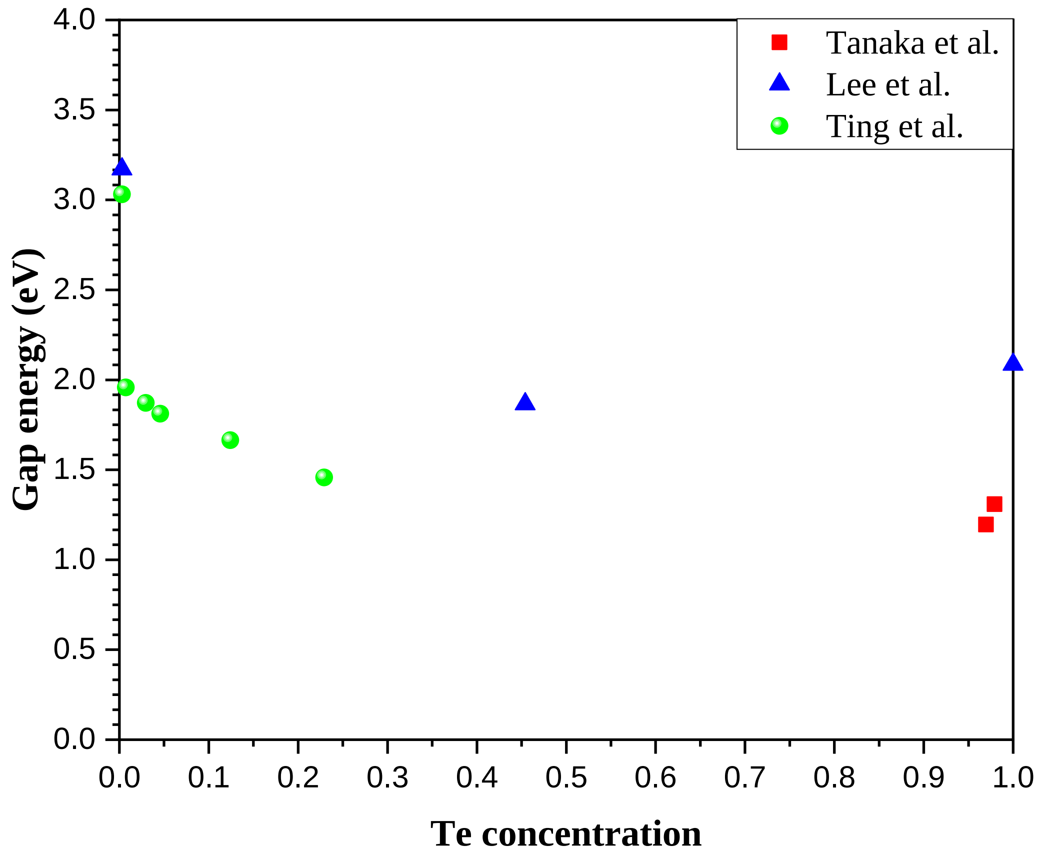

Figure I.10 Changes in bandgap energy as a function of 'Te' content in the $ZnO_{1-x}Te_x$ ternary alloys **[73,76,77]**.

I.6 Conclusion

In this chapter, we have introduced and discussed key parameters of various binary materials such as ZnO, ZnS, ZnSe and ZnTe as well as ternary materials like ZnOS, ZnOSe and ZnOTe. Understanding the crystalline structure and the energy band gap of these semiconductor compounds is of paramount importance. By comprehending these parameters, we can gain valuable insights into the optical and electronic behavior of these materials. It has been shown in this chapter that some of the physical properties of ternary alloys, such as the lattice parameter and gap energy of $ZnO_{1-x}S_x$, $ZnO_{1-x}Se_x$ and $ZnO_{1-x}Te_x$, can be determined by linear interpolation between their binary constituents. Furthermore, any deviation from this linearity can be described by a bowing parameter

Throughout the years, many theoretical methods have been employed for understanding the properties of materials, among these theoretical approaches, notable ones include the virtual crystal approximation (VCA), pseudopotential semi-empirical model, and more. One particularly powerful method that has gained significant traction over the past few decades is known as density functional theory (DFT). It has emerged as a widely utilized theoretical tool for comprehensively describing and analyzing the structural, electronic, and optical properties of physical and chemical systems. In the following chapter, we'll get into the details of this theoretical method and look closely at how it can be used.

I.7 References

[1] SI Inamdar et al., **Superlattices Microstruct.** 76, 253 (2014).
[2] H Bong et al., **Appl. Phys. Lett.** 96 (19), 192115 (2010).
[3] JM Lin et al., **Appl. Surf. Sci.** 255 (13), 6460 (2009).
[4] Y Ryu et al., **Appl. Phys. Lett.** 88 (24) (2006).
[5] Ü Özgür et al., **J. Appl. Phys.** 98 (4) (2005).
[6] A Samavati et al., **J. mater. sci. eng., B** 263, 114811 (2021).
[7] M Sowjanya et al., **Acta Phys. Pol. A** 137 (3) (2020).
[8] V Pawar et al., **Phys. Rev. Appl.** 9 (5), 054001 (2018).
[9] A Sáenz-Trevizo et al., **Mater. Res.** 19 (2016).
[10] T Makino et al., **Appl. Phys. Lett.** 78 (9), 1237 (2001).
[11] S Choopun et al., **Appl. Phys. Lett.** 80 (9), 1529 (2002).
[12] K Sakurai et al., **J. Cryst. Growth** 237-239, 514 (2002).
[13] J Wang and M Isshiki, in *Springer Handbook of Electronic and Photonic Materials*, edited by Safa Kasap and Peter Capper (Springer US, Boston, MA, 2007), pp. 325.
[14] H Morkoç and Ü Özgür, *Zinc oxide: fundamentals, materials and device technology*. (John Wiley & Sons, 2008).
[15] A-B Chen and A Sher, *Semiconductor alloys: physics and materials engineering*. (Springer Science & Business Media, 1995).
[16] M Lenglet, **Act. Passiv. Electron** 27, 1 (2004).
[17] MC Tamargo, *II-VI semiconductor materials and their applications*. (CRC Press, 2002).
[18] C Kittel and P McEuen, *Introduction to solid state physics*. (John Wiley & Sons, 2018).
[19] LP Bouckaert et al., **Phys. Rev.** 50 (1), 58 (1936).
[20] A Bachiri, Montouri-Constantine, 2006.
[21] PS Kireev, *Semiconductor Physics*. (Mir Publishers, 1975).
[22] F Aymerich, **Phys. Rev. B** 26 (4), 1968 (1982).
[23] H ABID, Djillali Liabes-Sidi-Bel-Abbes, 1997.
[24] S Adachi, *Properties of semiconductor alloys: group-IV, III-V and II-VI semiconductors*. (John Wiley & Sons, 2009).
[25] H Mathieu and H Fanet, *Physique des semiconducteurs et des composants électroniques - 6ème édition: Cours et exercices corrigés*. (Dunod, 2009).
[26] S Bloom and I Ortenburger, **Phys. Status Solidi B** 58 (2), 561 (1973).
[27] D Reynolds et al., **Phys. Rev. B** 60 (4), 2340 (1999).
[28] M JABERI et al., **Mod. Phys. Lett. B** 28 (04), 1450027 (2014).
[29] A Ashrafi and C Jagadish, **J. Appl. Phys.** 102 (7) (2007).
[30] JE Bernard and A Zunger, **Phys. Rev. B** 36 (6), 3199 (1987).
[31] L Vegard, **Z. Phys.** 5 (1), 17 (1921).
[32] A Ebina et al., **Phys. Rev. B** 10 (6), 2495 (1974).
[33] T-M Hsieh et al., **J. Power Sources** 246, 443 (2014).
[34] C Bugot et al., presented at the 2015 IEEE 42nd Photovoltaic Specialist Conference (PVSC), 2015 (unpublished).
[35] HK Hong et al., **Sol. Energy Mater. Sol. Cells** 155, 43 (2016).
[36] P Sinsermsuksakul et al., **Appl. Phys. Lett.** 102 (5) (2013).
[37] KX Steirer et al., **Phys. Chem. Chem. Phys.** 17 (23), 15355 (2015).
[38] HH Park et al., **Prog Photovolt** 23 (7), 901 (2015).
[39] OK Echendu and IM Dharmadasa, **Energies** 8 (5), 4416 (2015).
[40] AA Ojo and IM Dharmadasa, **Sol Energy** 158, 721 (2017).
[41] IO Oladeji et al., **Sol. Energy Mater. Sol. Cells** 61 (2), 203 (2000).

[42] X-B Xu et al., **Superlattices Microstruct.** 109, 463 (2017).
[43] Y-Z Yoo et al., **Appl. Phys. Lett.** 81 (20), 3798 (2002).
[44] L Zhang et al., **J. Alloys Compd.** 617, 413 (2014).
[45] Y He et al., **J. Alloys Compd.** 534, 81 (2012).
[46] K Ogata et al., **J. Cryst. Growth** 251 (1), 623 (2003).
[47] W Chen et al., **Appl. Phys. A** 115 (3), 817 (2014).
[48] M Wraback et al., **Appl. Phys. Lett.** 74 (4), 507 (1999).
[49] CR Gorla et al., **J. Appl. Phys.** 85 (5), 2595 (1999).
[50] Y Li et al., **J. Cryst. Growth** 375, 104 (2013).
[51] J Zúñiga-Pérez et al., **J. Appl. Phys.** 99 (2) (2006).
[52] M Li et al., **J. Alloys Compd.** 630, 106 (2015).
[53] J Chen et al., **J. Alloys Compd.** 773, 443 (2019).
[54] J Chen et al., **Appl. Phys. Lett.** 115 (8) (2019).
[55] BK Meyer et al., **Appl. Phys. Lett.** 85 (21), 4929 (2004).
[56] HL Pan et al., **Appl. Surf. Sci.** 256 (14), 4621 (2010).
[57] H Xu et al., **J. Appl. Phys.** 114 (8) (2013).
[58] G Baldissera and C Persson, **J. Appl. Phys.** 119 (4) (2016).
[59] J Zhu et al., **Carbon** 115, 1 (2017).
[60] C Persson et al., **Phys. Rev. Lett.** 97 (14), 146403 (2006).
[61] T Zhang et al., **Mater. Sci. Eng. R Rep.** 147, 100661 (2022).
[62] K Iwata et al., **Phys. Status Solidi B** 229 (2), 887 (2002).
[63] Y Nabetani et al., **Appl. Phys. Lett.** 83 (6), 1148 (2003).
[64] W Shan et al., **Appl. Phys. Lett.** 83 (2), 299 (2003).
[65] C-Y Chen et al., **J. Cryst. Growth** 378, 180 (2013).
[66] MA Mayer et al., **Appl. Phys. Lett.** 97 (2) (2010).
[67] MA Mayer et al., **J. Appl. Phys.** 111 (11) (2012).
[68] J-c Lee et al., **J. Alloys Compd.** 585, 94 (2014).
[69] A Polity et al., **Phys. Status Solidi A** 203 (11), 2867 (2006).
[70] M Welna et al., **Appl. Phys. Express** 7 (7), 071202 (2014).
[71] C-Z Zhao et al., **Physica B Condens. Matter** 502, 21 (2016).
[72] T Tanaka et al., **Appl. Phys. Lett.** 102 (5) (2013).
[73] T Tanaka et al., **Appl. Phys. Lett.** 100 (1) (2012).
[74] JC Slater, **J. Chem. Phys.** 41 (10), 3199 (2004).
[75] Y Nabetani et al., **Phys. Status Solidi A** 203 (11), 2653 (2006).
[76] D Uk Lee et al., **Appl. Phys. Lett.** 103 (26) (2013).
[77] M Ting et al., **Appl. Phys. Lett.** 106 (9) (2015).
[78] O Sánchez et al., **MRS Adv.** 2 (53), 3111 (2017).
[79] CP Liu et al., **J. Alloys Compd.** 852, 156950 (2021).
[80] NA Noor et al., **Comput. Mater. Sci.** 93, 151 (2014).
[81] D Long et al., **Mater. Res. Express.** 4 (5), 055901 (2017).

Chapter II Calculation method

II.1 Introduction

Over the past few decades, significant advancements in computational techniques have revolutionized our understanding of complex structures of matter. The properties of materials, at their most fundamental level, are governed by the complex interactions between electrons and nuclei. To grasp these phenomena and predict material behavior, quantum mechanics stands as an indispensable tool, offering a profound description of material behavior.

The foundation of quantum mechanics was laid in the early 20th century by intuitive scientists such as Bohr, De Broglie, Schrödinger, and Dirac **[1-5]**. Their groundbreaking contributions paved the way for modern theoretical approaches. Central to quantum mechanical calculations, the Schrödinger equation **[1]** provides a fundamental framework. However, for systems with a multitude of particles, analytical solutions become elusive, necessitating alternative strategies.

Enter first-principle methods, or ab-initio methods, which have emerged as essential resources for calculating the structural and electronic properties of intricate systems. These techniques, now a cornerstone of materials research, have revolutionized the prediction of novel materials, offering a cost-effective and practical alternative to traditional laboratory experiments.

The scientific community's growing reliance on first-principle methods is evident in the exponential increase in related publications over the years **[6]**. As one successful and popular approach which is shown by **Figure II.1**, Density Functional Theory (DFT), conceptualized by Hohenberg and Kohn **[7]**, has played a pivotal role in calculating material properties from electronic density. Its versatility and reliability have been acknowledged by the Nobel Prize, awarded to Walter Kohn for his exceptional contributions to the development of DFT **[8-9]**.

The implementation of these theoretical concepts into practical simulations requires specialized codes, such as Wien2k, Quantum Espresso, VASP, and CASTEP. These codes enable the simulation of molecular and material properties, offering invaluable insights into the behavior of complex systems.

In this chapter, we embark on a comprehensive exploration of first principles calculations, uncovering the approximations utilized in the Schrödinger equation to describe materials. Additionally, we delve into the intricacies of DFT and the Kohn-Sham equations, investigating the critical issue of exchange and correlation. We dedicate considerable attention to the solution of Kohn-Sham equations, a vital aspect of practical applications.

Furthermore, we introduce the FP-LAPW (Full-Potential Linearized Augmented Plane Wave) method, with a particular emphasis on the Wien2k code [10]; a powerful and widely adopted tool that lies at the heart of the chapter's demonstrations and case studies.

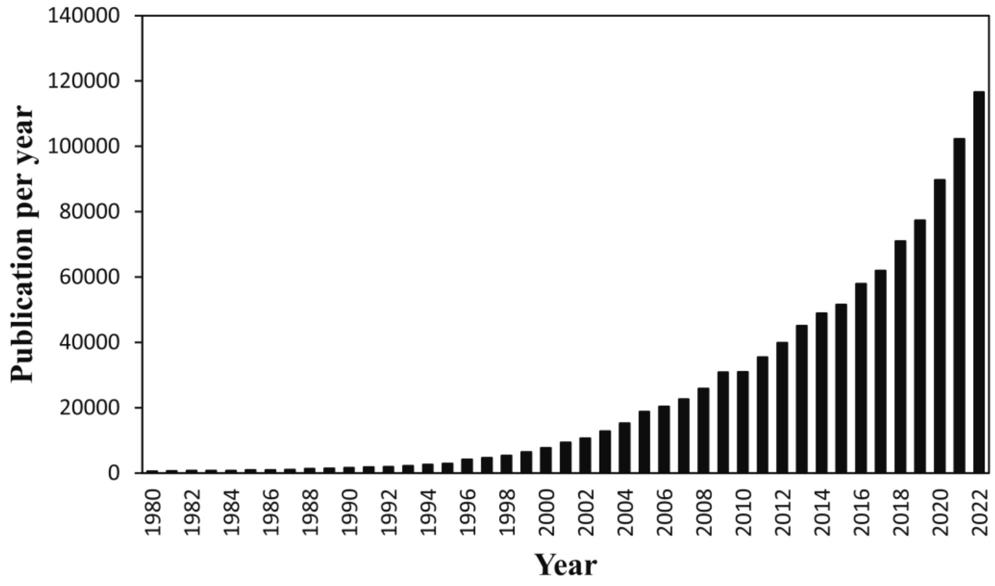

Figure II.1 Number of papers that mention DFT [6].

II.2 Many-Body Schrödinger Equation

The foundation for investigating a quantum mechanical system involves the resolution of the Schrödinger equation, first introduced by Erwin Schrödinger in 1926 [1]. In the realm of materials science, the challenge lies in solving the time-independent many-body Schrödinger equation within the non-relativistic framework. Let's consider a material consisting of M nuclei, collectively represented by spatial coordinates $\vec{R} = \{\vec{R}_1, \vec{R}_2, \ldots, \vec{R}_M\}$, and N electrons, each having spatial coordinates $\vec{r} = \{\vec{r}_1, \sigma_1, \ldots \vec{r}_N, \sigma_N\}$ and a spin σ_i. The wave function, which depends on the positions of all the particles in the system, contains all the important information about this system. To simplify, we denote the wave function as $\psi(\vec{r}, \vec{R})$, and the time-independent Schrödinger equation is expressed as follow:

$$\hat{H}\psi(\vec{r}, \vec{R}) = E\psi(\vec{r}, \vec{R}) \tag{II.1}$$

Where $\hat{H}$ is the Hamiltonian operator, and its equal to:

$$\hat{H} = \hat{T}_n + \hat{T}_e + \hat{V}_{n-n} + \hat{V}_{n-e} + \hat{V}_{e-e} \quad \text{(II.2)}$$

Where:

$\hat{T}_n = -\frac{\hbar^2}{2}\sum_I \frac{\nabla_I^2}{M_I}$: is the kinetic energy operator for atoms.

$\hat{T}_e = -\frac{\hbar^2}{2m}\sum_i \nabla_i^2$: is the kinetic energy operator for electrons.

$\hat{V}_{n-n} = \frac{1}{4\pi\epsilon_0}\sum_{I\neq J} \frac{Z_I Z_J}{|\vec{R}_I - \vec{R}_J|}$: the potential energy operator for nuclear-nuclear interaction.

$\hat{V}_{n-e} = -\frac{e}{4\pi\epsilon_0}\sum_{i,I} \frac{Z_I}{|\vec{r}_i - \vec{R}_I|}$: the potential energy operator for nuclear-electron interaction.

$\hat{V}_{e-e} = \frac{e^2}{4\pi\epsilon_0}\sum_{i\neq j} \frac{1}{|\vec{r}_i - \vec{r}_j|}$: the potential energy operator for electron-electron interaction.

Where M and Z refers to the mass and the charge of the nucleus, m and e to the mass and the charge of the electron, r to distance, the subscripts I, J and i, j refer to nuclei and electrons respectively, ∇^2 is the Laplacian operator, which in cartesian coordinates has the form:

$$\nabla^2 = \frac{\partial^2}{\partial x^2} + \frac{\partial^2}{\partial y^2} + \frac{\partial^2}{\partial z^2} \quad \text{(II.3)}$$

To simplify we use the atomic units where $4\pi\varepsilon_0 = \hbar = m_e = e = 1$. Also, we use the notation $r_{IJ} = |\vec{R}_I - \vec{R}_J|, r_{iI} = |\vec{r}_i - \vec{R}_I|, r_{ij} = |\vec{r}_i - \vec{r}_j|$. The Hamiltonian operator will become:

$$\hat{H} = -\frac{1}{2}\sum_I \frac{\nabla_I^2}{M_I} - \frac{1}{2}\sum_i \nabla_i^2 + \sum_{I\neq J} \frac{Z_I Z_J}{r_{IJ}} - \sum_{i,I} \frac{Z_I}{r_{iI}} + \sum_{i\neq j} \frac{1}{r_{ij}} \quad \text{(II.4)}$$

II.3 Born-Oppenheimer approximation

The first fundamental approach to tackle the many-body problem was put forth by Born and Oppenheimer in 1927 **[11]**. As electrons are significantly lighter and less massive than nuclei (with the proton being about 1800 times heavier than an electron), the nuclei move at a much slower pace compared to electrons. This difference in mass allows us to consider nuclei as essentially stationary particles, permitting the separation of motion between nuclei and electrons. Consequently, it becomes reasonable to treat electrons as moving within the influence of fixed nuclei in an external field.

This approximation, known as the Born-Oppenheimer approximation, involves neglecting the kinetic energy term for the nuclei, effectively treating it as zero, and considering the nucleus-nucleus Coulomb term as a constant, which can be negated by appropriately choosing the origin of potential energy. Within the Born-Oppenheimer approximation, the electronic Hamiltonian takes the following form:

$$\hat{H}_e = \hat{T}_e + \hat{V}_{n-e} + \hat{V}_{e-e} \tag{II.5}$$

In this approximation, the wave function can be expressed as the product of two components, the electronic component and the nuclear component:

$$\psi(\vec{r}, \vec{R}) = \psi_e(\vec{r}; \vec{R})\psi_n(\vec{R}) \tag{II.6}$$

And the Schrödinger equation for the electronic motion became:

$$\hat{H}_e\psi_e = E_e\psi_e \tag{II.7}$$

Despite these simplifications, the resolution of this equation remains extremely difficult because for a system with *N* electrons it depends on *3N* space coordinates. This is why it is very often coupled with other approximations.

II.4 Hartree approximation

In 1928, Hartree **[12]** formulated the complete wave function of the electronic system ψ_e as the direct multiplication of the wave functions corresponding to each individual electron $\phi_i(\vec{r}_i)$; The wave functions, known as orbitals, describe the independent motion of each electron within a field generated by other electrons and nuclei. By employing this approximation, the complex many-body problem is simplified into a more manageable one-electron problem. Consequently, the total electronic wave function can be expressed as follow:

$$\psi_e(\vec{r}_1, \vec{r}_2, \dots \dots, \vec{r}_N) = \phi_1(\vec{r}_1) \dots \dots \phi_N(\vec{r}_N) = \prod_i \phi_i(\vec{r}_i) \tag{II.8}$$

And using variational principle, we can find the Schrödinger equation for the single electron:

$$\left(-\frac{1}{2}\nabla^2 + \hat{V}_H(\vec{r}_i) + \hat{V}_{ext}(\vec{r}_i)\right)\phi_i(\vec{r}) = \varepsilon_i\phi_i(\vec{r}) \tag{II.9}$$

Where the individual Hamiltonian of each electron is:

$$\hat{h}_i = -\frac{1}{2}\nabla_i^2 + \hat{V}_H(\vec{r}_i) + \hat{V}_{ext}(\vec{r}_i) \tag{II.10}$$

$\hat{V}_H$ is referred to as the Hartree potential; it is the classical Coulomb interaction operator produced by the charge density $\rho(\vec{r}\,') = \sum_j \left|\phi_j(\vec{r}\,')\right|^2$:

$$\hat{V}_H = \sum_j \int \frac{\left|\phi_j(\vec{r}\,')\right|^2}{|\vec{r} - \vec{r}\,'|} dr' = \int \frac{\rho(\vec{r}\,')}{|\vec{r} - \vec{r}\,'|} d^3r' \tag{II.11}$$

The operator $\hat{V}_{ext}$ represents the external potential that arises from the presence of the nuclei:

$$\hat{V}_{ext}(r) = -\sum_J \frac{Z_I}{\left|r - R_J\right|} \tag{II.12}$$

The global Hamiltonian $\hat{H}_e$ is written in the form of the sum of monoelectronic Hamiltonians:

$$\hat{H}_e = \sum_i \hat{h}_i \tag{II.13}$$

And using the relation $E_e = \langle \psi_e | \hat{H}_e | \psi_e \rangle$ we can find the total electronic energy:

$$E_e = T_e + E_H + E_{ext} \tag{II.14}$$

The Hartree approximation is based on the idea that electrons can be treated as independent particles, disregarding any interactions between electrons and their respective spin states. This assumption has two notable implications:

1- The total Coulomb repulsion ($\hat{V}_{e-e}$) within the electronic system is overestimated.
2- The Pauli exclusion principle is not considered in the approximation.

This second consequence is more serious than the first. Because electrons are fermions, they have to obey The Pauli exclusion principle which states that it is prohibited for two electrons to possess the same quantum state **[13]**. Consequently, their wave function is antisymmetric, and it has to follow this equation when electrons exchange positions:

$$\psi_e(\vec{r}_1, \vec{r}_2 \dots \vec{r}_i, \vec{r}_j \dots \vec{r}_N) = -\psi_e(\vec{r}_1, \vec{r}_2 \dots \vec{r}_j, \vec{r}_i \dots \vec{r}_N) \tag{II.15}$$

II.5 Hartree-Fock approximation

Fock (1930) **[14]** provided direct proof that the Hartree wave function (**Equation II.9**) is in conflict with the Pauli exclusion principle due to its lack of antisymmetry concerning the exchange of two electrons. An alternative approach was introduced, involving the energy minimization using a Slater determinant **[15]**. In this method, combining single-electron wave functions while upholding the antisymmetry principle results in the formation of the N-electron wave function. The Hartree-Fock approximation is the name of this improved approach. The Hartree-Fock many-electron wave function is then:

$$\psi(\vec{r},\sigma) = \frac{1}{\sqrt{N!}}\begin{vmatrix} \phi_1(\vec{r}_1,\sigma_1) & \phi_1(\vec{r}_2,\sigma_2) & \phi_1(\vec{r}_3,\sigma_3) & \cdots & \phi_1(\vec{r}_N,\sigma_N) \\ \phi_2(\vec{r}_1,\sigma_1) & \phi_2(\vec{r}_2,\sigma_2) & \phi_2(\vec{r}_3,\sigma_3) & \cdots & \phi_2(\vec{r}_N,\sigma_N) \\ \vdots & \vdots & \vdots & \ddots & \vdots \\ \phi_N(\vec{r}_1,\sigma_1) & \phi_N(\vec{r}_2,\sigma_2) & \phi_N(\vec{r}_3,\sigma_3) & \cdots & \phi_N(\vec{r}_N,\sigma_N) \end{vmatrix} \quad \text{(II.16)}$$

plug it into the Schrödinger equation we find:

$$\left[-\frac{1}{2}\nabla^2 + \hat{V}_H(\vec{r}_i) + \hat{V}_{ext}(\vec{r}_i)\right]\phi_i(\vec{r}) - \sum_j \int \frac{\phi_j^*(\vec{r}\,')\phi_i(\vec{r\,'})}{|\vec{r}\,' - \vec{r}|}\phi_j(\vec{r})dr' = E_n\phi_n(\vec{r}) \quad \text{(II.17)}$$

Comparing this equation with Hartree equations we notice an extra term which is:

$$\hat{V}_x(\vec{r}_i)\phi_i(\vec{r}) = -\sum_j \int \frac{\phi_j^*(\vec{r}\,')\phi_i(\vec{r\,'})}{|\vec{r}\,' - \vec{r}|}\phi_j(\vec{r})dr' \quad \text{(II.18)}$$

It is called the non-local exchange potential, which describes the effects of exchange between electrons. It corrects the defect of the Hartree approximation, but it considerably complicates the calculations. Consequently, we can write the total electronic energy as follow:

$$E_e = T_e + E_H + E_{ext} + E_x \quad \text{(II.19)}$$

The Hartree-Fock approximation takes into consideration the exchange energy, but ignores the existing correlation energy between the electrons. We can also define this type of energy as being the difference between the exact total energy and that provided by the Hartree-Fock approximation. The inclusion of this unknown energy is proven by density functional theory (DFT).

II.6 Density functional theory

Density Functional Theory (DFT) revolves around the fundamental concept that the energy of an electronic system can be represented as a function of its density. This foundational idea traces its origins back to the early contributions of Thomas **[16]** and Fermi **[17]** in 1927, where the exchange and correlation effects between electrons were initially neglected. However, Dirac **[18]** addressed this limitation in 1930 by introducing the local exchange approximation.

Later, DFT was formally established with the groundbreaking publications of Hohenberg and Kohn in 1964 **[7]**, and Kohn and Sham in 1965 **[9]**, which laid the foundation for the theory. The primary objective of DFT is to establish the ground state properties of a system containing a set of interacting electrons in an external field caused by the nuclei, solely based on the electron density information.

The accurate treatment of electron correlations is one of the strengths of DFT, which makes it an effective tool for grasping the behavior of electronic systems.

II.6.1 Hohenberg-Kohn theorems

The formalism of density functional theory (DFT) is based on two fundamental theorems stated and demonstrated by Hohenberg and Kohn **[7]**.

Theorem 1 (Uniqueness): « *the external potential $\hat{V}_{ext}$ is (to within a constant) a unique functional of $\rho(\vec{r})$* »

According to the first theorem, the external potential of a quantum system is uniquely determined by the density of its electrons in the ground state. In simpler terms, if you have the electron density distribution of a many-electron system at its lowest energy state (ground state), you can determine the potential energy that the electrons are experiencing due to the combined effects of external fields such as the nuclei. This potential is called the external potential $\hat{V}_{ext}$. Consequently, the total energy can be written as a unique functional of $\rho(\vec{r})$ as follow:

$$E[\rho] = F_{HK}[\rho] + \int \hat{V}_{ext}\, \rho(\vec{r}) d^3r \tag{II.20}$$

Where:

$$F_{HK}[\rho] = \langle \Psi_e | \hat{T}_e + \hat{V}_{ee} | \Psi_e \rangle \tag{II.21}$$

$F_{HK}[\rho]$ is universal functional of the $\rho(\vec{r})$, that is, it is the same for all electronic structure problems. since it is independent of external potential $\hat{V}_{\text{ext}}$. This functional includes both the exchange and correlation effects.

Theorem 2 (Variational principle): « *For a given external potential, the true density* $\rho_0(\vec{r})$ *minimizes the total energy functional* ».

The second theorem extends the first one by stating that there is unique value of electronic density that we can solely express with it the ground state energy of a system. Which means that the ground sate energy is independent from the wave functions of the individual electrons. Mathematically, the second theorem may be expressed as follows:

$$E_0 = minE[\rho(\vec{r})] = E[\rho_0(\vec{r})] \tag{II.22}$$

II.7 Kohn-Sham equations

The theorems established by Hohenberg and Kohn demonstrate the existence of a precise solution for the ground state of a given system. However, these theorems do not provide a practical methodology for its computational determination. Nevertheless, in the year 1965, Kohn and Sham **[9]** proposed a concept that allowed to turn DFT into a real computational tool. Kohn and Sham proposed a scheme to evaluate $F_{HK}[\rho]$ that is analogous to the Hartree-Fock's method, in this scheme, one can decompose this $F_{HK}[\rho]$ as follow:

$$F_{HK}[\rho] = T_s[\rho(\vec{r})] + E_H[\rho(\vec{r})] + E_{xc}[\rho(\vec{r})] \tag{II.23}$$

Here T_s is the kinetic energy of a free electron gas (non-interacting electrons), E_H represents the Hartree contribution and E_{xc} is called the exchange-correlation energy. This energy incorporates the total errors arises from the combined effects of inaccuracies in employing a non-interacting kinetic energy and in addressing the electron-electron interaction in a classical manner. Consequently, total energy became:

$$E[\rho] = T_s[\rho(\vec{r})] + E_H[\rho(\vec{r})] + E_{xc}[\rho(\vec{r})] + E_{ext}[\rho(\vec{r})] \tag{II.24}$$

The only term that remains unknown is E_{xc}, which is not easy to calculate, but as we verify the advantage of being much smaller in front of the other terms. Using the variational principle, we finally obtain the single-particle Kohn-Sham equation:

$$\left\{-\frac{\hbar^2}{2m}\nabla_i^2 + V_{eff}^{KS}(\vec{r})\right\}\phi_i(\vec{r}) = \varepsilon_i\phi_i(\vec{r}) \tag{II.25}$$

Here:

$$\hat{V}_{eff}^{KS}(\vec{r}) = \hat{V}_H(\vec{r}) + \hat{V}_{ext}(\vec{r}) + \hat{V}_{xc}(\vec{r}) \quad \text{(II.26)}$$

And we get the Schrödinger-like Kohn-Sham equations:

$$\hat{H}^{KS}\varphi_i(\vec{r}) = \varepsilon_i\varphi_i(\vec{r}) \quad \text{(II.27)}$$

Where:

$\hat{H}^{KS} = -\frac{\hbar^2}{2m}\nabla_i^2 + V_{eff}^{KS}(\vec{r})$ is the Kohn-sham Hamiltonian.

$\hat{V}_{eff}^{KS}(\vec{r})$ is called the Kohn-Sham effective potential operator.

$\hat{V}_H(\vec{r}) = \frac{\delta E_H[\rho(\vec{r})]}{\delta\rho(\vec{r})} = \int \frac{\rho(\vec{r}')}{|\vec{r}-\vec{r}|} d^3r'$ is Hartree potential operator.

$\hat{V}_{ext}(\vec{r}) = \frac{\delta E_{ext}[\rho(\vec{r})]}{\delta\rho(\vec{r})} = \sum_J \frac{Z_J}{|\vec{r}-\vec{R}_J|}$ is the external potential operator.

$\hat{V}_{xc}(\vec{r}) = \frac{\delta E_{xc}[\rho(\vec{r})]}{\delta\rho(\vec{r})}$ is the exchange-correlation potential operator.

The KS scheme basic idea is to map the complex, interacting electronic systems into a set of fictitious non-interacting particles ($V_{e-e} = 0$) in an external effective potential V_{eff}^{KS} (see **Figure II.2**).

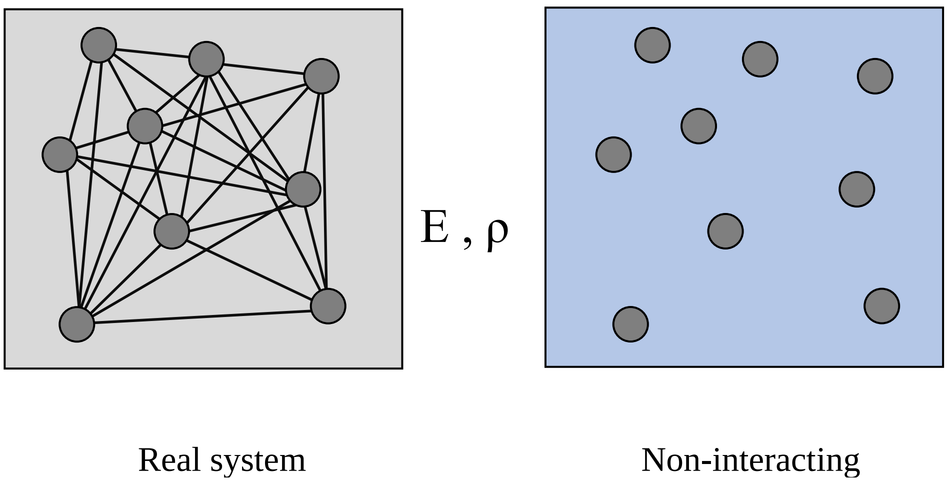

Figure II.2 Relationship between: (Left Side) Real Many-Body System, (Right Side) Kohn-Sham non-Interacting System.

II.8 Exchange-correlation functional

As mentioned earlier, at the Khon-Sham equations stage, Density Functional Theory (DFT) represents a completely accurate theory were the ground state energy of a system can be described uniquely by electronic density. However, despite this precision, DFT faces limitations as the exchange-correlation potential, which includes the correction to kinetic energy, remains unknown.

Nevertheless, this challenge can be overcome through approximations. Throughout history, various exchange-correlation functionals have been proposed and considered to address this issue. These functionals aim to approximate the elusive exchange-correlation potential, thereby making DFT practically applicable in a wide range of scenarios.

II.8.1 Local density approximation (LDA)

This approximation was firstly introduced by Kohn and Sham **[9]**. is based on the idea that the electron density exhibits slow spatial variations. Consequently, the exchange-correlation components are determined uniquely by the local density value $\rho(\vec{r})$. This approach considers a system which is non-homogeneous in total as locally homogeneous. The exchange-correlation energy within LDA is denoted by the following expression:

$$E_{xc}^{LDA}[\rho(\vec{r})] = \int \rho(\vec{r})\epsilon_{xc}[\rho(\vec{r})]d^3r \tag{II.28}$$

The exchange-correlation energy ϵ_{xc} can be separated into an "exchange" term ϵ_x and a "correlation" term ϵ_c:

$$\epsilon_{xc}^{LDA}[\rho(\vec{r})] = \epsilon_x[\rho(\vec{r})] + \epsilon_c[\rho(\vec{r})] \tag{II.29}$$

The exchange contribution was originally derived by Dirac [18]:

$$\varepsilon_x[\rho] = -\frac{3}{4}\left(\frac{3}{\pi}\right)^{1/3}\rho^{1/3} = -\frac{3}{4}\left(\frac{9}{4\pi^2}\right)^{1/3}\frac{1}{r_s} \tag{II.30}$$

Here $r_s = \left(\frac{4\pi\rho}{3}\right)^{-1/3}$ is the Wigner-Seitz radius **[19]** (radius of a sphere that contains one electron).

The variational quantum Monte-Carlo (VQMC) calculations performed by Ceperley and Alder **[20]** have allowed for the precise determination of the correlation energy $\epsilon_c[\rho(\vec{r})]$ in the homogeneous electron gas. These values were subsequently interpolated by Wigner

[19], and then by Vosko, Wilk, and Nusair (VWN) [21], as well as by Perdew and Zunger [22], to arrive at an analytical form of $\epsilon_c[\rho(\vec{r})]$.

In order to account for spin dependence, the local spin-density approximation (LSDA) was developed, leading to better descriptions of unpaired electrons in alkali metals [23]. As a result, the cohesive energy of solids is improved [24]. Proposed by Kohn and Sham [9], this approximation has shown remarkable accuracy and utility, especially in solid-state physics calculations. It is widely used in this field and takes the following form:

$$E_{xc}^{LSDA}[\rho] = \int \varepsilon_{xc}[\rho\uparrow, \rho\downarrow]\rho(\vec{r})d^3r \qquad \text{(II.31)}$$

II.8.2 Generalized Gradient Approximation (GGA)

It has been noticed that the exchange-correlation potential in the LDA only depends on the local density (constant through space). However, in practice, real systems exhibit spatial inhomogeneity in their electron density. Incorporating a correction to this functional that accounts for the rate of variation of $\rho(\vec{r})$ would therefore be more appropriate. By include variables that depend on the density gradient in the exchange-correlation energy, this improvement takes the inhomogeneity of the electron density into account and that is what the Generalized Gradient Approximation (GGA) do. it provides a balance between the local and gradient-dependent terms. The energy that links the local electron density function $\rho(\vec{r})$ and its gradient $d\rho(\vec{r})$ is given by the following formula:

$$E_{xc}^{GGA} = \int \rho(\vec{r})\varepsilon_{xc}^{GGA}[\rho(\vec{r}), \vec{\nabla}\rho(\vec{r})]d\vec{r} \qquad \text{(II.32)}$$

The energy ε_{xc}^{GGA} is a functional of local charge density and also local charge density gradient. We can rewrite the exchange-correlation energy under GGA approximation as follow:

$$E_{xc}^{GGA} = \int \rho(\vec{r})\epsilon_x[\rho(\vec{r})]F_{xc}[\rho(\vec{r}), \vec{\nabla}\rho(\vec{r})]d\vec{r} \qquad \text{(II.33)}$$

Here $\epsilon_x[\rho(\vec{r})]$ represents the exchange energy and $F_{xc}[\rho(\vec{r}), \vec{\nabla}\rho(\vec{r})]$ is called the enhancement factor.

There are many forms of F_{xc}, among them those of Perdew et al. (1991) [25], Wu-Cohen (WC) [26] and Engel Vosko (EV) [27]. The most frequently used are those introduced by Becke (B88) [28], Perdew and Wang [29] and Perdew-Burke-Ernzerhof [30].

II.8.3 Wu and Cohen's generalized gradient approximation (WC-GGA)

This new approximation is employed by Z. Wu and R. E. Cohen (WC) **[26]**, where the correlation energy functional is modified in combination with the PBE approximation **[30]**. This modification enhances the accuracy of structural properties compared to other approximations. The WC approximation possesses intriguing characteristics, primarily due to its GGA-like nature. The WC-GGA is easy to implement, computationally efficient, and does not involve adjustable parameters. We can write the enhancement factor for WC-GGA as follow:

$$F^{WC} = 1 + k - \frac{k}{1 + \frac{x}{k}} \tag{II.34}$$

Where $k = 0.804$:

$$x = \frac{10}{81}s^2 + \left(\mu - \frac{10}{81}\right)s^2 e^{-s^2} + ln\,(1 + cs^2) \tag{II.35}$$

Here: $s = |\nabla\rho|/\left[2(3\pi^2)^{1/3}\rho^{4/3}\right]$, $\mu = 0.21951$ and $c = 0.0079325$.

II.8.4 Modified Becke and Johnson potential (mBJ)

It is widely acknowledged that both LDA and GGA underestimate energy gaps. This is primarily due to their simple shapes. For establishing the precise shape of the exchange-correlation potential, these approximations prove to be insufficiently flexible. A revised version of the exchange potential initially proposed by Becke and Johnson **[31]** has been published by Tran and Blaha **[32]**. It's called the modified Becke and Johnson potential (mBJ) also known as the Tran Blaha potential. This approximation quickly proved its effectiveness compared to the mode of calculation most often used such as GGA **[29]**.

The form of the mBJ potential proposed by Tran and Blaha **[32]** is:

$$V_{x,\sigma}^{mBJ}(r) = cV_{x,\sigma}^{BR}(r) + (3c - 2)\frac{1}{\pi}\sqrt{\frac{5}{12}}\sqrt{\frac{2t_\sigma(r)}{\rho_\sigma(r)}} \tag{II.36}$$

Where: $\rho_\sigma(r)$ is electronic density, $t_\sigma(r)$ is the density of kinetic energy and $V_{x,\sigma}^{BR}(r)$ represents the Becke-Roussel potential **[33]** which has been suggested to simulate the Coulomb potential produced through the exchange hole. In this expression, c is equal to:

$$c = \alpha + \beta \left(\frac{1}{V_{cell}} \int_{cell} \frac{|\nabla \rho(r')|}{\rho(r')} d^3 r' \right)^{1/2} \quad \text{(II.37)}$$

Where: α and β are adjustable parameters α is dimensionless and β unit is Bohr$^{1/2}$ and V_{cell} is the unit cell volume.

II.9 Solving Kohn-Sham equations

To solve the Kohn and Sham **Equations II.27**, it is required to select a basis for the wave functions. This basis can be represented by a linear combination of orbitals known as Kohn-Sham (KS) orbitals, which can be expressed in the following form:

$$\phi_i = \sum_{p=1}^{P} c_p^i \phi_p^b \quad \text{(II.38)}$$

where c_p^i are constant coefficients. The process of solving the Kohn and Sham equations involves finding the coefficients c_p^i of the occupied electronic orbitals, which in turn minimize the total energy. Performing these calculations at the symmetry points in the first Brillouin zone allows for computational simplification. This iterative resolution is carried out through a self-consistent cycle of iterations, as shown in the flowchart of **Figure II.3**. Initially, the system begins with the injection of the initial charge density ρ_{in} to diagonalize the secular equation:

$$\begin{bmatrix} \cdots & \cdots & \cdots \\ \vdots & \langle \varphi_m | \hat{H}^{KS} | \varphi_n \rangle - \varepsilon_i \langle \varphi_m \mid \varphi_n \rangle & \vdots \\ \cdots & \cdots & \cdots \end{bmatrix} \begin{bmatrix} c_1^i \\ \vdots \\ c_P^i \end{bmatrix} = \begin{bmatrix} 0 \\ \vdots \\ 0 \end{bmatrix} \quad \text{(II.39)}$$

Or in the compact form:

$$\left(\hat{H}^{KS} - \varepsilon_i S \right) c_P^i = 0 \quad \text{(II.40)}$$

$\hat{H}^{KS}$: represents the Kohn-sham Hamiltonian matrix.

S: the overlap matrix.

Then the new charge density ρ_{in}, is built using the eigenvectors of the secular equation. The sum of the charge densities of all the occupied orbitals is used to calculate this density of charge. If ρ_{in} and ρ_{out} do not match, the two densities are mixed. The simplest mixing scheme is linear such as:

$$\rho_{in}^{i+1} = (1 - \alpha) \rho_{in}^{i} + \alpha \rho_{out}^{i} \quad \text{(II.41)}$$

Where i represents the iteration index and α represents the mixing parameter. Other methods employing the Jacobian or Hessian matrices are more effective than linear mixing. The family of Broyden mixing methods takes into consideration not only numerical details, but also algorithmic complexity, and iteratively updates the inverse Jacobian. Due to their effectiveness, Broyden-type mixing is widely used in modern approximations.

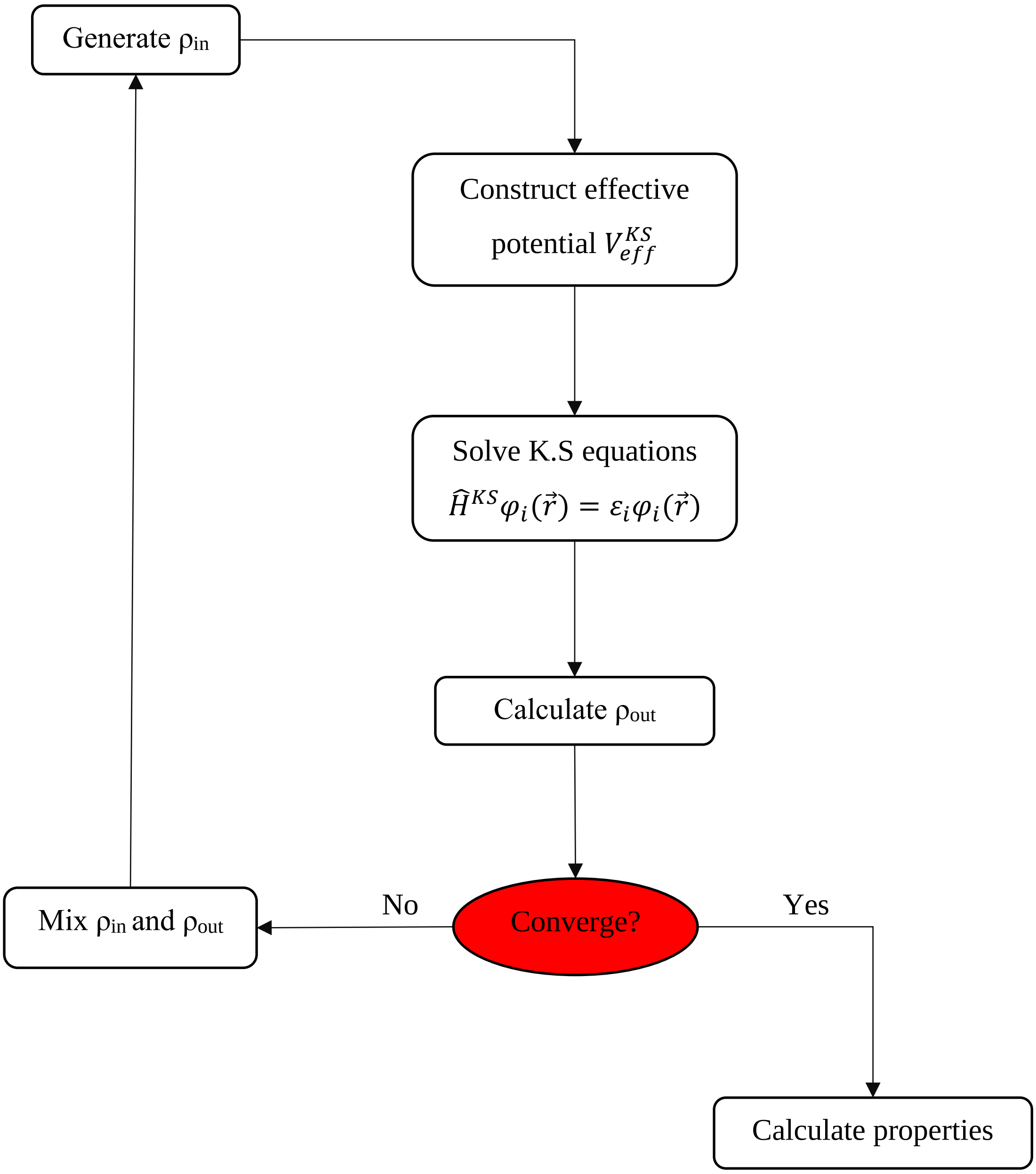

Figure II.3 Schematic representation of the self-consistent cycle.

II.10 DFT implementations

The pursuit of efficiently solving the Kohn-Sham equation has led to a diverse range of highly successful and effective electronic structure methods. To develop these methods, careful examination of the mathematical nature of the Schrödinger-like Kohn-Sham equation is crucial, considering the kinetic energy operator and the *1/r* singularity at the nucleus, while simultaneously addressing the determination of the exchange-correlation potential $\hat{V}_{xc}$ and the Hartree potential $\hat{V}_H$.

Finding a basis that is both unbiased and efficient is the ultimate quest of material simulation physics. The Kohn-Sham equation can be decomposed into a radial part and an angular part (represented by spherical harmonics) for use in atomic calculations, where it displays spherical symmetry for a particular electronic arrangement. Methods based on localised orbitals are commonly used when working with isolated clusters or molecules since they are in line with the chemical intuition of the system being studied **[34]**.

On the other hand, methods suitable for periodic solids often incorporate algorithms where the Bloch boundary condition can be included in the basis set. A plane-wave expansion of the Kohn-Sham wavefunctions is applied to benefit from the crystal's periodicity. The different methods that have been proposed to solve Schrödinger's equation are briefly summarised in **Figure II.4**.

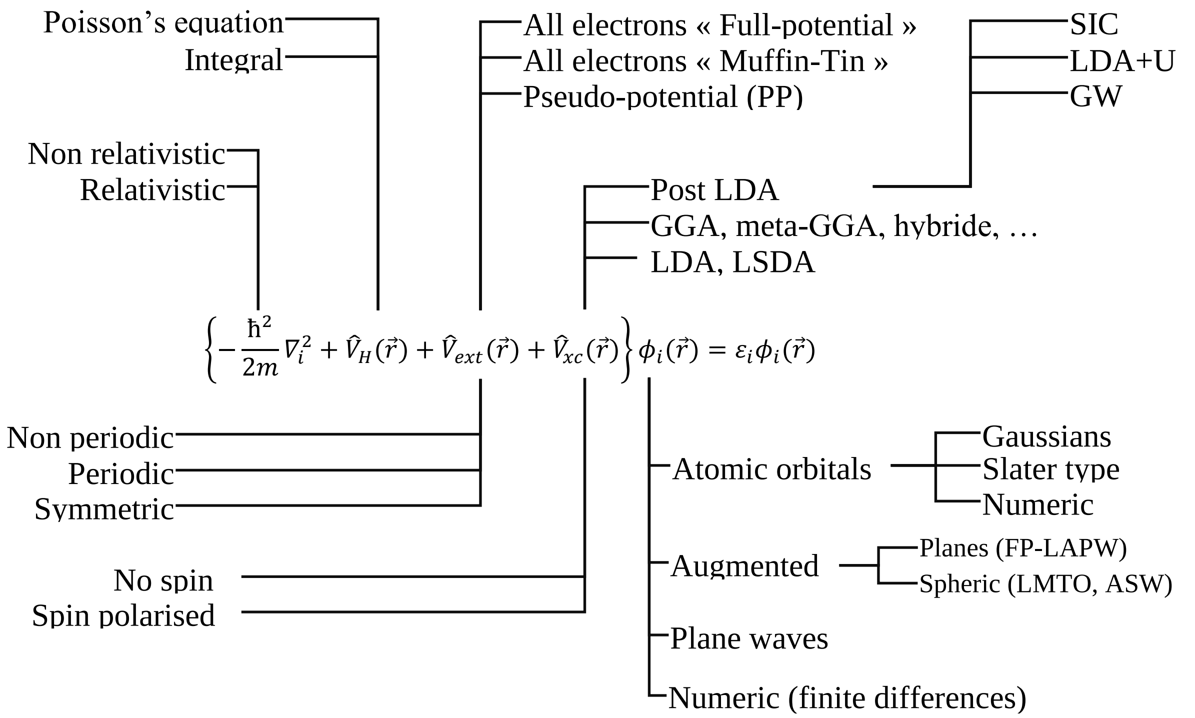

Figure II.4 Diagram illustrating different calculation methods based on Density Functional Theory.

II.11 Full-Potential Linearized Augmented Plane Wave Method (FP-LAPW)

Density functional theory is a powerful approach for dealing with many-body problems. However, selecting an appropriate basis set of wave functions is crucial for solving the Kohn-Sham equations. There are several methods available to solve the Schrödinger equation, differing in the shape of the potential used and the wave functions chosen as a basis. Among them are the Linear Combination of Atomic Orbitals (LCAO) methods **[35-36]**, suitable for treating transition metals. The Orthogonalized Plane Wave (OPW) methods and their derivatives **[36-37]** are applicable to the "*s-p*" character conduction bands of simple metals. Augmented Plane Wave (APW) methods with a cellular approach **[38]** are also used. Linearized Augmented Plane Wave (LAPW) methods **[39]** developed by Andersen, including Linearized Augmented Plane Waves (LAPW) and Linearized Muffin-Tin Orbitals (LMTO), offer significant computational speed improvements. The Linearized Augmented Plane Wave (LAPW) method **[40-41]** is a fundamental modification of Slater's Augmented Plane Wave (APW) method (1937-1964) **[42-43]**. Before delving into the LAPW method, let us start with a brief review of the APW method and its motivations within the LAPW method.

II.11.1 The Augmented Plane Wave method (APW)

Back in 1937, the Augmented Plane Wave (APW) method was introduced by the eminent physicist, Slater **[38]**. His proposal involved incorporating a radial by integrating the Muffin-tin approximation into the crystal potential. In essence, the unit cell was partitioned into two distinct regions, each serving a unique purpose.

- The first region, situated in close proximity to the atomic nucleus, has resemblance to an isolated atom in terms of potential and wave function characteristics. Within this spatial domain, which called the "Muffin-Tin" (MT) sphere and with a radius denoted as R_α, the potential demonstrated spherical symmetry while the wave functions took the form of radial functions. This allowed for a precise depiction of the localized behavior near atomic nuclei.

- The second region, referred to as the interstitial region (I), the potential was modeled as constant, facilitating the use of plane waves as the ideal wave functions for this region (as illustrated in **Figure II.5**).

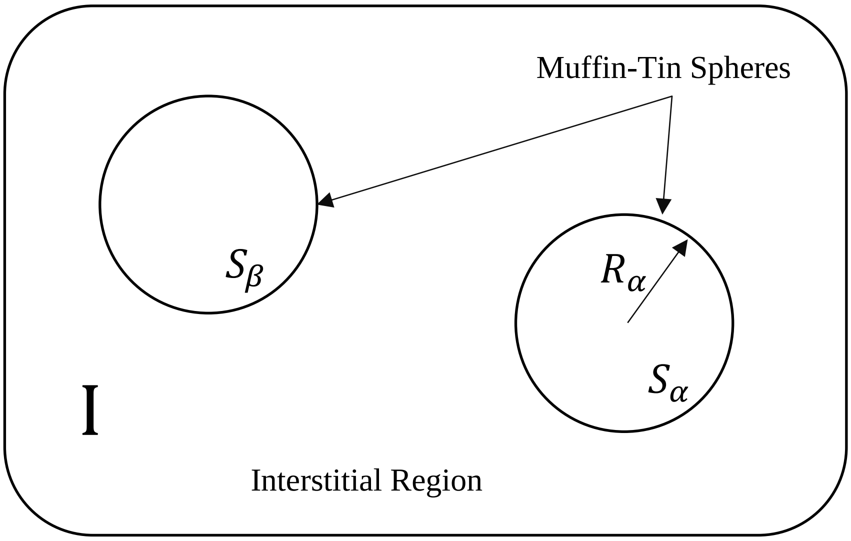

Figure II.5 Division of a unit cell into a Muffin-tin region and an interstitial region.

This combination of spherical symmetry and plane waves yielded a powerful tool for comprehending and analyzing the complex nature of crystalline structures. The wave function takes the following form:

$$\phi_{\vec{K}}^{\vec{k}}(\vec{r},E)=\begin{cases}\dfrac{1}{\sqrt{\Omega}}e^{i(\vec{k}+\vec{K})\cdot\vec{r}} & \vec{r}\in I\\ \displaystyle\sum_{\ell,m}A_{\ell m}^{\alpha,\vec{k}+\vec{K}}u_{\ell}^{\alpha}(r',E)Y_{m}^{\ell}(\hat{r}') & \vec{r}\in S_\alpha\end{cases} \tag{II.42}$$

Ω represents the volume of the primitive cell, and $r=r'-r_\alpha$, where r_α is the atomic position within the primitive cell. l is the index of angular momentum, and Y_m^ℓ denotes spherical harmonics. $\vec{k}$ is a wave vector in the reduced Brillouin zone, and $\vec{K}$ is a vector of the reciprocal lattice. u_ℓ^α are numerical solutions of the radial part of the Schrödinger equation for an energy E. The coefficients $A_{\ell m}^{\alpha,\vec{k}+\vec{K}}$ are chosen to satisfy boundary conditions. For a truly free atom, the boundary conditions that $u_\ell^\alpha=0$ must satisfy for $r\to\infty$ which puts constraint in the number of energy values E. However, in our case, these specific boundary conditions do not apply, allowing us to obtain numerical solutions for each energy E. The u_ℓ^α do not have physical reality; instead, they form a basis that differs from the eigenfunctions. Nonetheless, since this basis is still quite similar to the eigenfunctions in this region of the crystal, it remains highly effective. It is crucial to consider that the plane waves outside the Muffin tin spheres connect with the functions inside, ensuring continuity on the surface of the spheres. To achieve this, the plane waves are expressed in terms of spherical harmonics as follow **[44]**:

$$\frac{1}{\sqrt{\Omega}}e^{i(\vec{k}+\vec{K})\cdot\vec{r}} = \frac{4\pi}{\sqrt{\Omega}}e^{i(\vec{k}+\vec{K})\cdot\vec{r}_\alpha}\sum_{\ell,m} i^\ell j_\ell\left(|\vec{k}+\vec{K}||\vec{r}'|\right)Y_m^{\ell*}(\widehat{\vec{k}+\vec{K}})Y_m^\ell(\hat{r}') \qquad \text{(II.43)}$$

Where j_ℓ is the Bessel function of order ℓ and $\widehat{\vec{k}+\vec{K}}$ represents the angular dependence of the vector $\vec{k}+\vec{K}$. By identifying this equation in ℓ and m with **Equation II.42** and this in R_α which corresponds to the surface of the sphere muffin tin, we obtain:

$$A_{\ell m}^{\alpha,\vec{k}+\vec{K}} = \frac{4\pi i^\ell e^{i(\vec{k}+\vec{K})\cdot\vec{r}_\alpha}}{\sqrt{\Omega}u_\ell^\alpha(\vec{R}_\alpha, E)} j_\ell\left(|\vec{k}+\vec{K}|R_\alpha\right)Y_m^{\ell^*}(\vec{k}+\hat{K}) \qquad \text{(II.44)}$$

The parameters $A_{\ell m}^{\alpha,\vec{k}+\vec{K}}$ have unique definitions even when the energy E remains undetermined. **Equation II.43** contains a potentially infinite number of terms, which would necessitate an infinite number of $A_{\ell m}^{\alpha,\vec{k}+\vec{K}}$ coefficients. However, in practice, we introduce a cutoff at a specific value of ℓ known as $\ell_{\max}$. This introduces the challenge of determining the appropriate cutoff. This can be done using spherical harmonic nodes, which are points in space were the of amplitude of the spherical harmonic equal to zero. For a given $\ell_{\max}$, the corresponding spherical harmonic $Y_m^{\ell_{\max}}$ has a maximum of $2\ell_{\max}$ nodes per sphere α. We can express this value in length units as: $\frac{2\ell_{\max}}{(2\pi R_\alpha)} = \ell_{\max}/(\pi R_\alpha)$. For an equivalent plane wave, the number of nodes per unit length must be the same. A plane wave with a period equal to $\frac{2\pi}{K_{\max}}$ has $\frac{2\pi}{(2\pi/K_{\max})} = K_{\max}/\pi$ nodes per unit length. By ensuring that the cutoffs for plane waves ($K_{\max}$) and for angular functions ($\ell_{\max}$) have the same number of nodes per unit length. We get the following condition **[44]**:

$$R_\alpha K_{max} = \ell_{max} \qquad \text{(II.45)}$$

This methodology grants us the ability to determine an optimal value for $\ell_{\max}$ given a specific $K_{\max}$. With a finite $\ell_{\max}$, the matching at the sphere boundaries for each APW might not be perfectly precise, but it proves to be sufficiently accurate for practical purposes. Expanding $\ell_{\max}$ beyond what $R_\alpha K_{\max}$ dictates would only lead to undesirable instability near the sphere boundary. Consequently, it becomes apparent that there should not be a major difference in the radii of muffin tins for various atoms. If there were significant differences between them, finding a suitable $\ell_{\max}$ for each atom would become infeasible.

A single APW $\phi_{\vec{k}}^{\vec{k}}(\vec{r},E)$ can be viewed as an oscillating function that traverses the unit cell. When the electron interacts with an atom along its trajectory, its initial simple oscillatory motion undergoes a transition, leading to the development of a more complex pattern within the spherical region of the muffin tin that encompasses the specific atom.

Unfortunately, the augmented plane wave method presents some computational challenges. Among these challenges is that in order to accurately describe an eigenstate using APWs, E have to be set equal to the eigenvalue $\epsilon_{\vec{k}}^{n}$ of that particular state. Ironically, this eigenvalue is what we aim to determine in the first place. As a result, we are compelled to initiate the process by assuming a guessed value for $\epsilon_{\vec{k}}^{n}$ and considering it as E. This initial guess enables us to derive the APWs, determine the elements of the Hamiltonian matrix, establish the overlap matrix and solve the secular equation, and our initial guessed $\epsilon_{\vec{k}}^{n}$ should ideally be a solution to this equation. However, this is often not the case, necessitating us to start a second iteration of guesses to converge upon the appropriate solution. Which make the APW extremely slow. Another difficulty with this method is that related to u_{ℓ}^{α} function, which appears in the denominator of $A_{\ell m}^{\alpha,\vec{k}+\vec{K}}$ expression (**Equation II.44**). Indeed, there are in general values of the energy parameter, E for which u_{ℓ}^{α} vanishes on the sphere boundary, causing separation of radial functions with respect to plane wave functions. This is the so-called asymptote problem. Several modifications have been made to overcome these problems, including those proposed by Koelling **[45]** and by Andersen **[39]** known as linearized augmented plane waves (LAPW).

II.11.2 The LAPW method

The most challenging aspect of the APW method arises from the necessity to construct the functions $u_{\ell}^{\alpha}\left(\vec{R}_{\alpha},E\right)$ at an eigenenergy $E=\epsilon_{\vec{k}}^{n}$, which is unknown. It would be advantageous if we could obtain $u_{\ell}^{\alpha}\left(\vec{R}_{\alpha},\epsilon_{\vec{k}}^{n}\right)$ directly using quantities that are already known. This is precisely what is the goal of the Linearized Augmented Plane Wave (LAPW) method **[39,45]**. By calculating u_{ℓ}^{α} at a reference energy E_0, we can determine it at energies near to E_0 using Taylor expansion **[44]**.

$$u_{\ell}^{\alpha}\left(r',\epsilon_{\vec{k}}^{n}\right)=u_{\ell}^{\alpha}(r',E_0)+\left(E_0-\epsilon_{\vec{k}}^{n}\right)\dot{u}_{\ell}^{\alpha}(r',E_0)+O\left(E_0-\epsilon_{\vec{k}}^{n}\right)^2 \qquad \text{(II.46)}$$

Replacing the fixed energy value E_0 in APW by the first two expansion terms above, we arrived at the LAPW method. However, there is still the problem of determining the difference $\left(E_0 - \epsilon_{\vec{k}}^{n}\right)$ which is unknown, necessitating the introduction of a yet undetermined term denoted as $B_{\ell m}^{\alpha,\vec{k}+\vec{K}}$:

$$\phi_{\vec{K}}^{\vec{k}}(\vec{r}) = \begin{cases} \frac{1}{\sqrt{\Omega}} e^{i(\vec{k}+\vec{K})\cdot\vec{r}} & \vec{r} \in I \\ \sum_{\ell,m} \left(A_{\ell m}^{\alpha,\vec{k}+\vec{K}} u_{\ell}^{\alpha}(r', E_0) + B_{\ell m}^{\alpha,\vec{k}+\vec{K}} \dot{u}_{\ell}^{\alpha}(r', E_0)\right) Y_m^{\ell}(\hat{r}') & \vec{r} \in S_\alpha \end{cases} \tag{II.47}$$

To find $A_{\ell m}^{\alpha,\vec{k}+\vec{K}}$ and $B_{\ell m}^{\alpha,\vec{k}+\vec{K}}$, it is essential to ensure that the function within the muffin-tin sphere equal the plane wave in value and also in slope at the boundary of the sphere, leading to a system of two equations that enables the solution for both coefficients.

However, the definition of Linearized Augmented Plane Wave (LAPW) method is not completed. To illustrate this, consider describing an eigenstate $\psi_{\vec{k}}^{n}$ that strongly exhibits *p*-character for atom α (means $\ell = 1$). This implies that the expansion in the coefficients $A_{(\ell=\mathbf{1})m}^{\alpha,\vec{k}+\vec{k}}$ in the LAPW method is large. To enhance the efficiency of the calculation, it more useful to choose the energy parameter E_0 close to the *p*-band's center. By doing so, the $O\left(E_0 - \epsilon_{\vec{k}}^{n}\right)^2$ term in **Equation II.46** remains small, allowing for the linear term to be more accurate.

This approach can be applied for other states like *s*, *p*, *d*, and *f*, where ℓ ranging from 0 to 3, and for each atom in the system. Consequently, a universal E_0 should not be chosen; rather, a set of $E_{1,\ell}^{\alpha}$ values with ℓ ranging from 0 to 3 is more appropriate. Based on that, the definition of an LAPW method become:

$$\phi_{\vec{K}}^{\vec{k}}(\vec{r}) = \begin{cases} \frac{1}{\sqrt{\Omega}} e^{i(\vec{k}+\vec{K})\cdot\vec{r}} & \vec{r} \in I \\ \sum_{\ell,m} \left(A_{\ell m}^{\alpha,\vec{k}+\vec{K}} u_{\ell}^{\alpha}\left(r', E_{1,\ell}^{\alpha}\right) + B_{\ell m}^{\alpha,\vec{k}+\vec{K}'} \dot{u}_{\ell}^{\alpha}\left(r', E_{1,\ell}^{\alpha}\right)\right) Y_m^{\ell}(\hat{r}') & \vec{r} \in S_\alpha \end{cases} \tag{II.48}$$

Similar to various other methods for electronic band structure calculations, the efficiency of computations using LAPW basis relies on the count of utilized basis functions. In this method, the form of the electron density (or potential) on the surfaces of atomic spheres controls the number of basis functions. For A standard tightly packed material, each atom requires about 50 basis. As long as the atomic spheres exhibit the same behavior, the non-local property of the plane wave basis is flexible enough to describe the system. However, some atomic spheres might need more variational freedom, like for example a molecule adsorbed on a metal surface characterized by short interatomic distances. In such situation, the number of basis functions must be increased. This issue becomes more pronounced when the system under consideration has high interatomic distances in some regions while having short bonding distances in other regions. This scenario is often encountered when studying the chemical reactions on a surface. Where in this system, the use of sets of local bases (e.g., Gaussian type orbitals) appears to be more convincing.

Furthermore, the LAPW method is not suitable for treating semi-core states. The LAPW method aims to obtain accurate band energies near the linearization energies (E_l). For many materials, this condition can be met by choosing E_l values at the center of the bands **[46]**. However, in materials characterized by semi-core states, which lie intermediate between valence and core states, using a single E_l value may be insufficient. In such cases, the LAPW+LO method, established by Singh **[47]**, offers a better treatment of the problem compared to a resolution based solely on the LAPW method.

II.11.3 LAPW with Local Orbitals (LAPW+LO)

The incorporation of the LAPW method with local orbitals (LO) necessitates a modification of its fundamental orbitals. This modification aims to eliminate the requirement for multiple energy windows, achieved by introducing a third kind of basis functions. The fundamental idea behind this approach is to handle all bands within a single energy window. Singh **[47]** presented these orbitals as a linear combination of two radial functions associated with distinct energies, along with the derivative of one of these functions with respect to energy. We can write the local orbitals for specific atom α as follow:

$$\phi_{\alpha,LO}^{\ell m}(\vec{r}) = \begin{cases} 0 & \vec{r} \notin S_\alpha \\ \left(A_{\ell m}^{\alpha,LO} u_\ell^\alpha(r', E_{1,\ell}^\alpha) + B_{\ell m}^{\alpha,LO} \dot{u}_\ell^\alpha(r', E_{1,\ell}^\alpha) + C_{\ell m}^{\alpha,LO} u_\ell^\alpha(r', E_{2,\ell}^\alpha)\right) Y_m^\ell(\hat{r}') & \vec{r} \in S_\alpha \end{cases} \tag{II.49}$$

A local orbital is uniquely characterized by a specific combination of ℓ and m quantum numbers, as well as for a particular atom α. It earns its designation as a "local orbital" due to its absence in both the interstitial region as well as inside the muffin-tin spheres of neighboring atoms. Within the muffin tin sphere of atom α, The LAPW basis set uses the same radial functions $u_\ell^\alpha(r', E_{1,\ell}^\alpha)$ and $\dot{u}_\ell^\alpha(r', E_{1,\ell}^\alpha)$. The selection of the suitable linearization energy $E_{1,\ell}$ is made based on the higher of the two valence states. The lower valence state, resembling a free atom to a greater extent, is defined by a strongly concentrated energy $E_{2,\ell}^\alpha$. This energy can be adequately represented by a singular radial function, $u_\ell^\alpha(r', E_{2,\ell}^\alpha)$, corresponding to that specific energy level.

Local orbitals are distinct from plane waves in that they lack any $\vec{k}$ or $\vec{K}$ dependence in the interstitial region. Consequently, they serve as a localized representation of electron behavior within the muffin tin sphere. The three coefficients $A_{\ell m}^{\alpha,LO}$, $B_{\ell m}^{\alpha,LO}$ and $C_{\ell m}^{\alpha,LO}$ are determined by ensuring the normalization of the local orbital and imposing condition that they are null in value and slope at the muffin tin boundary, ensuring that the orbital remains confined within the muffin tin sphere and does not extend beyond it.

II.11.4 The APW+lo method

The problem with the APW approach was the energy dependency of its basis set. The LAPW+LO method, despite its somewhat greater basis size, successfully overcame this issue by incorporating an energy-independent basis set. in the following description of the APW+lo method **[48]**, we shall show that this new basis set maintains the same size as the APW technique while being energy independent. In essence, APW+lo uses the positive features of APW and LAPW+LO.

There are two different kinds of functions in the APW+lo basis set. The first category consists of APWs, which have a fixed set of energies $E_{1,\ell}^{\alpha}$:

$$\phi_{\vec{K}}^{\vec{k}}(\vec{r}) = \begin{cases} \dfrac{1}{\sqrt{\Omega}} e^{i(\vec{k}+\vec{K})\cdot\vec{r}} & \vec{r} \in I \\ \sum\limits_{\ell,m} A_{\ell m}^{\alpha,\vec{k}+\vec{K}} u_{\ell}^{\alpha}(r', E_{1,\ell}^{\alpha}) Y_{m}^{\ell}(\hat{r}') & \vec{r} \in S_{\alpha} \end{cases} \tag{II.50}$$

We know that the basis set with fixed energies does not adequately describe the eigenfunctions. To enhance its accuracy, we supplement the basis set with a different type of functions known as local orbitals (lo), we short them (lo) instead of (LO) to distinct them from those employed in the LAPW method. The definition of these local orbitals is as follows:

$$\phi_{\alpha,lo}^{\ell m}(\vec{r}) = \begin{cases} 0 & \vec{r} \notin S_{\alpha} \\ \left(A_{\ell m}^{\alpha,lo} u_{\ell}^{\alpha}(r', E_{1,\ell}^{\alpha}) + B_{\ell m}^{\alpha,lo} \dot{u}_{\ell}^{\alpha}(r', E_{1,\ell}^{\alpha})\right) Y_{m}^{\ell}(\hat{r}') & \vec{r} \in S_{\alpha} \end{cases} \tag{II.51}$$

We can use the same set of energies that we use in APW, although it’s not requirement. The determination of coefficients $A_{\ell m}^{\alpha,lo}$ and $B_{\ell m}^{\alpha,lo}$ involves normalization and the requirement that the local orbital maintains a zero value at the muffin tin boundary. Consequently, both the APW and the local orbital maintain continuity at the sphere boundary, but due absence of slope equality, their first derivatives display discontinuities.

During practical computations, a combined basis comprising LAPW and APW+LO can be utilized for distinct atoms, and even for various values of the quantum number l. Typically, orbitals exhibiting slower convergence with the count of plane waves (such as the 3d states of transition metals and the f states), or atoms with relatively smaller sphere sizes, are represented using the APW+LO basis. In contrast, the LAPW basis is employed for the remaining cases. This approach allows for a flexible and efficient treatment of various systems.

II.11.5 Concept of the FP-LAPW method

In the method of Full Potential Linearized Augmented Plane Waves (FP-LAPW) method, the LAPW basis given by **Equation II.48** and the APW+LO basis given by **Equation II.50** and **II.51** are implied and used according to the nature of the electronic states of the studied system. In this method, the form of the potential and the charge density are not approximated. Indeed, the potential describing the interactions between nuclei and electrons can be treated differently depending on whether one is inside or outside the muffin tin sphere. It’s developed through harmonics within each spherical atom in the muffin tin and is extended as a Fourier series within the interstitial regions. Hence, this method guarantees the potential's continuity at the muffin tin sphere's surface and presents its formulation in the following manner:

$$V(\vec{r}) = \begin{cases} \sum_{\vec{K}} V_I^{\vec{K}} e^{\vec{K}\vec{r}} & ,\vec{r} \in I \\ \sum_{\ell m} V_{MT}^{\ell m}(\vec{r}) Y_m^{\ell}(\hat{r}) & ,\vec{r} \in S_\alpha \end{cases} \tag{II.52}$$

Likewise, the charge density is formulated in the following manner:

$$\rho(\vec{r}) = \begin{cases} \sum_{\vec{K}} \rho_I^{\vec{K}} e^{\vec{K}\vec{r}} & ,\vec{r} \in I \\ \sum_{\ell m} \rho_{MT}^{\ell m}(\vec{r}) Y_m^{\ell}(\hat{r}) & ,\vec{r} \in S_\alpha \end{cases} \tag{II.53}$$

The WIEN2k code incorporates the FP-L/APW+lo method through set of programs. In the next section, we give a brief overview of this code.

II.11.6 The WIEN2k Code

The FP-LAPW method has been implemented in the WIEN code, a set of programs developed by Blaha, Schwarz, and their colleagues **[10,49]**. This code has been successfully used for treating high-temperature superconducting systems **[50]**, minerals **[51]**, transition metal surfaces **[52]**, non-ferromagnetic oxides **[53]**, molecules, as well as electric field gradients **[55]**.

WIEN2k is a collection of several Fortran90 programs that are linked together via C-shell scripts. The entire calculation process can be divided into two parts:

1- Initialization (preparation of the input files)

2- Self-consistent cycle (SCF)

a. Initialization

To initiate a computation with WIEN2k, it is necessary to generate a case.struct file. Within this file, crucial crystal attributes such as structure type, lattice constants, atomic positions, and the radii of muffin-tin spheres (R_{MT}) are specified. These operations are performed through a series of programs that generate:

NN: A subprogram for verifying distances between nearest neighbors and equivalent positions in order to avoid spheres overlapping.

LSTART: Generates atomic densities and establishes the treatment of distinct atomic orbitals within the band structure calculation.

SYMMETRY: Generates spatial symmetry operations and determines the point group of individual atomic sites.

KGEN: Generates the number of k-points in the Brillouin zone.

DSART: Generates a starting density for the self-consistent cycle (SCF) by superimposing the atomic densities generated in LSTART.

b. Self-consistent cycle

Based on a convergence criterion (energy, force, charge density), The energies and electronic density of the ground state are calculated at this stage. The subprograms used are:

LAPW0: Generates the Poisson potential for density calculation.

LAPW1: Computes valence bands, eigenvalues, and eigenvectors.

LAPW2: Calculates valence densities for the eigenvectors.

LCORE: Computes core states and densities.

MIXER: Performs mixing of input and output densities (starting, valence, and core).

Once the self-consistent calculation is completed, the properties of the ground state (charge density, band structure, optical properties, etc.) are determined. **Figure II.6** represents the work flow of WIEN2k software **[49]**.

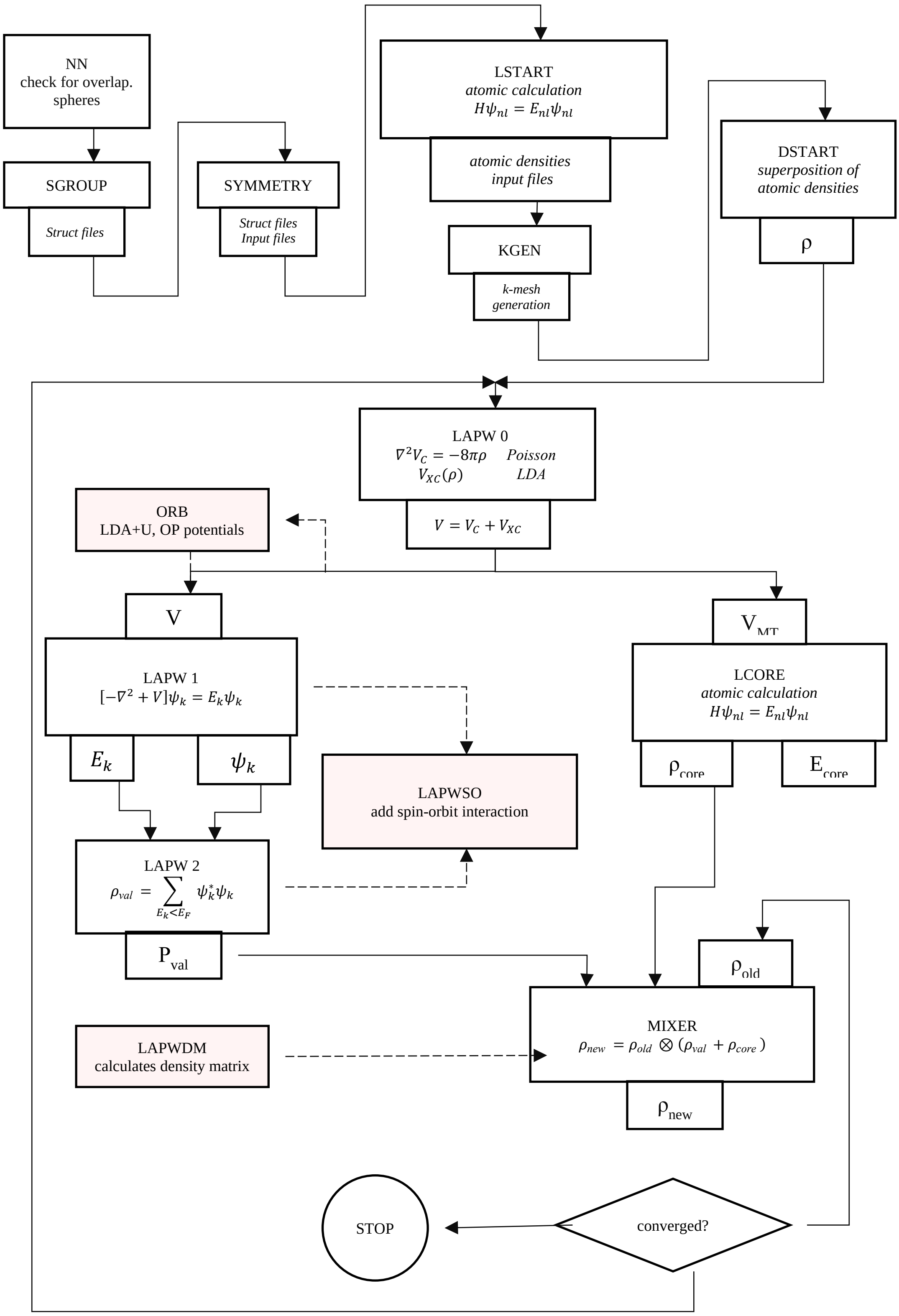

Figure II.6 Program flow in WIEN2k [49].

II.12 Conclusion

This chapter provides an overview of the formalism of Density Functional Theory (DFT) and the methodologies employed in our research. We have meticulously described the DFT theory and introduced the FP-LAPW method, which forms the basis for our calculations of the physical properties of the materials under investigation. Furthermore, we briefly introduced the Wien2k computer code utilized in this thesis, along with its algorithms and essential programs crucial for determining the various properties targeted in our study.

In the forthcoming chapter, we will delve into a detailed discussion of the different choices and convergence criteria employed in this research. Lastly, in the latter part of this chapter, we provided a concise presentation of the calculation results of the different binary compounds and ternary alloys.

II.13 References

[1] E Schrödinger, **Phys. Rev.** 28 (6), 1049 (1926).
[2] PAM Dirac, **Proc. R. soc. Lond. Ser. A-Contain. Pap. Math. Phys. Character** 112 (762), 661 (1926).
[3] M Born, **Z. Phys.** 37 (12), 863 (1926).
[4] M Born and W Heisenberg, in *Original Scientific Papers Wissenschaftliche Originalarbeiten*, edited by Walter Blum, Helmut Rechenberg, and Hans-Peter Dürr (Springer Berlin Heidelberg, Berlin, Heidelberg, 1985), pp. 216.
[5] L De Broglie, *An Introduction to the Study of Wave Mechanics*. (Methuen & Co., 1930).
[6] Dimensions, research database, published by Digital Science.
[7] P Hohenberg and W Kohn, **Phys. Rev.** 136 (3B), B864 (1964).
[8] W Kohn, **Rev. Mod. Phys.** 71 (5), 1253 (1999).
[9] W Kohn and LJ Sham, **Phys. Rev.** 140 (4A), A1133 (1965).
[10] P Blaha et al., **J. Chem. Phys.** 152 (7) (2020).
[11] M Born and R Oppenheimer, **Ann Phys** 389 (20), 457 (1927).
[12] DR Hartree, **Math. Proc. Camb. Philos. Soc.** 24 (1), 89 (1928).
[13] W Pauli, **Z. Phys.** 31 (1), 765 (1925).
[14] V Fock, **Z. Phys.** 61 (1), 126 (1930).
[15] JC Slater, **Phys. Rev.** 34 (10), 1293 (1929).
[16] LH Thomas, **Math. Proc. Camb. Philos. Soc.** 23 (5), 542 (1927).
[17] E Fermi, **Z. Phys.** 48 (1), 73 (1928).
[18] PAM Dirac, **Math. Proc. Camb. Philos. Soc.** 26 (3), 376 (1930).
[19] E Wigner, **Phys. Rev.** 46 (11), 1002 (1934).
[20] DM Ceperley and BJ Alder, **Phys. Rev. Lett.** 45 (7), 566 (1980).
[21] SH Vosko et al., **Can. J. Phys.** 58 (8), 1200 (1980).
[22] JP Perdew and A Zunger, **Phys. Rev. B** 23 (10), 5048 (1981).
[23] BY Tong, **Phys. Rev. B** 6 (4), 1189 (1972).
[24] O Gunnarsson et al., **Phys. Rev. B** 10 (4), 1319 (1974).
[25] JP Perdew et al., **Phys. Rev. B** 46 (11), 6671 (1992).
[26] Z Wu and RE Cohen, **Phys. Rev. B** 73 (23), 235116 (2006).
[27] JP Perdew et al., **Phys. Rev. B** 48 (7), 4978 (1993).
[28] AD Becke, **Phys. Rev. A** 38 (6), 3098 (1988).
[29] JP Perdew and Y Wang, **Phys. Rev. B** 45 (23), 13244 (1992).
[30] JP Perdew et al., **Phys. Rev. Lett.** 77 (18), 3865 (1996).
[31] AD Becke and ER Johnson, **J. Chem. Phys.** 124 (22) (2006).
[32] F Tran and P Blaha, **Phys. Rev. Lett.** 102 (22), 226401 (2009).
[33] AD Becke and MR Roussel, **Phys. Rev. A** 39 (8), 3761 (1989).
[34] C Frayret, Université Sciences et Technologies - Bordeaux I, 2004.
[35] F Bloch, **Z. Phys.** 52 (7), 555 (1929).
[36] JC Slater, *Quantum Theory of Molecules and Solids. vol. 2,. Symmetry and energy bands in crystals*. (McGraw-Hill New York, NY, New York, NY, 1965).
[37] C Herring, **Phys. Rev.** 57 (12), 1169 (1940).
[38] JC Slater, **Phys. Rev.** 51 (10), 846 (1937).
[39] OK Andersen, **Phys. Rev. B** 12 (8), 3060 (1975).
[40] N Troullier and JL Martins, **Phys. Rev. B** 43 (3), 1993 (1991).
[41] G Kresse et al., **J. Phys.: Condens. Matter** 4 (36), 7451 (1992).
[42] OH Nielsen and RM Martin, **Phys. Rev. Lett.** 50 (9), 697 (1983).
[43] WC Topp and JJ Hopfield, **Phys. Rev. B** 7 (4), 1295 (1973).

[44] S Cottenier, *Density Functional Theory and the Family of (L) APW-Methods: A Step-by-Step Introduction*. (2004).
[45] DD Koelling and GO Arbman, **J Phys F Met Phys** 5 (11), 2041 (1975).
[46] DJ Singh, *Planewaves, Pseudopotentials and the LAPW Method*. (Springer US, 2013).
[47] D Singh, **Phys. Rev. B** 43 (8), 6388 (1991).
[48] E Sjöstedt et al., **Solid State Commun.** 114 (1), 15 (2000).
[49] P Blaha et al., **Improved and updated Unix version of the original copyright WIEN code** (1997).
[50] K Schwarz et al., **Phys. Rev. B** 42 (4), 2051 (1990).
[51] B Winkler et al., **Am. Mineral.** 81 (5-6), 545 (1996).
[52] B Kohler et al., **Phys. Rev. Lett.** 74 (8), 1387 (1995).
[53] XG Wang et al., **Phys. Rev. Lett.** 81 (5), 1038 (1998).

Chapter III Results and discussion of Zinc-based semiconductor alloys

III.1 Introduction

The development of II-VI semiconductor materials has witnessed significant advancements in recent years. This chapter focuses on exploring the properties and applications of these materials, specifically ZnO, ZnS, ZnSe, and ZnTe, as well as their ternary alloys. These materials have demonstrated to be of great technological value, finding use in a variety of systems and technologies, including photonic, electronic, and optoelectronic devices, light-emitting diodes, optical communication systems, performance sensors and solar cells. Using these binary compounds, we can form an infinite series of ternary ($ZnO_{1-x}S_x$, $ZnO_{1-x}Se_x$, $ZnO_{1-x}Te_x$, …) alloys. It is enough to vary the composition of these alloys.

This chapter presents a theoretical research based on density functional theory (DFT) using the full potential linearized augmented plane wave (FP-LAPW) approach as implemented in the Wien2K code to better understand the physical characteristics of these materials. Various alternative theoretical models have also been presented for interpreting experimental results and predicting new materials are discussed.

The structural, electronic and optical properties of solids are essential in the development of new devices. While considerable knowledge exists regarding the physical properties of binary compounds in the zinc-blende structure, there is a lack of data available for the wurtzite binary and ternary compounds. Therefore, this study aims to fill this gap by describing the physical properties of these alloys using density functional theory (DFT).

By employing different approximations, the chapter aims to examine the structural, electronic, optical and elastic properties of binary and ternary compounds. The obtained results are compared with experimental data and other existing theoretical models found in the literature. The results showed a direct correlation between the physical properties and electronic properties of these materials, with a close connection to their structural properties.

III.2 Details of calculation method

In this work, the calculations are carried out using the full potential linearized augmented plane wave (FP-LAPW) within the framework of density functional theory as implemented in Wien2k code **[1-3]**. For structural properties, the exchange-correlation potential was treated using Local Density approximation (LDA) **[4]**, Perdew-Burke-Ernzerhof's generalized gradient approximation (PBE-GGA) **[5]** and Wu and Cohen's generalized gradient approximation (WC-GGA) **[6]**. It's well known that those approximations underestimate the value of the band gap, so we have used the modified Becke-Johnson potential of Tran-Plaha (TB-mBJ) parameterized by Koller et al **[7]**, as it has been proven that this approximation is more accurate in calculating the bandgap and hence the optical and electronic properties of the solid materials. For comparison, we have also used Perdew-Burke-Ernzerhof's generalized gradient approximation (PBE-GGA) to calculate the electronic and optical properties. In the FP-LAPW method, the wave function is expanded into spherical harmonic waves inside non-overlapping muffin tin spheres. In the remaining space (interstitial region), the wave function developed into a plane wave basis set. The energy convergence criteria are chosen to be 0.0001 Ry. The electron wave functions were expanded inside the muffin-tin spheres on spherical harmonic functions with a cut-off of l_{max} = 10. Whereas, in the interstitial region, they are expanded on plane wave basis set with an energy cut-off parameter of the matrix size $R_{mt} \times K_{max}$ = 7. The radius of the muffin tin spheres was selected as 1.81, 1.63, 1.69, 1.72, and 1.85 atomic units (a.u) for 'Zn', 'O', 'S', 'Se' and 'Te' respectively **[8-9]**. A mesh of 100 special *k*-points and 500 special *k*-points is used to respectively calculate the structural and optoelectronic properties. The present calculations are based on the Wurtzite (B4) structure, which has hexagonal primitive unit cell with space group $P6_3mc$. The binary compound ZnO has two atoms: Zn at (1/3, 2/3, 0) and O at (1/3, 2/3, *u*). In order to make alloying possible, we considered a supercell of 2×2×1. Then we substituted the oxygen 'O' atoms by 'Y' atoms in the $ZnO_{1-x}Y_x$ ternary alloy, where Y= 'S', 'Se' and 'Te'. We can get series of alloys just by varying the *x* composition from 0 to 1 by step of 0.25, where **Table III.1** shows the atomic positions for each material. The electronic configurations of the elements are illustrated as follows: Zn: [Ar] $3d^{10}$ $4s^2$, O: [He] $2s^2$ $2p^4$, S: [Ne] $3s^2$ $3p^4$. Se: [3d10] $4s^2$ $4p^4$ and Te: [Kr] $4d^{10}$ $5s^2$ $5p^4$.

Table III.1 Atomic positions of the $ZnO_{1-x}Y_x$ (Y= S, Se, Te) alloys in the wurtzite structure.

x	Atoms	Atomic positions
0.25	**Zn**	(1/6,1/3,0), (1/3,1/6,1/2), (2/3,1/3,0), (1/3,2/3,1/2), (1/6,5/6,0), (5/6,1/6,1/2), (2/3,5/6,0), (5/6,2/3,1/2)
	O	(2/3,1/3,*u*), (1/3,2/3,*u*+1/2), (1/6,5/6,*u*), (5/6,1/6,*u*+1/2), (2/3,5/6,*u*), (5/6,2/3,*u*+1/2)
	Y (S, Se, Te)	(1/6,1/3,*u*), (1/3,1/6,*u*+1/2)
0.5	**Zn**	(1/6,1/3,0), (1/3,1/6,1/2), (2/3,1/3,0), (1/3,2/3,1/2), (1/6,5/6,0), (5/6,1/6,1/2), (2/3,5/6,0), (5/6,2/3,1/2)
	O	(1/6,5/6,*u*), (5/6,1/6,*u*+1/2), (2/3,5/6,*u*), (5/6,2/3,*u*+1/2)
	Y (S, Se, Te)	(1/6,1/3,*u*), (1/3,1/6,*u*+1/2), (2/3,1/3,*u*), (1/3,2/3,*u*+1/2)
0.75	**Zn**	(1/6,1/3,0), (1/3,1/6,1/2), (2/3,1/3,0), (1/3,2/3,1/2), (1/6,5/6,0), (5/6,1/6,1/2), (2/3,5/6,0), (5/6,2/3,1/2)
	O	(2/3,5/6,*u*), (5/6,2/3,*u*+1/2)
	Y (S, Se, Te)	(1/6,1/3,*u*), (1/3,1/6,*u*+1/2), (2/3,1/3,*u*), (1/3,2/3,*u*+1/2), (1/6,5/6,*u*), (5/6,1/6,*u*+1/2)

III.3 Structural properties

The initial step of ab-initio calculations involves determining the optimized geometry of the crystal structure, which is crucial for examining the fundamental properties of materials in their ground state. The lattice equilibrium parameters of a crystal structure represent the parameters that minimize the overall energy. Achieving convergence in each self-consistent cycle is necessary to minimize the energy as a function of volume. To ensure convergence, the iteration process is repeated until the calculated energy of the system reaches a value lower than 10^{-3} *Ryd*. The wurtzite structure can be described by three parameters *a*, *c* and *u* (internal parameter). All these parameters have been calculated for the lowest energy of the crystal. The lattice constants, bulk modulus B_0 and its first pressure derivative *B'* have been optimized by fitting the obtained total energy as a function of volume to Birch-Murnaghan's equation of state **[10-11]**:

$$E(V) = E(V_0) + \frac{9V_0B_0}{16}\left\{\left[\left(\frac{V_0}{V}\right)^{2/3} - 1\right]^3 B_0' + \left[\left(\frac{V_0}{V}\right)^{2/3} - 1\right]^2 \left[6 - 4\left(\frac{V_0}{V}\right)^{2/3}\right]\right\} \quad \text{(III.1)}$$

Where E_0, V_0, B_0 and B_0' are respectively: the total energy, the equilibrium volume, the compressibility modulus and its derivative. The compressibility modulus is given by:

$$B_0 = V_0 \frac{\partial^2 E}{\partial V^2}\bigg|_{V=V_0} \tag{III.2}$$

The compressibility modulus B_0 measures the stiffness of the crystal, indicating that a higher B_0 value corresponds to greater rigidity of the crystal structure. To determine the equilibrium geometry of the wurtzite phase, we optimize the independent parameters *V* (volume of the unit cell), *c/a* ratio and the internal parameter *u* as follows: In the first step, we assume the ideal wurtzite structure and determine the equilibrium volume by varying the lattice constants *a* and *c*. Then, keeping the equilibrium volume fixed, the *c/a* ratio is varied to find the optimum value. At new *c/a* ratio we once again vary the lattice constants *a*, *c* to determine the new equilibrium volume. Then, having found *c/a* and *V*, we determine the equilibrium internal parameter *u* by doing structural relaxation and taking the value that minimize the total energy.

III.3.1 Binary compounds

The curves giving the variation of total energy as a function of volume for the different binary compounds ZnO, ZnS, ZnSe and ZnTe, are shown in **Figures III.1(a-d)**. The solid line represents the best fit of the points $E_{tot}(V)$ with the Birch-Murnaghan equation of state (**Equation (III.1)**). The numerical results obtained for the lattice parameters and the compressibility modulus calculated by the methods LDA, PBE-GGA and WC-GGA, are reported in **Table III.2**.

By comparing our optimized values with those available in the literature, we can see that they agree well with the theoretical results. However, compared to the experimental results, we encounter the well-known behavior of the PBE-GGA approximation which overestimates the lattice constants compared to those found experimentally, and on the other hand the LDA approximation underestimates the lattice constants compared to those found experimentally. With regard to bulk modulus, we observe an inverse behavior to the lattice parameters. Although it’s not always the case, but in general, its overestimated by LDA and underestimated by PBE-GGA. The approximation WC-GGA gives exact average values of two other approaches PBE-GGA and LDA. Overall, we can say that the WC-GGA approximation gave us results agreeing well with the experimental measurements and the theoretical results obtained by other works using different DFT approximations

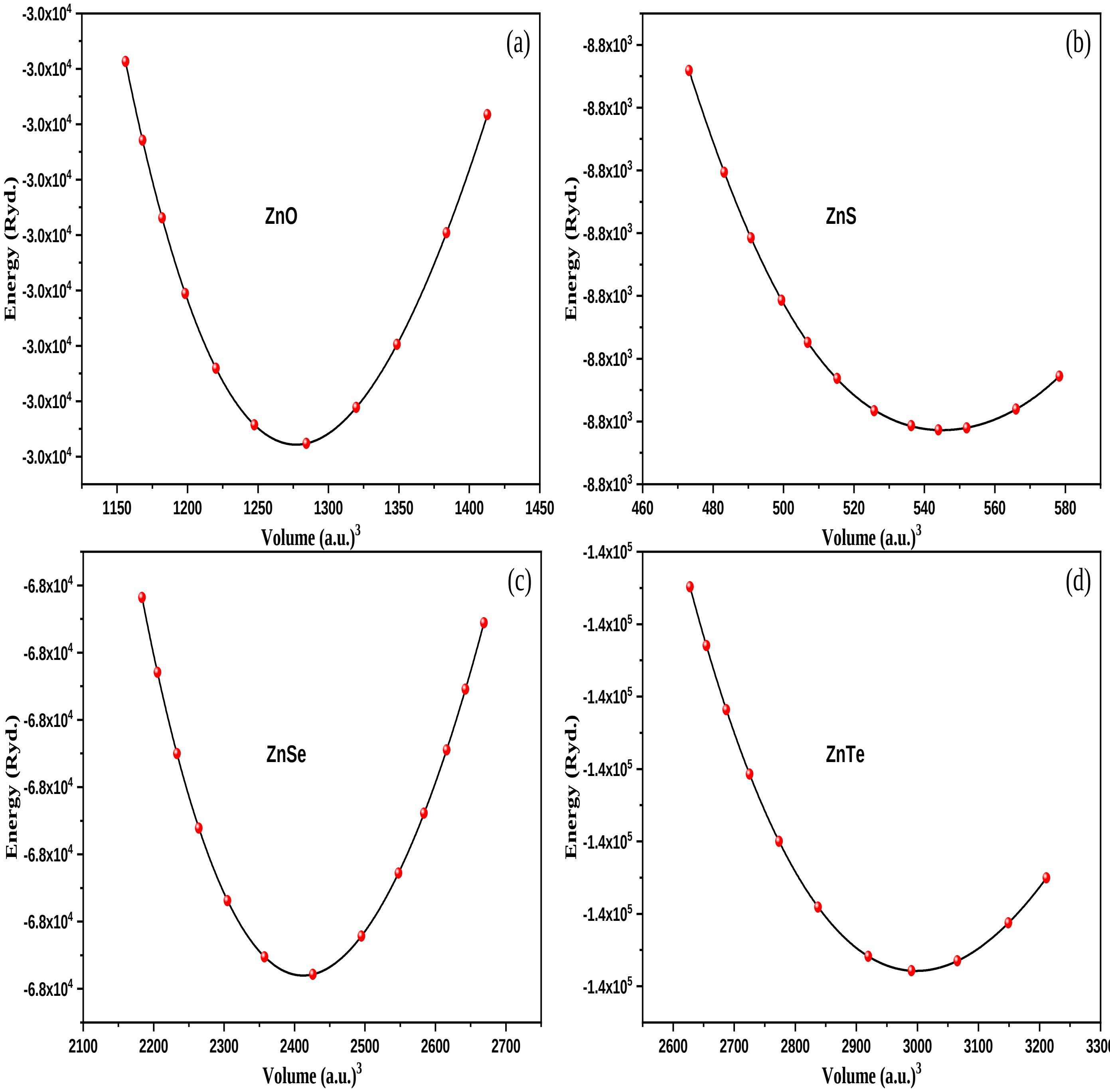

Figure III.1 Change in the total energy as a function of the volume for binary compounds ZnO, ZnS, ZnSe and ZnTe.

Table III.2 Structural parameters of binary compounds ZnO, ZnS, ZnSe and ZnTe.

Compound	Parameters	Present work			Experimental	Theoretical
		LDA	PBE-GGA	WC-GGA		
ZnO	***a(Å)***	3.186	3.410	3.242[a, b]	3.249[c], 3.249[d]	3.29[f], 3.286[g], 3.17[h]
	c(Å)	5.184	5.531	5.197[a, b]	5.206[c], 5.204[d]	5.269[f], 5.269[g], 5.12[h]
	c/a	1.63	1.62	1.601[a, b]	1.601[d]	1.602[f], 1.603[g]
	u	0.3769	0.3777	0.3807[a, b]	0.382[e]	0.38089[f], 0.38[g]
	B(GPa)	166.830	132.394	146.124[a, b]	183[d], 181[e]	128.72[g]
	B'	4.807	4.294	4.679[a, b]	4.0[d], 4.0[e]	4.38[g]
ZnS	***a(Å)***	3.742	3.846	3.846	3.8226[h], 3.816[i]	3.775[k], 3.74[l]
	c(Å)	6.135	6.303	6.303	6.2605[h], 6.252[i]	6.167[k], 6.12[l]
	c/a	1.64	1.64	1.64	1.638[h], 1.6[i]	1.6424[k]
	u	0.3720	0.3724	0.3721	0.374[i], 0.3748[j]	0.3742[k]
	B(GPa)	87.160	69.140	68.805	80[i]	84.99[k]
	B'	4.6	4.438	4.685	4[i]	4.67[k]
ZnSe	***a(Å)***	3.925	4.042	3.995[a]	3.996[m]	3.93[k], 4.043[n]
	c(Å)	6.456	6.635	6.465[a]	6.626[m]	6.464[k], 6.703[n]
	c/a	1.64	1.65	1.618[a]	1.66[m]	1.64[k]
	u	0.3692	0.3697	0.3741[a]	0.375[m]	0,3740[k], 0.371[n]
	B(GPa)	70.734	59.264	65.802[a]	-	70.78[k]
	B'	3.906	3.880	3.415[a]	-	4.73[k]
ZnTe	***a(Å)***	4.229	4.348	4.295[b]	4.270[m], 4.27[o]	4.234[p], 4.35[q]
	c(Å)	6.941	7.127	6.952[b]	6.99[m, o]	6.977[p], 7.14[q]
	c/a	1.64	1.64	1.619[b]	1.637[m]	1.648[p]
	u	0.3727	0.3762	0.3766[b]	-	-
	B(GPa)	59.416	54.579	55.307[b]	-	55.3[p]
	B'	3.160	1.623	3.661[b]	-	-

[a][8], **[b][9]**, **[c][12]**, **[d][13]**, **[e][14]**, **[f][15]**, **[g][16]**, **[h][17]**, **[i][18]**, **[j][19]**, **[k][20]**, **[l][21]**, **[m][22]**, **[n][23]**,**[o][24]**, **[p][25]**, **[q][26]**.

III.3.2 Ternary alloys

The procedure used to determine the structural parameters of ternary alloys follows a similar approach to that used for binary compounds. It involves determining the total energy computed for various volumes surrounding the equilibrium volume for x = 0.25, 0.5, and 0.75. These values are then adjusted to equilibrium values *E(V)* using the Birch-Murnaghan equation. **Figures III.2(a-c)**, **Figures III.3(a-c)** and **Figures III.4(a-c)** illustrate the variation of total energy with respect to volume for the ternary alloys $ZnO_{1-x}S_x$, $ZnO_{1-x}Se_x$, and $ZnO_{1-x}Te_x$, respectively at different compositions.

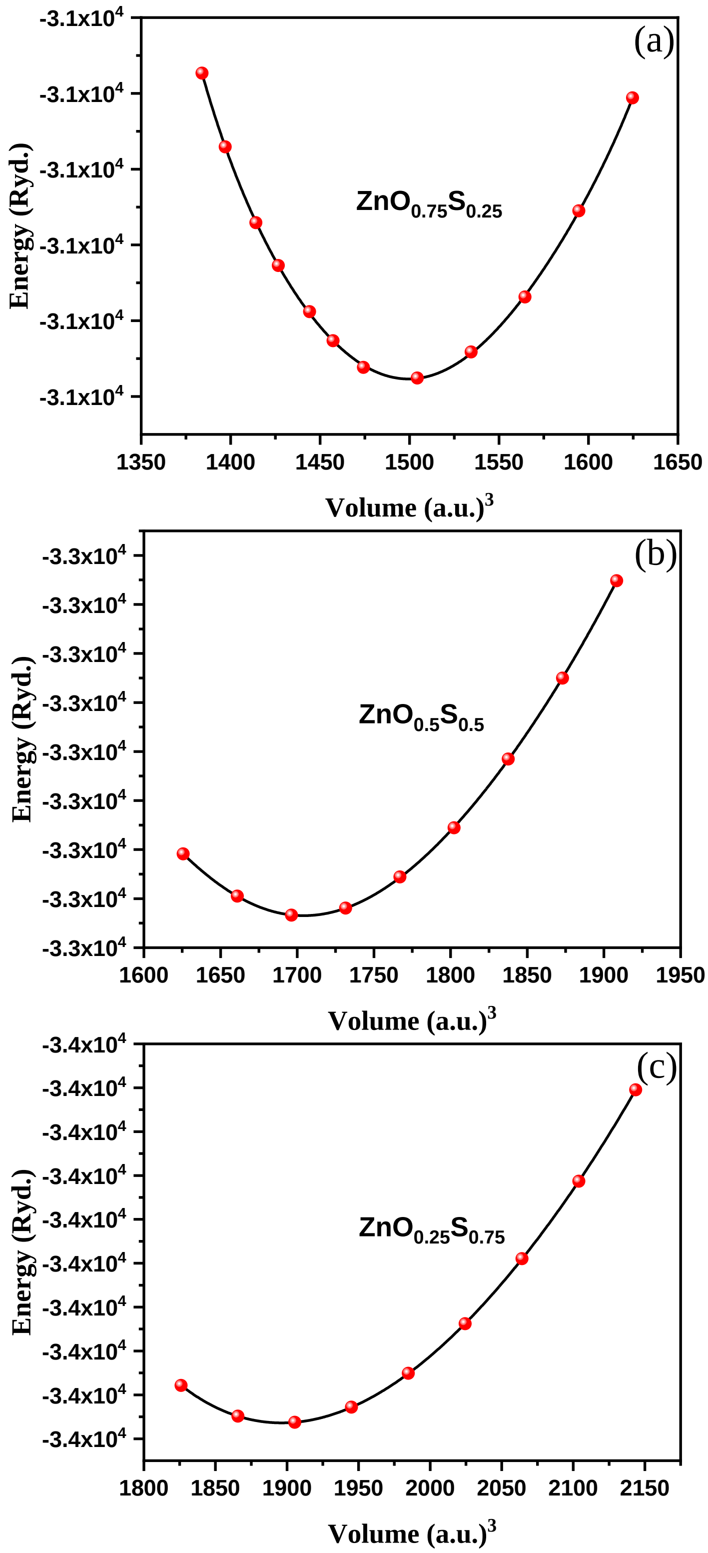

Figure III.2 Change in the total energy as a function of volume for $ZnO_{1-x}S_x$ ternary alloys.

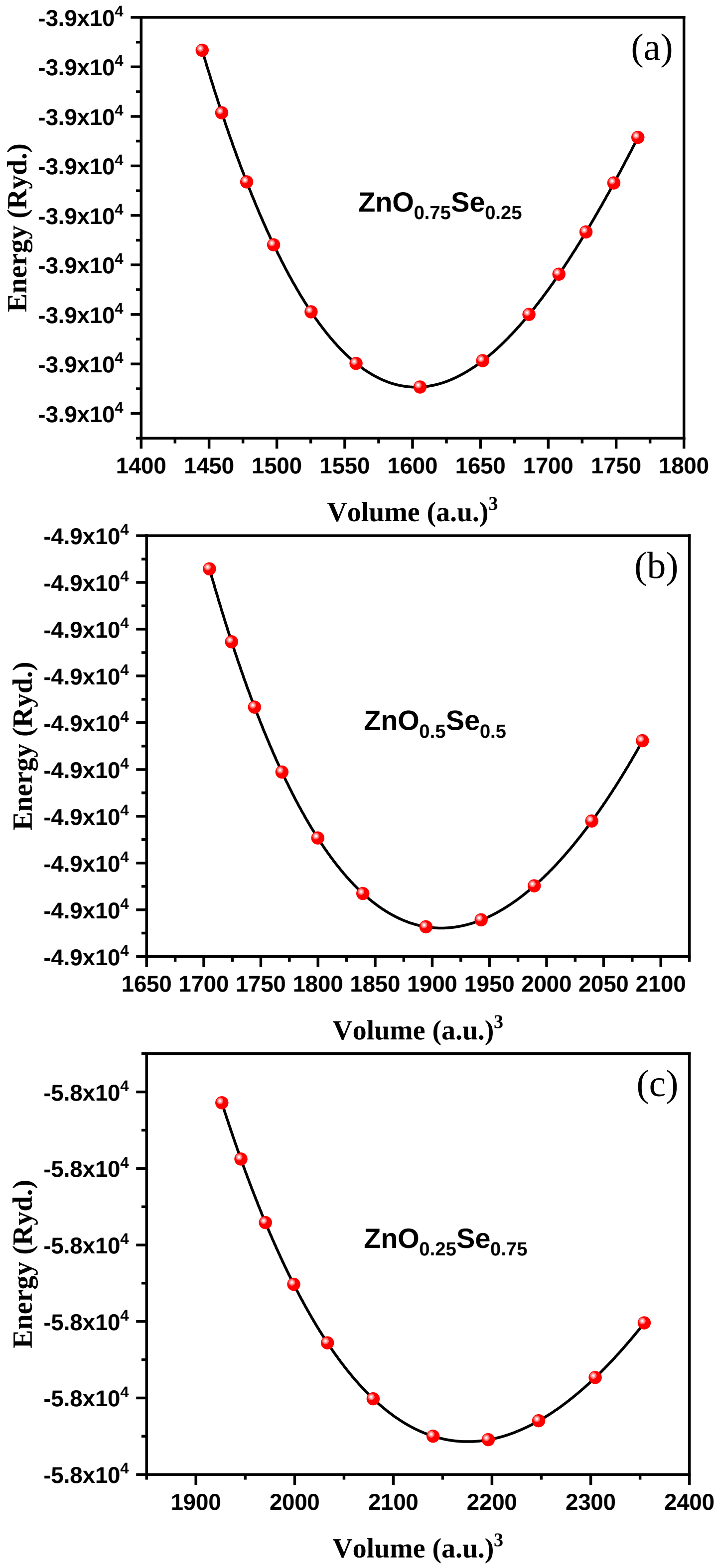

Figure III.3 Change in the total energy as a function of volume for $ZnO_{1-x}Se_x$ ternary alloys.

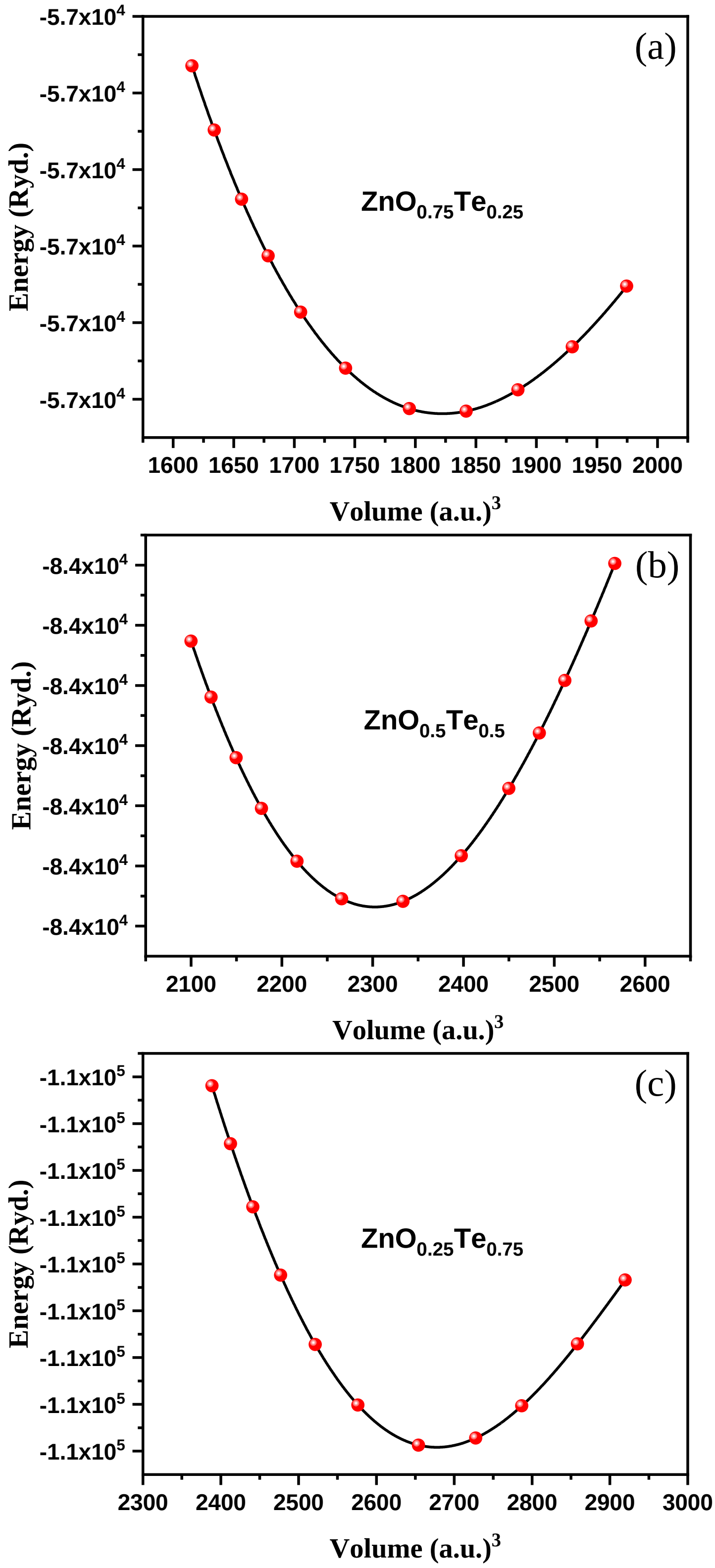

Figure III.4 Change in the total energy as a function of volume for $ZnO_{1-x}Te_x$ ternary alloys.

The values of structural parameters at equilibrium for all the studied ternary alloys, have been presented in **Tables III.3-5**. The parameters included in this study consist of the lattice parameters *a* and *c*, the internal parameter *u*, the compressibility modulus B_0, and its first pressure derivative *B'*. The findings obtained from our study are then compared to other research documented in the existing literature. Like binary compounds, we notice the same behavior of LDA and PBE-GGA approximations, where the first one underestimates the lattice constants and the second one overestimates them, and WC-GGA is the average between the two approximations. Also, for all ternary alloys, we notice that the lattice constants increase with increase of the composition *x*, the opposite thing happen in the case of bulk modulus. For ternary alloys $ZnO_{1-x}S_x$ and $ZnO_{1-x}Se_x$, the values of the structural parameters obtained in the present work are in good agreement with the data available in the literature. In the case of the wurtzite ternary alloy $ZnO_{1-x}Te_x$ there are no other theoretical or experimental data that we aware of to compare with our results.

Table III.3 Structural parameters of $ZnO_{1-x}S_x$ ternary alloys.

Alloy	***x***	**Parameters**	**Present work**			**Exp.**	**Theo.**
			LDA	**PBE-GGA**	**WC-GGA**		
$ZnO_{1-x}S_x$	**0.25**	***a(Å)***	3.365	3.470	3.411	-	3.46[a], 3.30[b]
		c(Å)	5.430	5.611	5.508	-	5.58[a], 5.35[b]
		c/a	1.61	1.62	1.61	-	-
		u	0.3790	0.3785	0.3788	-	-
		B(GPa)	129.676	103.238	117.618	-	129.7[a]
		B'	4.220	4.308	4.286	-	-
	0.5	***a(Å)***	3.513	3.609	3.556	-	3.61[a], 3.53[b]
		c(Å)	5.690	5.852	5.758	-	5.80[a], 5.75[b]
		c/a	1.62	1.62	1.62	-	-
		u	0.3769	0.3766	0.3769	-	-
		B(GPa)	108.589	90.447	99.065	-	82.1[a]
		B'	5.766	3.830	4.502	-	-
	0.75	***a(Å)***	3.645	3.745	3.688	-	3.74[a], 3.74[b]
		c(Å)	5.896	6.063	5.965	-	6.07[a], 6.11[b]
		c/a	1.62	1.62	1.62	-	-
		u	0.3770	0.3769	0.3771	-	-
		B(GPa)	94.464	78.142	87.030	-	66.1[a]
		B'	4.767	3.929	4.550	-	-

[a]**[27]**, [b]**[28]**.

Table III.4 Structural parameters of $ZnO_{1-x}Se_x$ ternary alloys.

Alloy	x	Parameters	Present work			Exp.	Theo.
			LDA	PBE-GGA	WC-GGA		
$ZnO_{1-x}Se_x$	0.25	*a(Å)*	3.435	3.532	3.488[a]	-	3.34[b]
		c(Å)	5.595	5.756	5.635[a]	-	5.42[b]
		c/a	1.63	1.63	1.615[a]	-	-
		u	0.3766	0.3787	0.3786[a]	-	-
		B(GPa)	117.100	89.829	105.582[a]	-	-
		B'	3.962	5.339	4.542[a]	-	-
	0.5	*a(Å)*	3.631	3.761	3.689[a]	-	3.53[b]
		c(Å)	5.958	6.170	5.995[a]	-	5.75[b]
		c/a	1.64	1.64	1.625[a]	-	-
		u	0.3736	0.3737	0.3760[a]	-	-
		B(GPa)	90.656	71.814	85.068[a]	-	-
		B'	2.591	5.056	4.614[a]	-	-
	0.75	*a(Å)*	3.802	4.001	3.860[a]	-	3.74[b]
		c(Å)	6.214	6.552	6.246[a]	-	6.11[b]
		c/a	1.63	1.64	1.618[a]	-	-
		u	0.3746	0.3740	0.3770[a]	-	-
		B(GPa)	85.281	61.640	71.900[a]	-	-
		B'	5.472	4.835	4.751[a]	-	-

[a][8], [b][28].

Table III.5 Structural parameters of $ZnO_{1-x}Te_x$ ternary alloys.

Alloy	x	Parameters	Present work			Exp.	Theo.
			LDA	PBE-GGA	WC-GGA		
$ZnO_{1-x}Te_x$	0.25	*a(Å)*	3.588	3.692	3.632[a]	-	-
		c(Å)	5.830	6.004	5.912[a]	-	-
		c/a	1.62	1.63	1.628[a]	-	-
		u	0.3773	0.3770	0.3769[a]	-	-
		B(GPa)	99.616	77.524	89.745[a]	-	-
		B'	4.725	4.464	4.581[a]	-	-
	0.5	*a(Å)*	3.926	3.987	3.921[a]	-	-
		c(Å)	6.423	6.507	6.402[a]	-	-
		c/a	1.64	1.63	1.633[a]	-	-
		u	0.3743	0.3749	0.3748[a]	-	-
		B(GPa)	73.175	54.880	64.081[a]	-	-
		B'	5.270	5.080	3.511[a]	-	-
	0.75	*a(Å)*	4.090	4.210	4.138[a]	-	-
		c(Å)	6.620	6.826	6.701[a]	-	-
		c/a	1.62	1.62	1.620[a]	-	-
		u	0.3769	0.3765	0.3766[a]	-	-
		B(GPa)	60.761	42.499	56.945[a]	-	-
		B'	0.527	7.139	4.377[a]	-	-

[a][9].

Concerning the variation of lattice parameters with change of composition *x*, Vegard's law **[29]** indicates that those parameters for wurtzite ternary alloys can be explained in terms of their binary components using the following equations:

$$a(AB_{1-x}C_x) = xa_{AC} + (1-x)a_{AB} \quad \text{(III.3)}$$

$$c(AB_{1-x}C_x) = xc_{AC} + (1-x)c_{AB} \quad \text{(III.4)}$$

Where a_{AC}, c_{AC} and a_{AB}, c_{AB} are the lattice constants of AC and AB binary compounds, respectively. This law is only an approximate rule and one can observe either positive deviations or negative deviations with respect to linearity. We can express this deviation as follow:

$$a(AB_{1-x}C_x) = xa_{AC} + (1-x)a_{AB} - x(1-x)b \quad \text{(III.5)}$$

$$c(AB_{1-x}C_x) = xc_{AC} + (1-x)c_{AB} - x(1-x)b \quad \text{(III.6)}$$

Where *b* is called the bowing parameter. It represents these deviations from Vegard's law. By substituting the lattice parameters of the binary constituents by their values in the equations above, we notice that those equations are essentially a quadratic polynomial where the bowing parameter is the coefficient of the quadratic term.

The variation of the lattice parameters as a function of the composition *x* of the ternary alloys under study, is represented in the **Figure III.5(a)**, **Figure III.6(a)** and **Figure III.7(a)**. For the $ZnO_{1-x}S_x$ alloys, the lattice constants vary almost linearly with the composition and therefore obeys Vegard's law, and for the other two alloys $ZnO_{1-x}Se_x$ and $ZnO_{1-x}Te_x$, we notice a small negative deviation from linearity. This deviation from the linearity or Vegard's law is explained by the lattice mismatch between the ternary alloys and their binary constituents. By using a quadratic polynomial function to fit the calculated values, we found the following equations:

- For LDA:

$$ZnO_{1-x}S_x \begin{cases} a(x)^{LDA} = 3.19 + 0.76\,x - 0.21\,x^2 \\ c(x)^{LDA} = 5.18 + 1.02\,x - 0.08\,x^2 \end{cases} \quad \text{(III.7)}$$

$$ZnO_{1-x}Se_x \begin{cases} a(x)^{LDA} = 3.19 + 1.05\,x - 0.32\,x^2 \\ c(x)^{LDA} = 5.19 + 1.77\,x - 0.5\,x^2 \end{cases} \quad \text{(III.8)}$$

$$ZnO_{1-x}Te_x \begin{cases} a(x)^{LDA} = 3.19 + 1.84\,x - 0.8\,x^2 \\ c(x)^{LDA} = 5.19 + 2.92\,x - 1.2\,x^2 \end{cases} \quad \text{(III.9)}$$

- For PBE-GGA:

$$ZnO_{1-x}S_x\begin{cases}a(x)^{PBE-GGA} = 3.40 + 0.37\,x + 0.09\,x^2\\ c(x)^{PBE-GGA} = 5.51 + 0.47\,x + 0.33\,x^2\end{cases} \tag{III.10}$$

$$ZnO_{1-x}Se_x\begin{cases}a(x)^{PBE-GGA} = 3.38 + 0.87\,x - 0.17\,x^2\\ c(x)^{PBE-GGA} = 5.48 + 1.56\,x - 0.36\,x^2\end{cases} \tag{III.11}$$

$$ZnO_{1-x}Te_x\begin{cases}a(x)^{PBE-GGA} = 3.4 + 1.37\,x - 0.41\,x^2\\ c(x)^{PBE-GGA} = 5.52 + 2.21\,x - 0.6\,x^2\end{cases} \tag{III.12}$$

- For WC-GGA:

$$ZnO_{1-x}S_x\begin{cases}a(x)^{WC-GGA} = 3.25 + 0.63\,x - 0.04\,x^2\\ c(x)^{WC-GGA} = 5.21 + 1.06\,x + 0.01\,x^2\end{cases} \tag{III.13}$$

$$ZnO_{1-x}Se_x\begin{cases}a(x)^{WC-GGA} = 3.24 + 1.04\,x - 0.29\,x^2\\ c(x)^{WC-GGA} = 5.2 + 1.88\,x - 0.63\,x^2\end{cases} \tag{III.14}$$

$$ZnO_{1-x}Te_x\begin{cases}a(x)^{WC-GGA} = 3.25 + 1.66\,x - 0.61\,x^2\\ c(x)^{WC-GGA} = 5.2 + 1.88\,x - 0.63\,x^2\end{cases} \tag{III.15}$$

Figure III.5(b), **Figure III.6(b)** and **Figure III.7(b)** show the variation of the bulk modulus as a function of the composition *x*. This variation is compared with that obtained using the linear dependence on the composition. We observe a positive deviation of the bulk modulus for all the alloys, whereas the bowing parameter for $ZnO_{1-x}S_x$ is 76.19, 46.62, 30.95 from the LDA, PBE-GGA and WC-GGA, respectively. In the case of $ZnO_{1-x}Se_x$, its equal to 104.50, 100.82, 87.12 for LDA, PBE-GGA and WC-GGA, respectively. On the other hand, for the alloys $ZnO_{1-x}Te_x$, the deviation is equal to 166.59, 164.76, 146.30 from the LDA, PBE-GGA and WC-GGA, respectively. These deviations are attributed to the differences between the values of the bulk modulus of the binary compounds ZnO, ZnS, ZnSe and ZnTe.

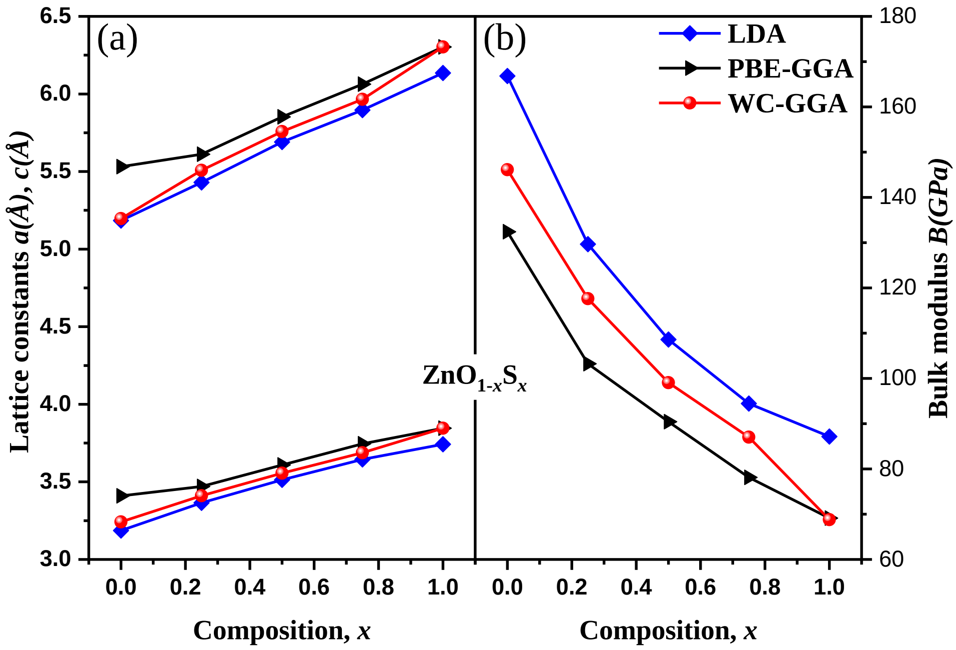

Figure III.5 Change in: (a) lattice parameters, (b) bulk modulus, as a function of composition for $ZnO_{1-x}S_x$ alloys.

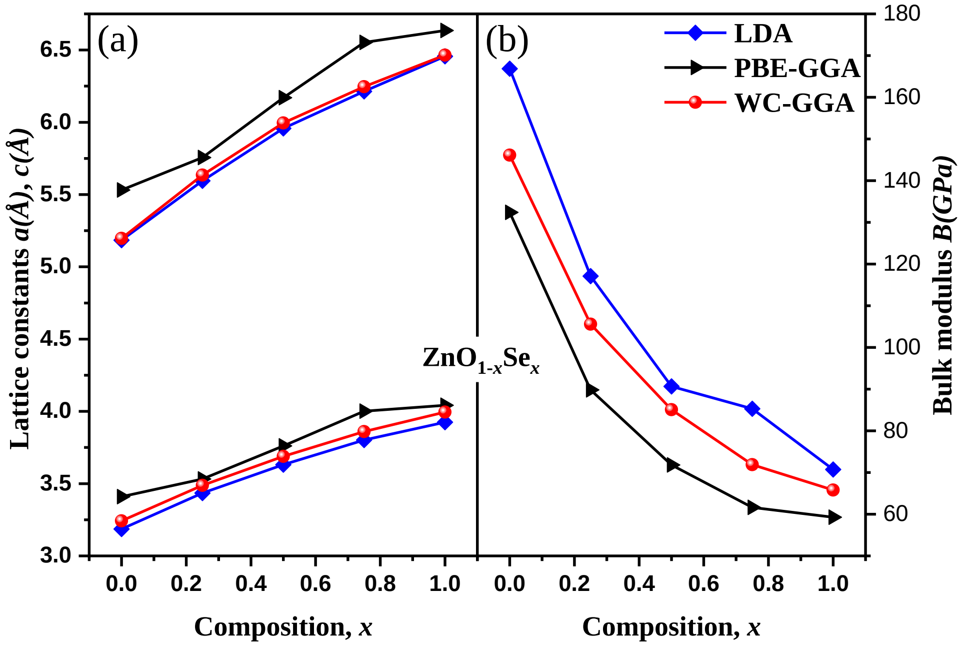

Figure III.6 Change in: (a) lattice parameters, (b) bulk modulus, as a function of composition for $ZnO_{1-x}Se_x$ alloys.

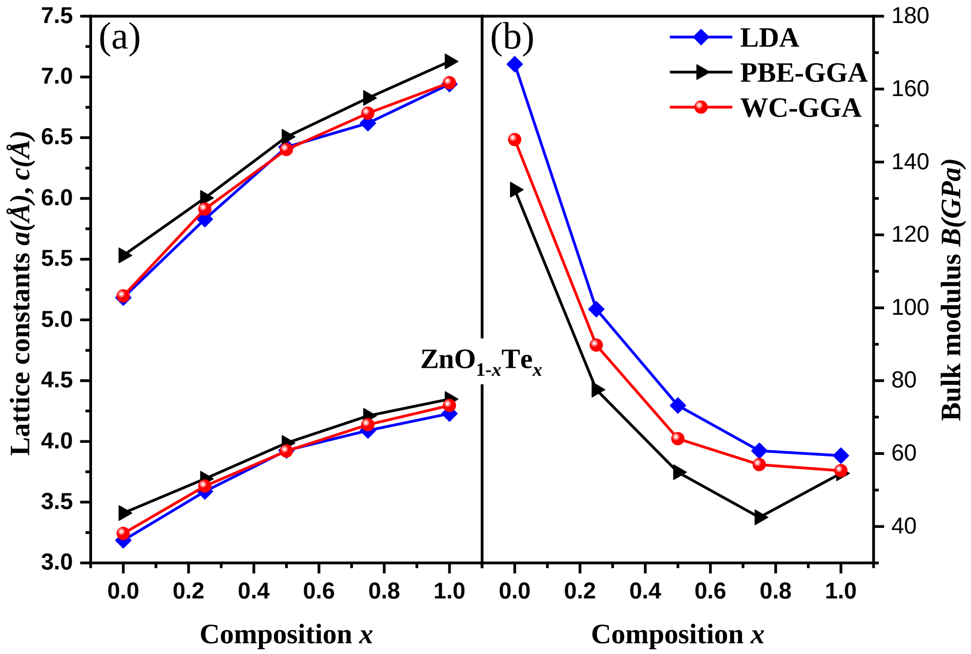

Figure III.7 Change in: (a) lattice parameters, (b) bulk modulus, as a function of composition for $ZnO_{1-x}Te_x$ alloys.

III.4 Electronic properties

III.4.1 Band structure

a. Binary compounds

The concept of energy bands plays a crucial role in understanding the behavior of electrons in a material. These energy bands describe the possible energies that an electron can possess as a function of its wave vector $\vec{k}$. In the case of semiconductors, the dispersion equation $E(\vec{k})$ becomes particularly significant as it provides valuable information about the electronic properties, such as band structures, gap energies (E_g), and densities of states.

In our study, we focused on computing the energy bands of several binary compounds, including ZnO, ZnS, ZnSe and ZnTe. To carry out these calculations, we employed the lattice parameters determined in the previous section and utilized two different approximations: PBE-GGA and TB-mBJ. Both of these approximations exhibit similar curve profiles. This is why only the curves obtained using TB-mBJ, are illustrated in **Figures III.8(a-d)**.

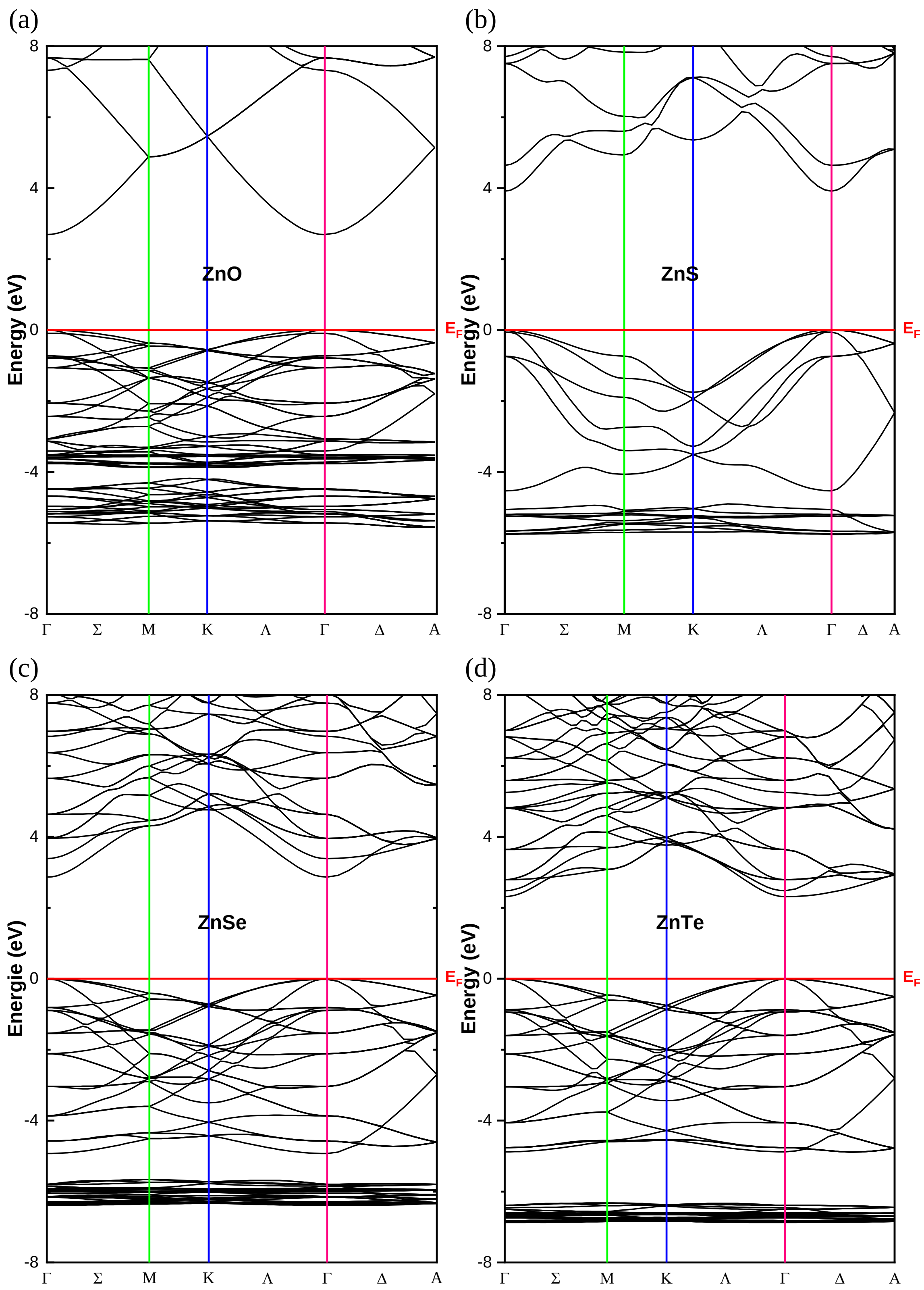

Figure III.8 Band structures of binary compounds ZnO, ZnS, ZnSe and ZnTe obtained by TB-mBJ.

By examining these curves, we can observe distinct characteristics of the compounds ZnO, ZnS, ZnSe and ZnTe. We can clearly see that these compounds are semiconductors. Moreover, in a semiconductor, if the highest point of the valence band and the lowest point of the conduction band coincide, we say that this semiconductor has direct band gap, if not, we say that it has indirect band gap. We notice that all the binary compounds exhibit a direct band gap in the Γ-Γ direction.

To quantify these observations, we have presented the energy gap results in **Table III.6**, which are also compared with experimental and theoretical data. It is worth noting that the energy gap values obtained using the PBE-GGA approximation tend to be underestimated when compared to experimental values. This disagreement with experimental data arises from a known limitation in density functional theory (DFT) for semiconductor materials. DFT in its standard form does not fully account for the electron-electron correlation effects and only gives simpler approximations to them, especially for systems with strongly correlated electrons, like transition metals and some insulators. These correlation effects can widen the band gap, but DFT's approximations tend to underestimate them.

However, our results obtained using the PBE-GGA approximation align well with the findings of other calculations. Notably, a significant improvement in the accuracy of the band gaps is observed when employing the modified Becke-Johnson functional (TB-mBJ). This functional demonstrates better agreement with experimental data in comparison to PBE-GGA. Importantly, the TB-mBJ approximation, proposed by Tran and Blaha, has also shown consistent results with other calculations. This approach led to good results for properties that depend on the accuracy of the exchange and correlation potential.

Table III.6 Bandgap energies in (eV) of ZnO, ZnS, ZnSe and ZnTe binary compounds.

Compound	**Band gaps direction**	**Our cal.**		**Other works.**	
		PBE-GGA	**TB-mBJ**	**Exp.**	**Theo.**
ZnO	$E_{\Gamma\to\Gamma}$	0.82	2.68[a, b]	3.3[c], 3.44[d]	2.65[e], 3.11[f]
ZnS	$E_{\Gamma\to\Gamma}$	2.066	3.914	3.91[d]	3.68[e], 3.91[f]
ZnSe	$E_{\Gamma\to\Gamma}$	0.75	2.45[a]	2.80[g]	3.02[f]
ZnTe	$E_{\Gamma\to\Gamma}$	1.49	2.31[b]	~1[h]	1.59[i], 2.67[j]

[a][8], **[b][9]**, **[c][30]**, **[d][31]**, **[e][27]**, **[f][28]**, **[g][32]**, **[h][33]**, **[i][35]**, **[j][22]**.

b. Ternary alloys

The study of the electronic properties of semiconductor alloys provides valuable information on their potential utility in the fabrication of electronic and optoelectronic devices. The electronic band structure of $ZnO_{1-x}S_x$, $ZnO_{1-x}Se_x$ and $ZnO_{1-x}Te_x$ ternary alloys computed using the (TB-mBJ) approach are shown in **Figures III.9(a-c)**, **Figures III.10(a-c)** and **Figures III.11(a-c)**, respectively. The valence band maxima (VBM) and conduction band minima (CBM) in each band structure are located in the same symmetry point Γ which clearly indicates that the studied materials are direct bandgap semiconductors. The bandgap energy of these alloys is investigated using both PBE-GGA and TB-mBJ approximations, and their results are summarized in **Table III.7**. Like the binary compounds, the bandgap energy computed with TB-mBJ approach is substantial ameliorated compared to that obtained through PBE-GGA approximation. As far we know, there is no experimental or theoretical data available for wurtzite $ZnO_{1-x}Te_x$ ternary alloys.

Table III.7 Bandgap energy values in (eV) of $ZnO_{1-x}S_x$, $ZnO_{1-x}Se_x$ and $ZnO_{1-x}Te_x$ ternary alloys.

Alloy	**x**	**Bandgap's direction**	**PBE-GGA**	**TB-mBJ**	**Other works.**
$ZnO_{1-x}S_x$	**0.25**	$E_{\Gamma\to\Gamma}$	1.316	3.112	2.83[c], 2.53[d], 2.80[e]
	0.5	$E_{\Gamma\to\Gamma}$	1.453	3.294	2.77[c], 2.47[d], 2.82[e]
	0.75	$E_{\Gamma\to\Gamma}$	1.813	3.590	3.03[c], 2.79[d], 3.18[e]
$ZnO_{1-x}Se_x$	**0.25**	$E_{\Gamma\to\Gamma}$	0.90[a]	2.71[a]	1.64[d]
	0.5	$E_{\Gamma\to\Gamma}$	0.75[a]	2.45[a]	1.46[d]
	0.75	$E_{\Gamma\to\Gamma}$	1.10[a]	2.64[a]	1.86[d]
$ZnO_{1-x}Te_x$	**0.25**	$E_{\Gamma\to\Gamma}$	0.77[b]	2.40[b]	-
	0.5	$E_{\Gamma\to\Gamma}$	0.46[b]	1.87[b]	-
	0.75	$E_{\Gamma\to\Gamma}$	0.88[b]	2.03[b]	-

[a] **[8]**, [b] **[9]**, [c] **[35]**, [d] **[28]**, [e] **[27]**.

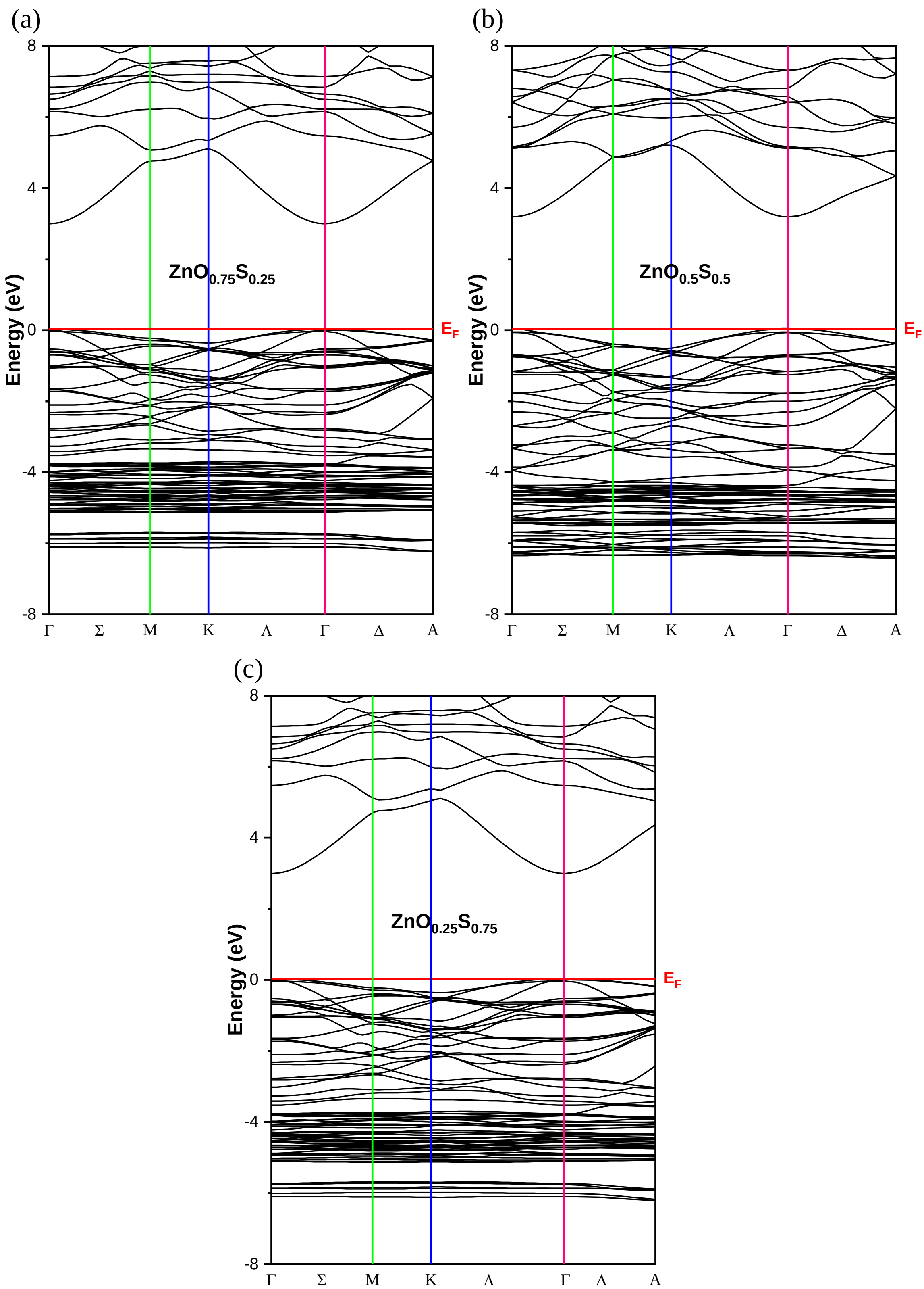

Figure III.9 Band structure of wurtzite $ZnO_{1-x}S_x$ ternary alloys obtained by TB-mBJ.

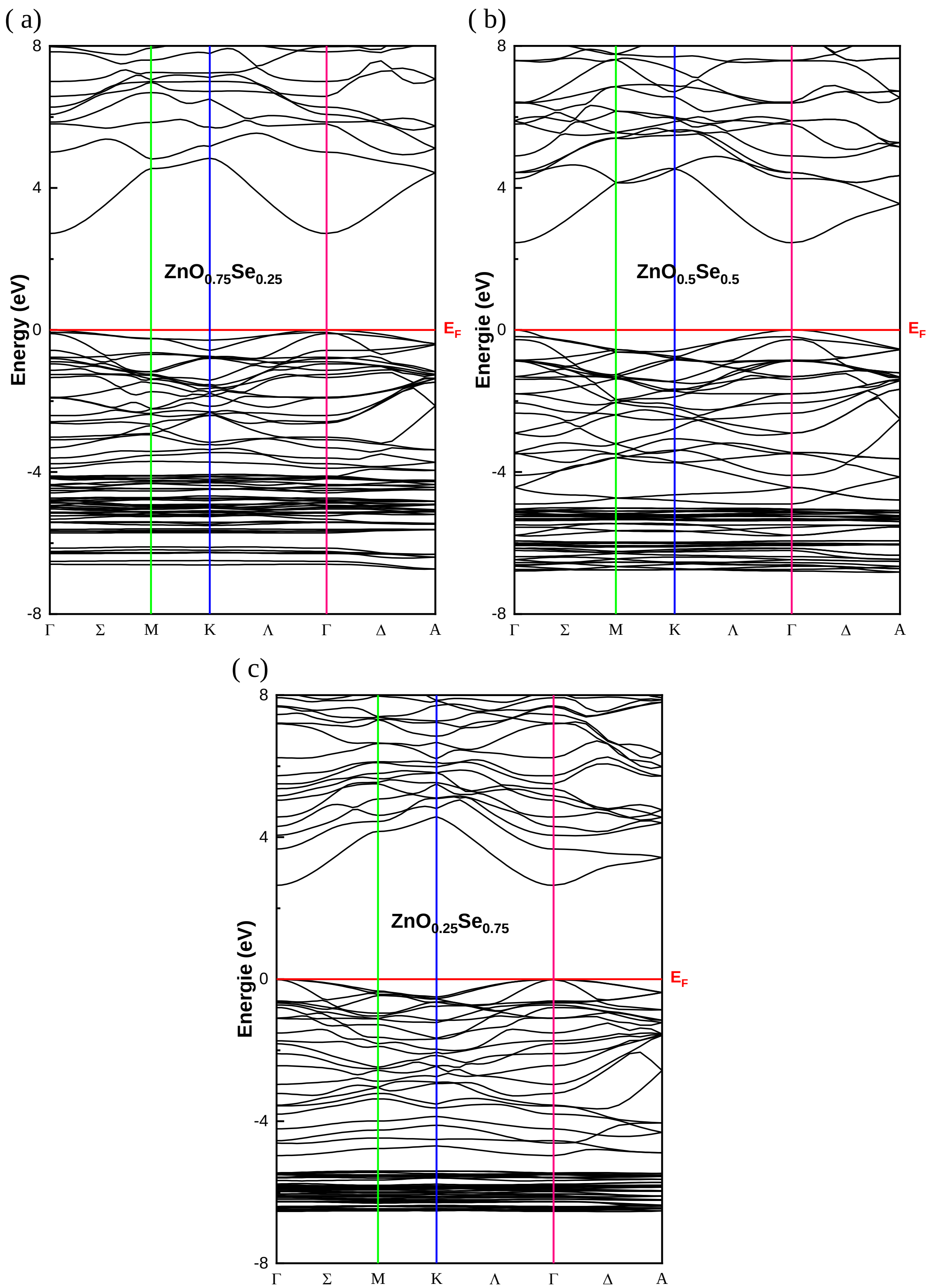

Figure III.10 Band structure of wurtzite teranry alloys $ZnO_{1-x}Se_x$ obtained by TB-mBJ.

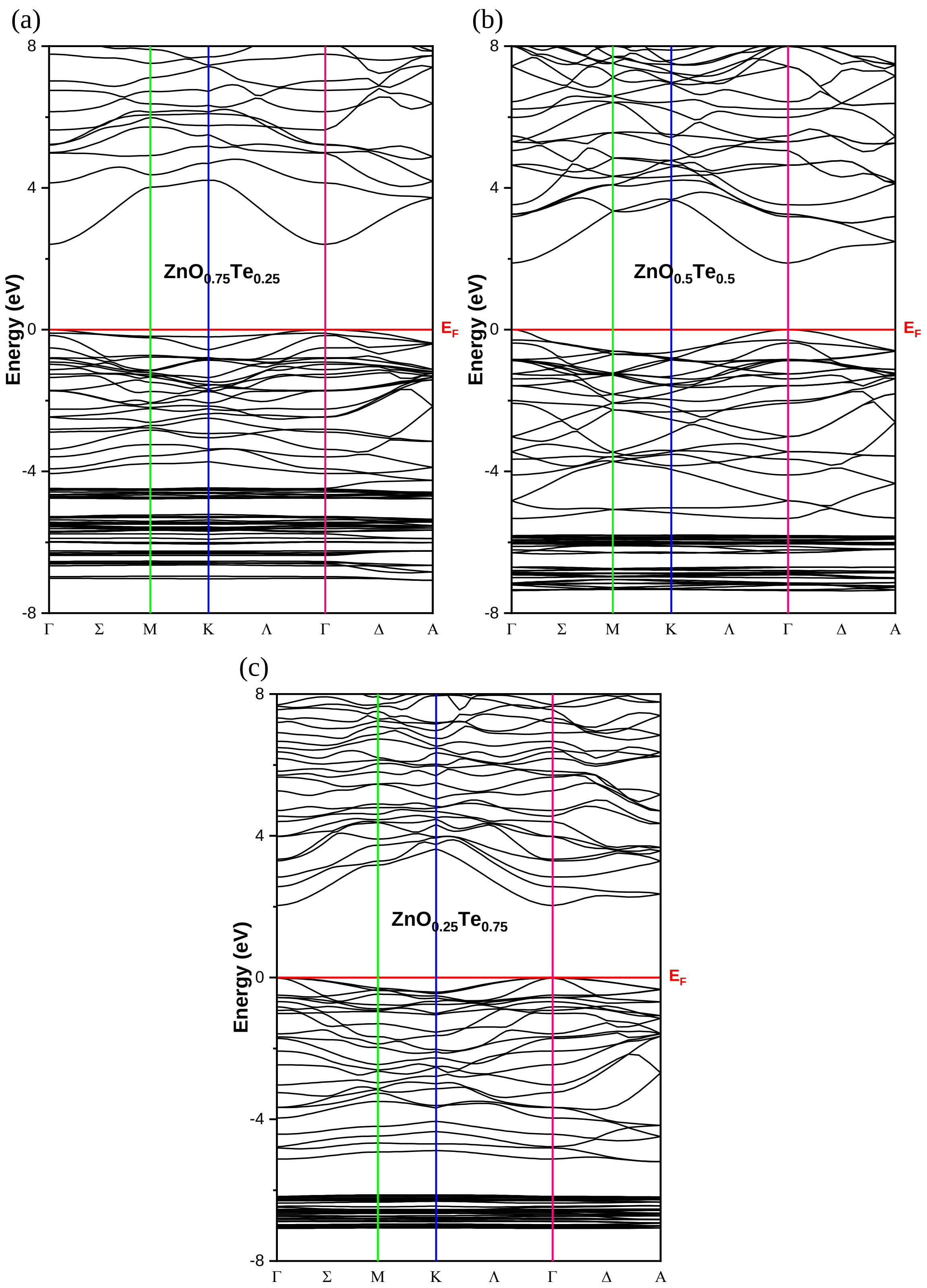

Figure III.11 Band structure of wurtzite teranry alloys $ZnO_{1-x}Te_x$ obtained by TB-mBJ.

The evolution of energy bandgap as a function of *x* as calculated by PBE-GGA and TB-mBJ approximations for $ZnO_{1-x}S_x$, $ZnO_{1-x}Se_x$ and $ZnO_{1-x}Te_x$ ternary alloys is depicted in **Figures III.12(a-c)**. The variations in bandgap energy with change in *x* can be well explained by the following quadratic formula **[36]**:

$$E = E_0 + ax + bx^2 \tag{III.16}$$

The deviation of bandgap from linear composition dependency can be described with the help of bowing parameter *b*. The bandgap energy variations obtained using the TB-mBJ and PBE-GGA are governed by the following equations:

$$ZnO_{1-x}S_x \begin{cases} E_{\Gamma\to\Gamma}(x)^{TP-mBJ} = 2.71 + 1.29x - 0.12x^2 \\ E_{\Gamma\to\Gamma}(x)^{PBE-GGA} = 0.86 + 1.50x - 0.3x^2 \end{cases} \tag{III.17}$$

$$ZnO_{1-x}Se_x \begin{cases} E_{\Gamma\to\Gamma}(x)^{TP-mBJ} = 2.73 - 0.83x + 0.94x^2 \\ E_{\Gamma\to\Gamma}(x)^{PBE-GGA} = 0.86 - 0.52x + 1.05x^2 \end{cases} \tag{III.18}$$

$$ZnO_{1-x}Te_x \begin{cases} E_{\Gamma\to\Gamma}(x)^{TP-mBJ} = 2.74 - 2.5x + 2.07x^2 \\ E_{\Gamma\to\Gamma}(x)^{PBE-GGA} = 0.89 - 1.76x + 2.34x^2 \end{cases} \tag{III.19}$$

The energy bandgap curves against change in *x* of $ZnO_{1-x}S_x$ alloys show a downward bowing parameter of -0.12 eV and -0.3 eV as calculated from PBE-GGA and TB-mBJ approximations, respectively. And for $ZnO_{1-x}Se_x$, the energy bandgap curves show an upward bowing parameter of 0.94 and 1.05 as calculated from PBE-GGA and TB-mBJ approximations, respectively. In the case of $ZnO_{1-x}Te_x$ ternary alloys, the curves also showed an upward bowing parameter of 2.07 eV for TB-mBJ approximation and 2.34 eV in the PBE-GGA approximation. These values of bowing parameter are attributed to difference in electronegativity of O (3.44) in one side and S (2.58), Se (2.55) and Te (2.1) on the other side. We observe that the more electronegativity difference gets bigger the more the bowing parameter value increase. Moreover, the bowing parameter *b* is originally divided into tree physical contributions; the first term is volume deformation representing the relative response of the binary constituents to hydrostatic pressure between the equilibrium lattice constants from these binary compounds to their ternary alloy. The second one is charge exchange contribution described by charge transfer in bringing the binary compounds to the ternary alloys. The last term is the structural relaxation due to the change of the bandgap upon passing from the unrelaxed to the relaxed alloy **[37]**.

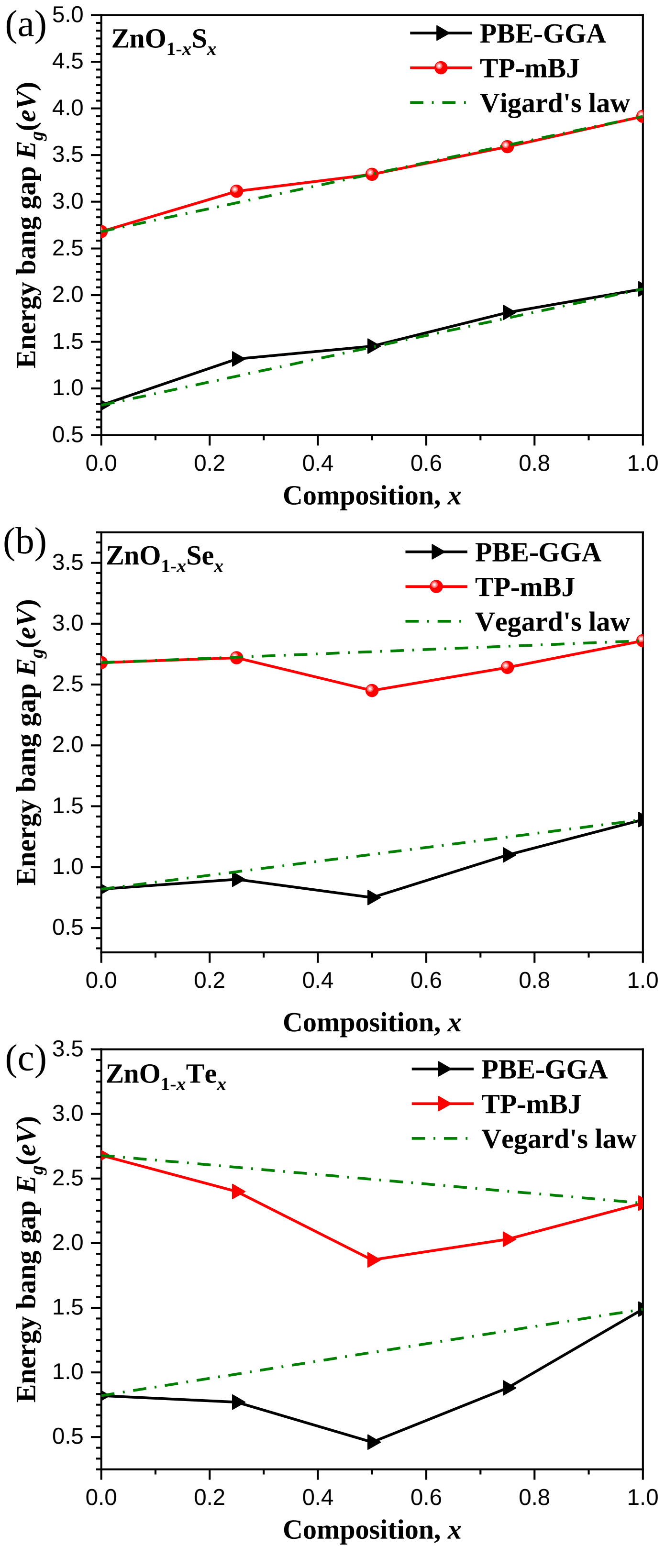

Figure III.12 Changes in the bandgap energies as a function of the x composition of the $ZnO_{1-x}S_x$, $ZnO_{1-x}Se_x$ and $ZnO_{1-x}Te_x$ ternary alloys.

III.4.2 Density of states DOS

a. Binary compounds

The computed total density of states (TDOS) and partial density of states (PDOS) of ZnO, ZnS, ZnSe and ZnTe are shown in **Figures III.13(a-d)**. There are three distinct regions in the TDOS spectrum: the lower valence band (LVB), the upper valence band (UVB), and the conduction band (CB). For ZnO, the DOS is shown in **Figure III.13a**. The LVB is essentially dominated by O-2s states with a few contributions from Zn-3p and Zn-4s states. Whereas, the UVB is mainly formed by Zn-3d and O-2p states with a small contribution from Zn-3p-4s states. The CB is created by the combined contribution of Zn-4s-3p states with a few participations of O-2p states.

For the ZnS, **Figure III.13b** shows that the LVB is mainly formed by the contribution of the S-3s states with small contribution from Zn-4s-3p states. The UVB region is dominated by mixture of the Zn-3d states and S-3p with a small contribution from the Zn-4s-3p. The CB is formed by a mixture of the Zn-4s-3p and S-3s3p states.

The TDOS and PDOS of ZnSe are depicted in **Figure III.13c**. The LVB is formed by the contribution of Se-4s states with a small contribution of Zn-4s-3p states, and the UVB is dominated by the Zn-3d states with a small contribution of the Zn-3s and Se-4p states. The CB region is essentially formed by the contributions of Zn-4s-3p states with a small participation of Se-4p-3d states.

The DOS of ZnTe compound is shown in **Figure III.13d**, the LVB region is formed essentially by the contribution of Te-4s states, and the UVB region is constructed by the both participation of Zn-4s, Zn-3d states, up the Fermi level the CB region is dominated by a mixture contribution of Zn-4s, Zn-3p states with the Te-3d states.

Furthermore, for the binary compounds, there is large contribution of Zn-3d, O-2s to the valence band, while the Zn-4s states contribute to the formation of the conduction band, these compounds exhibit semiconducting nature with a distinctive bandgap up the Fermi level. Therefore Zn-3d states are broadened between -3 eV and -6 eV and according to the photoemission results, the Zn-3d state could be situated at about -6 eV in the valence band **[38]**.

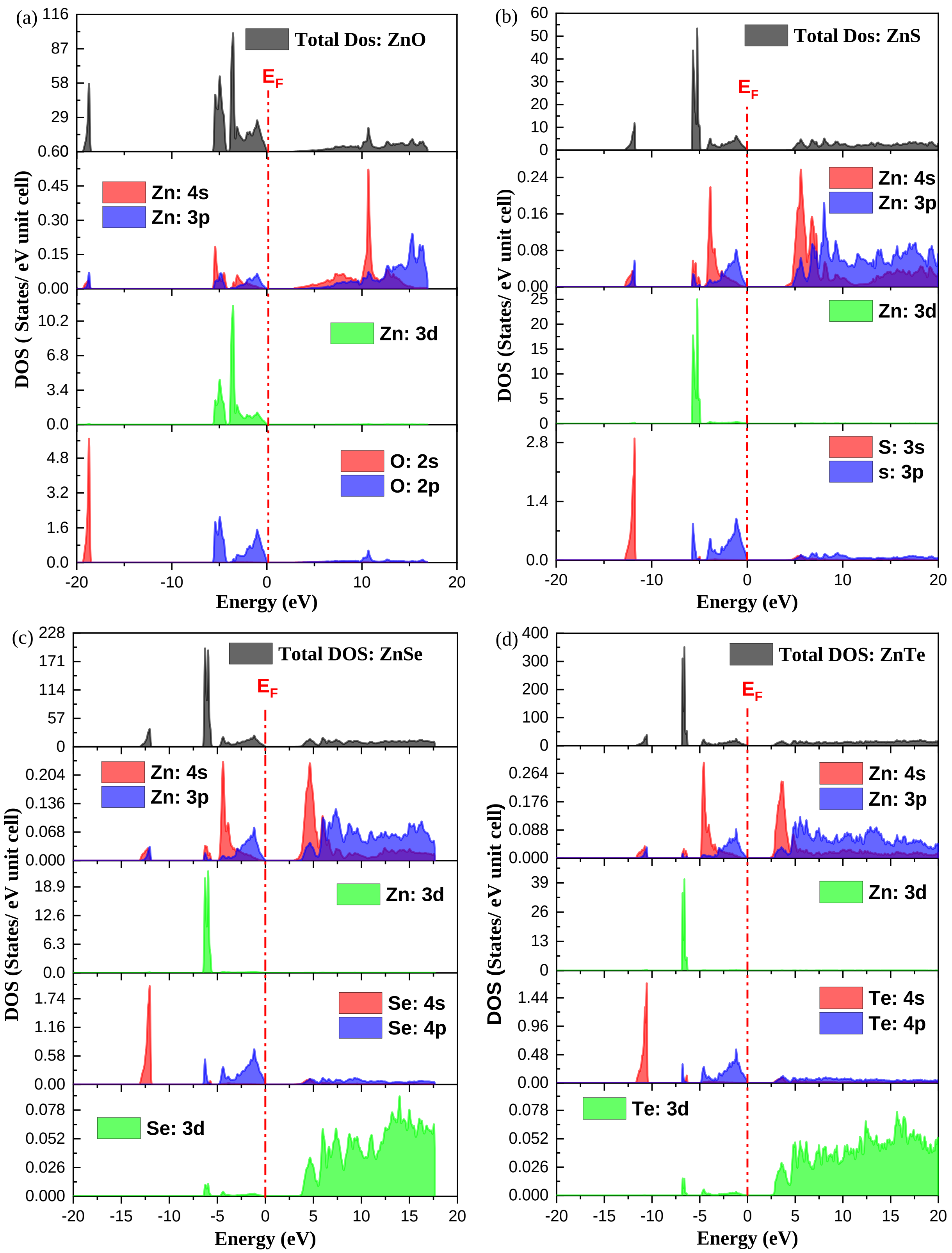

Figure III.13 Total (T-DOS) and partial (P-DOS) density of states of ZnO, ZnS, ZnSe and ZnTe obtained by TB-mBJ.

b. Ternary alloys

We calculated the total and partial densities of states (P-DOS) of $ZnO_{1-x}S_x$, $ZnO_{1-x}Se_x$ and $ZnO_{1-x}Te_x$ in the wurtzite phase. As prototypes the **Figures III.14(a-c)** illustrates the total and partial densities of $ZnO_{0.5}S_{0.5}$, $ZnO_{0.5}Se_{0.5}$ and $ZnO_{0.5}Te_{0.5}$ obtained by TB-mBJ approach. From these figures we observe the same behavior of (DOS) like we saw in binary materials where the curves of the total density of states (TDOS) are constructed by three distinct regions; the first one is the lower valence band (LVB), the second region is the upper valence band (UVB) and third is the conduction band region (CB).

The TDOS and PDOS of the wurtzite $ZnO_{0.5}S_{0.5}$ ternary alloy are depicted in **Figure III.14a**. The LVB is mainly formed by the contribution of the O-2s and S-3s states with a small contribution for Zn-4s-3p states. The UVB is due to the Zn-3d, O-2p and S-3p states with a small contribution for Zn-4s-3p states. The CB is essentially due to the mixture of all atomic states.

For $ZnO_{0.5}Se_{0.5}$ alloy that we have chosen as prototype, the DOS is plotted in **Figure III.14b** which shows that the LVB is formed by the contribution of O-2s and Se-4s states. The UVB is dominated by the participation of Zn-4s-3p states with a small contribution of O-2p and Se-4p states. The CB is formed by the mixture contribution of Zn-4s-3p, O-2p and Se-4p-3d states.

The **Figure III.14c**, present the total and partial DOS of the $ZnO_{0.5}Te_{0.5}$ ternary alloy that we have chosen as prototype ternary alloy. The region of LVB is predominated by the participation of O-2s, Te-4s states but the UVB region is formed by the contribution of the Zn-4s, Zn-3d states and with a few participations of the Te-4p, Te-3d states. Moreover, the CB region of alloy is dominated by the contribution of Zn-4s, Zn-3p states and with considerable participation of Te-3d states.

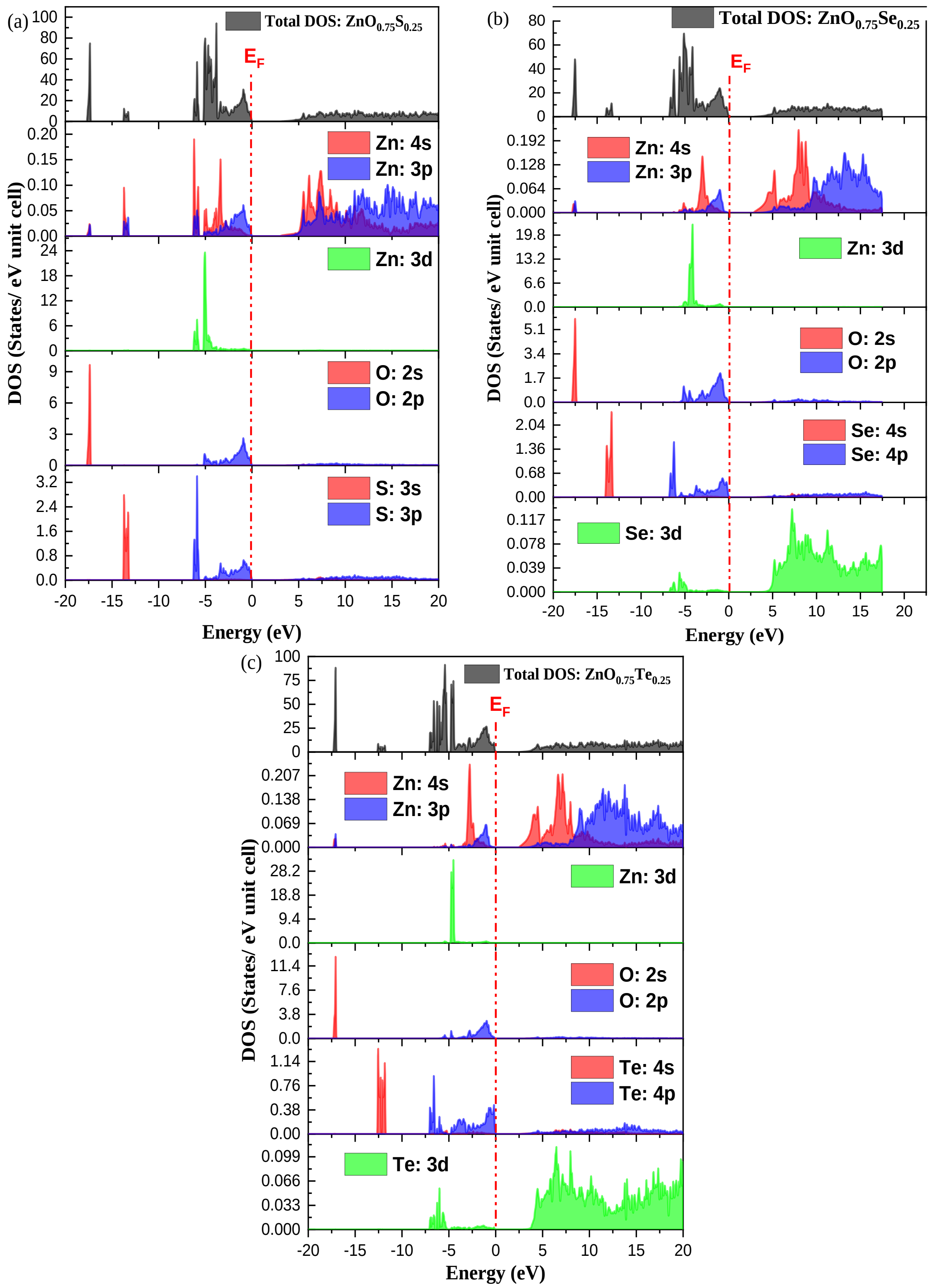

Figure III.14 Total (T-DOS) and partial (P-DOS) density of states of $ZnO_{0.5}S_{0.5}$, $ZnO_{0.5}Se_{0.5}$ and $ZnO_{0.5}Te_{0.5}$ obtained by TB-mBJ.

III.5 Optical properties

The optical properties allow us to understand the interaction of light with matter. These properties are strongly correlated with the electronic properties, especially the bandgap. We can describe the response of any material to electromagnetic radiation by knowing its complex dielectric function [$\varepsilon(\omega)=\varepsilon_1(\omega)+i\varepsilon_2(\omega)$]. The imaginary part of dielectric function is equivalent to the sum of all possible transitions between occupied and unoccupied states. It is also closely related to the band structure of the material. Following formula is used to determine the imaginary part of dielectric function $\varepsilon_2(\omega)$ **[39]**:

$$\varepsilon_2(\omega) = \frac{e^2\hbar}{\pi m^2\omega^2}\sum_{v,c}\int_{BZ}|M_{cv}(k)|^2[\omega_{cv}(k)-\omega]d^3 \qquad \text{(III.20)}$$

The integral is across the first Brillouin zone and $M_{cv}(k)$ is the momentum dipole elements which is given as:

$$M_{cv}(k) = u_{ck}|e\nabla|u_{vk} \qquad \text{(III.21)}$$

The real part of dielectric function $\varepsilon_1(\omega)$ is related to the imaginary part through well-known Kronig relation **[40]**:

$$\varepsilon_1(\omega) = 1 + \frac{2}{\pi}P\int_0^{\infty}\frac{\omega'\varepsilon_2(\omega')}{\omega'^2-\omega^2}d\omega' \qquad \text{(III.22)}$$

Where P represents the principal value of the integral. The knowledge of real and imaginary components of the dielectric function enables us to compute the other important optical functions including refractive index **[41]**:

$$n(\omega) = \left[\frac{\varepsilon_1(\omega)}{2} + \frac{\sqrt{\varepsilon_1^2(\omega)+\varepsilon_2^2(\omega)}}{2}\right]^{\frac{1}{2}} \qquad \text{(III.23)}$$

At low frequency (ω=0), the refractive index becomes:

$$n(0) = \varepsilon^{1/2}(0) \qquad \text{(III.24)}$$

We have employed other empirical and theoretical models that they used to get the refractive index of materials from the knowledge of the bandgap, these models are listed in the following expressions:

An empirical relation shape proposed by Tripathy **[42]** given as:

$$n = n_0\left[1+\alpha e^{-\beta E_g}\right] \qquad \text{(III.25)}$$

Where n_0, α and β are fitted parameters, with the values 1.73, 1.9017 and 0.539 (eV^{-1}), respectively.

A linear relation of Ravindra, Auluck and Srivastava written as [43]:

$$n = \alpha + \beta E_g \tag{III.26}$$

Where $\alpha = 4.084$ and $\beta = -0.62$ eV^{-1}.

The reflectivity can be deduced from the following formula:

$$R(\omega) = \left|\frac{\sqrt{\varepsilon(\omega)} - 1}{\sqrt{\varepsilon(\omega)} + 1}\right|^2 \tag{III.27}$$

The absorption coefficient is explained in term of real and imaginary parts of the dielectric function as:

$$\alpha(\omega) = \frac{\sqrt{2}\omega}{c}\left[\sqrt{\varepsilon_1^2(\omega) + \varepsilon_2^2(\omega)} - \varepsilon_1(\omega)\right]^{\frac{1}{2}} \tag{III.28}$$

One should mention that since we are dealing with hexagonal symmetry, the optical properties can be calculated in the *xx* and *zz* direction. But our results showed that the behavior of optical properties in those directions is almost identical. Based on that, we only present results in the *xx* direction.

III.5.1 Binary compounds

The real part of the dielectric function provides information about how a material responds to an external electric field in terms of polarization, electric susceptibility, dielectric constant, and optical properties. It is a crucial parameter in understanding and characterizing the electrical and optical behavior of materials. The real parts versus the photon energy of the ZnO, ZnS, ZnSe and ZnTe binary compounds are represented in **Figure III.15a**. One can see clearly that the curves picked at 5.73 eV, 5.11 eV and 4.22 eV for ZnS, ZnSe and ZnTe, respectively. After that we notice a sharp decrease indicating the anomalous region. This dispersion describes the decrease of dielectric function in an absorption band. Following that, we observe an increase in the three curves. Since that increase happened in an area with no absorption, we say that there is a normal dispersion. We notice that ZnO curve behave differently, it exhibits three picks around 2.88 eV, 8.14 eV and 11.63 eV. After the last pick, the curve decreases slower than other curve showing

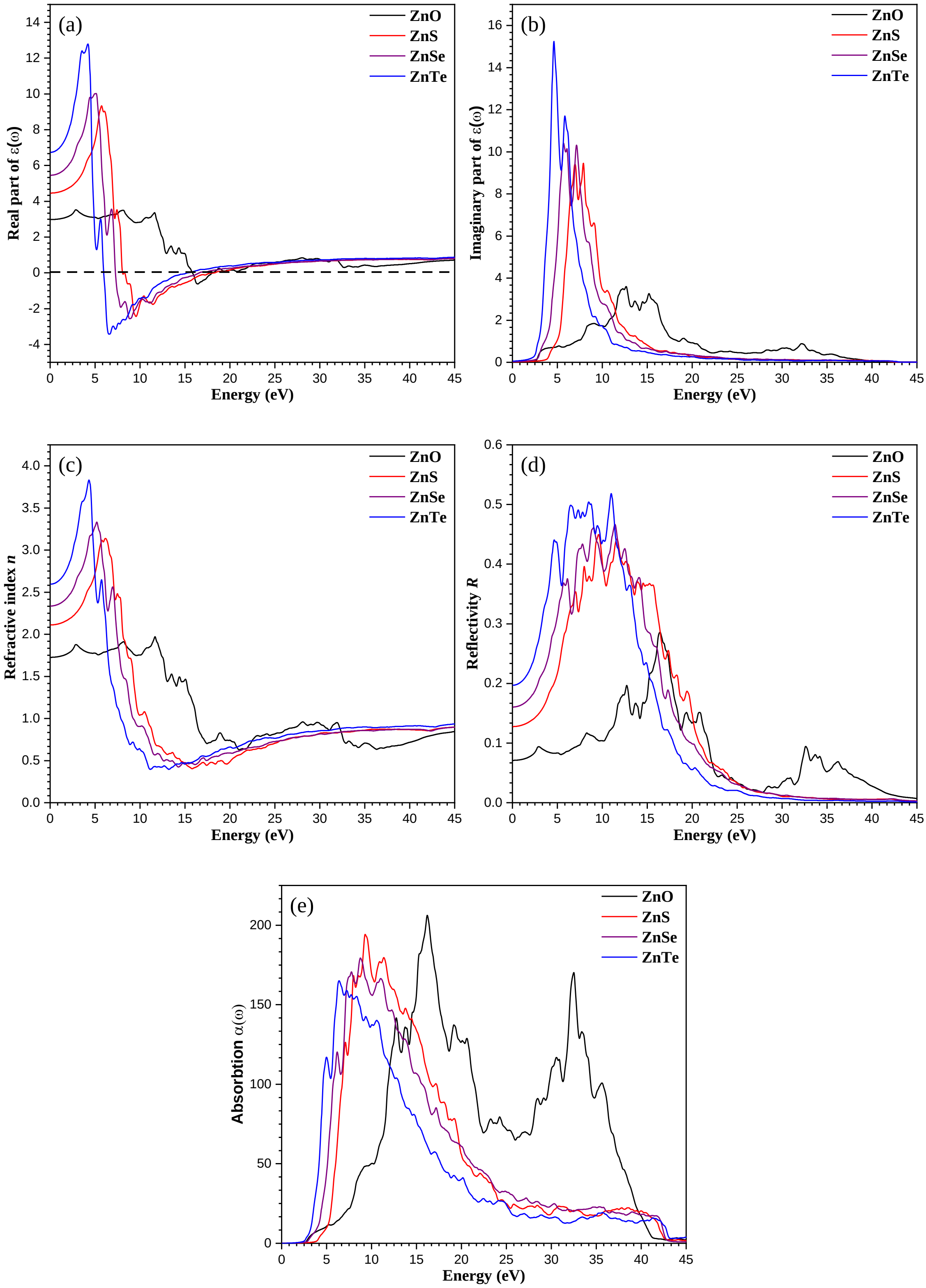

Figure III.15 Real Parts (a), Imaginary Parts (b), Refractive Indices (c), Reflectivity Indices (d), and Absorption Coefficients (e) of ZnO, ZnS, ZnSe and ZnTe binary compounds.

larger anomalous region, then it increases again showing tighter normal dispersion region. At high energies, all the curve tends to small steady values. The dielectric constant of the studied materials is deduced by the intercept of the real part curves with *y* axes where the values are given in the **Table III.8**.

the imaginary part of the dielectric function provides information about how a material absorbs and dissipates energy when exposed to an external electromagnetic field. It is crucial in understanding the optical and electrical properties of materials, as well as in designing and analyzing devices and systems that involve energy absorption, such as detectors, sensors, and optical filters. The imaginary parts of the binary compounds ZnO, ZnS, ZnSe and ZnTe are plotted in **Figure III.15b**. It is clear that for all binary compounds, the spectra of the imaginary part have two main peaks. They are located in the energy values of 12.66 eV and 15.19 eV for the ZnO compound, 6.95 eV and 7.9 eV for the ZnS compound, 5.69 eV and 7.12 eV for the ZnSe compound and 4.61 eV and 5.85 eV for the ZnTe compound. Additionally, we have observed small humps in the right side of the main major peaks located at the energy values of 19 eV, 9.04 eV, 8.42 eV and 9.18 eV for the ZnO, ZnS, ZnSe and ZnTe materials, respectively. Furthermore, there is also a small hump in the left side of the main major peak observed at the energy values of 2.80 eV, 3.81 eV, 2.85 eV and 2.45 eV for the ZnO, ZnS, ZnSe and ZnTe materials, respectively. Generally, the first left humps correspond to the direct optical transition between the maximum of the valence band and the minimum of conduction band.

The refractive index quantifies how light interacts with and propagates through a material. It governs the speed of light, the bending of light at boundaries, the optical density of the material, and the phenomena of dispersion and total internal reflection. This property is essential in optics and has practical applications in optoelectronics field. The refractive index as a function of photon energy for the binary compounds ZnO, ZnS, ZnSe and ZnTe are shown in **Figure III.15c**. For ZnS, ZnSe and ZnTe, the curve of the refractive index has a small peak before the major one with small humps in the right-side region. The major peaks are situated at energy values of 6.14 eV, 5.2 eV and 4.33 eV for the ZnS, ZnSe and ZnTe compounds, respectively. The refractive index increases with the increase of photon energy until the major peak, after that it decreases with the increase of photon energy. For ZnO, we notice three major peaks observed at values 2.85 eV, 8.19 eV and 11.67 eV. After these major peaks, the refractive index decreases with the increase of energy. The first major peaks often indicate the inter-band transition of electrons. While the other two maybe are an indication of intraband transition or a resonance phenomenon occurring. The static refractive index is the value of refractive index at zero frequency, and it's shown in **Table III.8**.

Reflectivity refers to the ratio of reflected light to incident light upon interaction with a material. It provides information about how a material reflects incident electromagnetic radiation as a function of the energy of the photons. The frequency-dependent reflectivity *R(ω)* of the ZnO, ZnS, ZnSe and ZnTe binary compounds is presented in **Figure III.15d**. The reflectivity of ZnS, ZnSe and ZnTe compounds increases with the increase of photon energy. We notice four major peaks in each curve of them situated in the energy rang of 4.60 eV to 15.67 eV. After that, we observe a small humps in the right-side of the curves. For ZnO, we can clearly see a major peak situated between two minor peaks, this major peak has the reflectivity percentage of 28% and energy value 16.42 eV. At zero energy, the reflectivity values are 07 %, 12.76%, 16.03% and 19.70% for ZnO, ZnS, ZnSe and ZnTe compounds respectively.

Absorption refers to the process in which a material absorbs incident electromagnetic radiation. The absorption curve provides information about the energy levels and electronic transitions within the material. The absorption coefficient *α(ω)* as a function of photon energy is presented in **Figure III.15e** for all the binary alloys. For ZnS, ZnSe and ZnTe, we can observe that the absorption coefficient increases with the increase of photon energy until the peak positioned approximately at 9.29 eV, 8.79 eV and 6.44 eV for ZnS, ZnSe and ZnTe, respectively. After these values the absorption coefficient decreases slowly as the photon energy increases. For ZnO, we notice two major peaks positioned in between two minor peaks, these major peaks situated at 16.25 eV and 32.51 eV. We observe that the reflectivity peaks are situated at nearly the same photon energy as peaks in the absorption coefficients.

Table III.8 Static dielectric constant and refractive index of ZnO, ZnS, ZnSe and ZnTe binary compounds.

Compound	Parameters	TB-mBJ	PBE-GGA	*S. K. Tripathy* 2015	*Ravindra, Auluck 1973*	Exp.	Theo.
ZnO	n	1.72[a, b]	2.17[a, b]	2.5	2.42	1.69[c]	1.71[d], 1.63[e]
	ε_1	2.98[a, b]	4.74[a, b]	6.27	5.86	2.89[c]	2.91[d], 2.68[e]
ZnS	n	2.11	2.47	2.13	1.66	2.28[f]	1.5[g]
	ε_1	4.46	6.10	4.54	2.76	6.1[f]	4.60[h]
ZnSe	n	2.33[a]	2.69[a]	2.61	2.57	2.168[i]	2.30[k]
	ε_1	5.45[a]	7.27[a]	6.81	6.60	7.6[j]	5.66[l]
ZnTe	n	2.60[b]	2.96[b]	2.67	2.65	2.7[m]	-
	ε_1	6.76[b]	8.76[b]	7.13	7.02	-	-

[a]**[8]**, [b]**[9]**, [c]**[44]**, [d]**[45]**, [e]**[46]**, [f]**[47]**, [g]**[48]**, [h]**[27]**, [i]**[49]**, [j]**[50]**, [k]**[51]**, [l]**[52]**, [m]**[33]**.

III.5.2 Ternary alloys

The real parts of $ZnO_{1-x}S_x$ ternary materials are shown in the **Figure III.16a**. In the region situated between 0.66 eV and 6.08 eV, the real parts of the dielectric function increase as the photon energy increases until it reaches its peak, this corresponds to the normal dispersion region. After that, these quantities decrease with the increase of photon energy which is corresponds to the abnormal dispersion. Also, we notice increase in amplitude and shift toward lower energies when increasing the composition.

The imaginary parts are represented in the **Figure III.16b** which are related to the $ZnO_{1-x}S_x$ ternary alloys. The main (major) peak is located at the energy's values of 10 eV 7.44 eV and 7.02 eV for compositions of 0.25, 0.5 and 0.75, respectively. Furthermore, we have also observed a small hump at the left side of the major peaks for the same alloy in the position energy of 2.53 eV, 2.72 eV and 2.96 eV, this peak corresponds to the direct optical transition between the maximum of the valence band and the minimum of conduction band. Following these major peaks, the imaginary part curves decrease with the increase of energy.

we should mention that the intensity of the major peaks increases when we go from 0.25 to 0.75.

The refractive indices of the $ZnO_{1-x}S_x$ ternary alloys are computed and plotted in **Figure III.16c**. For the $ZnO_{0.5}S_{0.5}$ and $ZnO_{0.25}S_{0.75}$ alloys, the principal peaks of *n(ω)* spectrum are located at the energy values of 5.88 eV and 6.80 eV with a magnitude of 2.64 and 2.92, respectively. After these peaks, the refractive index decreases with the increase of photon energy. In this region we notice small humps in the three curves. In the case of the $ZnO_{0.75}S_{0.25}$ ternary alloy, we notice three major peaks situated at energy values of 3.18 eV, 6.09 eV and 9.5 eV with a magnitude of 2.09, 2.22 and 1.99, respectively. For all ternary alloys, we notice a steady refractive index values at higher energies.

Figure III.16d, give the frequency-dependent reflectivity *R(ω)* for $ZnO_{1-x}S_x$ ternary alloys. The maximum of reflectivity occurs at the photon energy range of 5.45 eV-13 eV. The highest reflectivity's are situated at energy values of 15.18 eV, 9.72 eV and 12.20 eV with magnitude of 26.64 %, 30.96 % and 38.62 % and *x* compositions of 0.25, 0.5 and 0.75, respectively. At zero energy, the reflectivity values are found to be equal 9.25 %, 11.14 % and 12.38 % for the compositions 0.25,0.5 and 0.75, respectively. One can conclude that the reflectivity amplitude is increased with increase of Sulfur doped atoms.

Figure III.16e show the calculated absorption coefficient dispersion *α(ω)* of the ternary alloys $ZnO_{1-x}S_x$ for different compositions. The absorption curves increase with the increase of energy until they reach maximum absorption situated at energy values 13.9 eV, 12.34 eV and 9.5 eV for the compositions 0.25, 0.5 and 0.75, respectively. We can clearly see the doping more sulfur cause increasing in the absorption peaks.

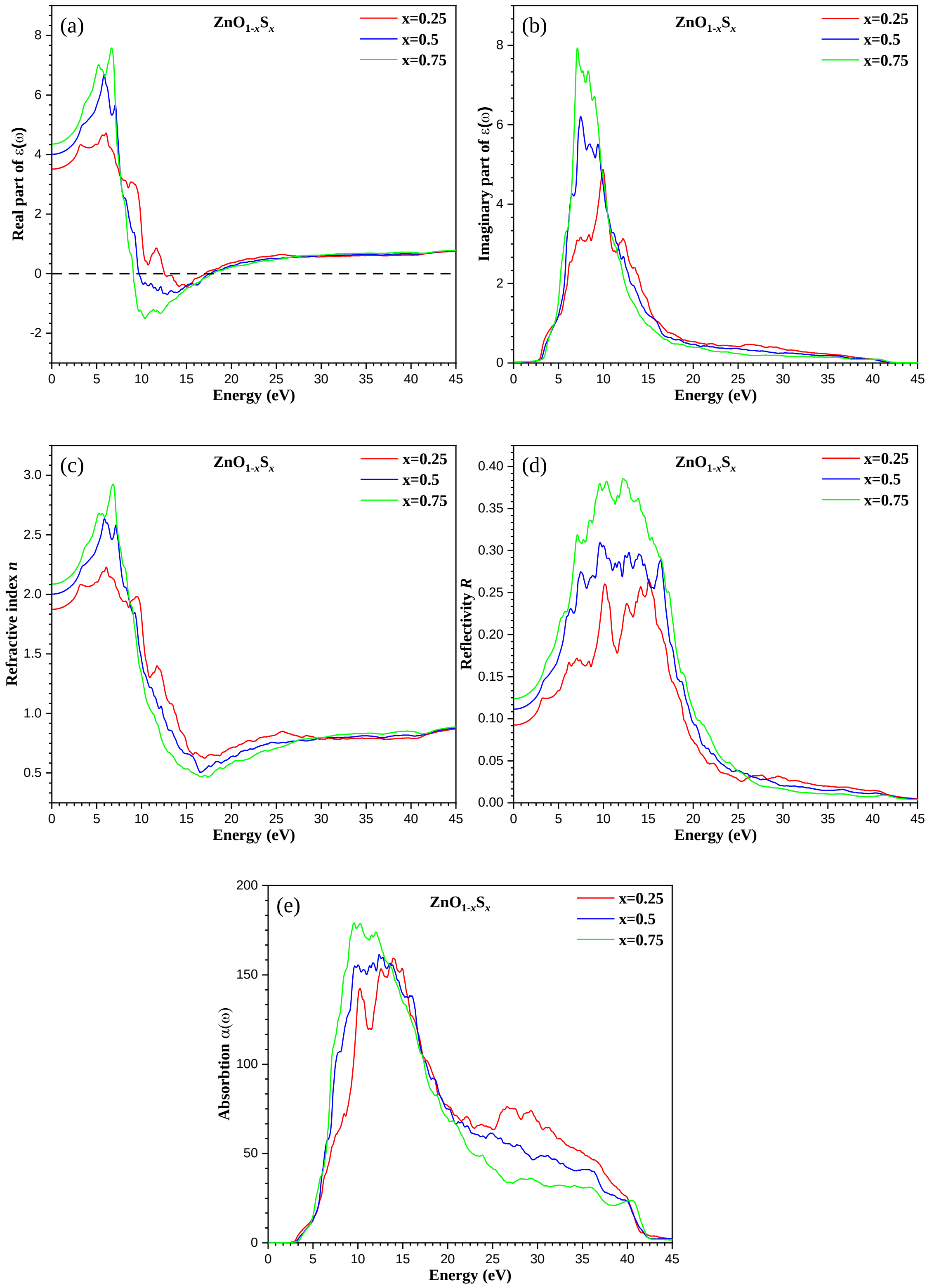

Figure III.16 Real Parts (a), Imaginary Parts (b), Refractive Indices (c), Reflectivity Indices (d), and Absorption Coefficients (e) of $ZnO_{1-x}S_x$ ternary alloys.

The curves for real part of dielectric function of $ZnO_{1-x}Se_x$ depicted in **Figure III.17a**. It is obvious that the value of dielectric function is increased with increase in photon energy over the region 2.33-5.8 eV. Afterward, the value of dielectric function decreases with increase in photon energy in the same region, indicating the anomalous dispersion. As the composition x is gradually increased from 0 to 1, the real part of dielectric function is shifted towards the lower photon energy with an augmentation in their amplitudes. However, when the photon energy becomes zero, the values of dielectric constant of the samples is decreased.

Figure III.17b shows the variation in imaginary part of dielectric function $\varepsilon_2(\omega)$ as a function of photon energy for $ZnO_{1-x}Se_x$ alloys. One can clearly see that the $\varepsilon_2(\omega)$ curves have major peaks between the two small humps. The value of $\varepsilon_2(\omega)$ increases with increase in photon energy until the major peaks are obtained at 9.56, 6.54 and 6.19 eV for respective change in x as 0.25, 0.50 and 0.75. The right small humps are located at 12.09, 7.82 and 7.76 eV for the same respective aforementioned compositions. Afterward, the value of $\varepsilon_2(\omega)$ decreases with increase in photon energy. Moreover, the left small humps are found at 5.12, 3.44, 4.83 and 4.88 eV for x as 0, 0.25, 0.50 and 0.75, respectively. It is observed that the curves of imaginary part of dielectric function shift towards the lower energy with gradual increase in x.

Figure III.17c shows the refractive index $n(\omega)$ of $ZnO_{1-x}Se_x$ ternary alloys as a function of photon energy. It has major peaks at 5.91, 5.26 and 5.89 eV corresponding to the amplitude of 2.27, 2.76 and 2.95 for the values of x as 0.25, 0.50 and 0.75, respectively. We notice a shift toward lowest energies as we increase the Selenium 'Se' composition.

Figure III.17d illustrates the frequency-dependent reflectivity $R(\omega)$ of $ZnO_{1-x}Se_x$ alloys. The value of reflectivity increases with increase in photon energy and its major peaks are observed at 14.38, 11.08 and 11.74 eV for composition x as 0.25, 0.50 and 0.75, respectively. There appeared a few humps in left region of the principal peak; whereas in right region, the reflectivity decreased as the photon energy is increased. At zero energy, the reflectivity values are found to be 10.18, 12.65 and 14.51 % for composition x as 0.25, 0.50 and 0.75, respectively. It is concluded that the reflectivity of the studied materials is increased by ~2 % with increase in x from 0.25 to 0.75.

The absorption coefficient $\alpha(\omega)$ profiles of proposed alloys and compounds are presented in **Figure III.17e**. The absorption edges are produced due to electronic transitions from fully occupied valence band to least populated conduction band. The fundamental

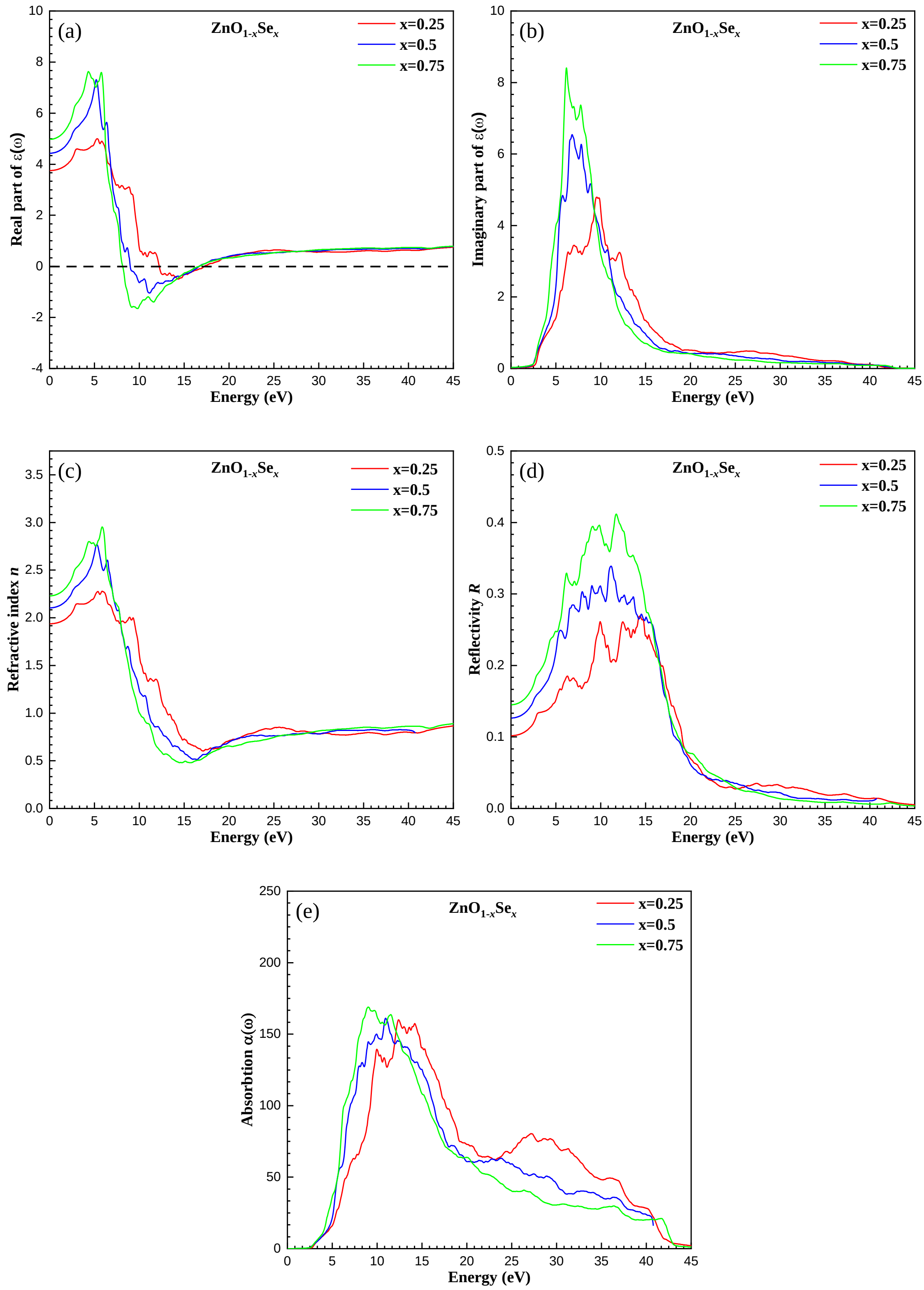

Figure III.17 Real Parts (a), Imaginary Parts (b), Refractive Indices (c), Reflectivity Indices (d), and Absorption Coefficients (e) of $ZnO_{1-x}Se_x$ ternary alloys.

absorption region is found to be about 2.66, 2.51 and 2.61 eV for compositions *x* as 0.25, 0.50 and 0.75, respectively. The value of $\alpha(\omega)$ increases as the photon energy increases, and reach to maximum for energy 12.39, 10.95 and 8.99 eV for corresponding composition *x* as 0.25, 0.50 and 0.75. Furthermore, the absorption coefficient decreases as the photon energy increases just after the major peaks.

The optical properties such as the real with imaginary parts of the dielectric function, refractive index, reflectivity and absorption coefficients of the ternary alloys $ZnO_{0.25}Te_{0.75}$, $ZnO_{0.5}Te_{0.5}$ and $ZnO_{0.75}Te_{0.25}$ are investigated as function of the incident photon energy at the constant composition *x* values, where the results are presented in the **Figures III.18(a-e)**. The real parts of the studied materials are given in the **Figure III.18a**, there are two different regions observed for the real parts spectrums, the first one is delimited from 4.19 eV to 16.32 eV corresponding to the abnormal dispersion region, in which the real parts curves increase with the increases of photon energy. The second one exists over the region (4.19 eV- 16.32 eV), the real parts spectrums decrease with the increase of photon energy indicating the normal dispersion region.

The imaginary parts as function of photon energy of the alloys are depicted in **Figure III.18b**, by analyzing these spectrums; one can clearly see that there is one major peak situated between other two small humps. The major peaks are located at energy values of 8.36 eV, 5.64 eV and 5.04 eV corresponding to the Tellurium 'Te' compositions 0.25, 0.5 and 0.75, respectively. Moreover, there are also a small humps observed in right side region of the main major peak positioned at 7.76 eV and 7.97 eV for the compositions 0, 0.5 and 0.75, respectively. It is noted that this hump is disappeared in the case of the $ZnO_{0.75}Te_{0.25}$ ternary alloy. Additionally, the other humps of the left side region are observed only for 0.25 at the energy values of 5.59 eV. The first small hump of the left side region is corresponding to the direct optical transition between the maximum of the valence band and the minimum of the conduction band.

The refractive indices versus of photon energy for the ternary alloys are presented in **Figure III.18c**. The curves of $n(\omega)$ increase with increase of photon energy until the principal peaks located at 4.66 eV, 4.14 eV and 4.66 eV which have the magnitudes of 2.46, 2.96 and 3.28 for the compositions 0.25, 0.5 and 0.75, respectively. Furthermore, the curves decrease rapidly with the increase of photon energy to reach a minimum occurred in the values 16.06 eV, 13.89 eV and 13.37 eV for the compositions 0.25, 0.5, 0.75, respectively.

After that the refractive index spectrums increase with the energy and tend toward a limit value at approximately 45 eV.

The frequency-dependent reflectivity *R(ω)* of the ternary alloys is represented in **Figure III.18d**. The reflectivity curves increase with the increase of photon energy crossing successive peaks at the left side of the main peak, after that the *R(ω)* decrease with the increase of photon energy in the right side of the main peak. The values of the major peaks are 8.74 eV, 9.75 eV and 7.95 eV corresponding to the compositions 0.25, 0.5 and 0.75, respectively. At zero energy, the reflectivity values are 11.6%, 15.3% and 17.93% with a respect of the same compositions.

The absorption coefficient *α(ω)* of materials as a function of photon energy is depicted in **Figure III.18e**. The curves of *α(ω)* increase as the photon energy increases until the maximum absorption values at 11.90 eV, 8.50 eV and 7.74 eV for the compositions 0.25, 0.5 and 0.75, respectively. After that the absorption coefficient spectrums decrease with the increase of photon energy.

Table III.9 summarizes the calculated values of static dielectric constant and refractive index of $ZnO_{1-x}S_x$, $ZnO_{1-x}Se_x$ and $ZnO_{1-x}Te_x$ ternary alloys. The refractive index and dielectric function have been plotted against the compositions of the ternary alloys in the **Figures III.19-21**. Their values are increased with increase value of x from 0 to 1. The variations in refractive index and dielectric constant as a function of composition is determined from the quadratic fit which obeys the following expression:

$$ZnO_{1-x}S_x \begin{cases} n(x)^{TP-mBJ} = 1.72 + 0.73\,x - 0.33\,x^2 \\ \varepsilon(x)^{TP-mBJ} = 2.96 + 2.64\,x - 1.12\,x^2 \\ n(x)^{PBE-GGA} = 2.17 + 0.59\,x - 0.30\,x^2 \\ \varepsilon(x)^{PBE-GGA} = 4.75 + 2.62\,x - 1.28\,x^2 \end{cases} \quad \text{(III.29)}$$

$$ZnO_{1-x}Se_x \begin{cases} n(x)^{TP-mBJ} = 1.72 + 0.90\,x - 0.30\,x^2 \\ \varepsilon(x)^{TP-mBJ} = 2.96 + 3.29\,x - 0.83\,x^2 \\ n(x)^{PBE-GGA} = 2.17 + 0.85\,x - 0.33\,x^2 \\ \varepsilon(x)^{PBE-GGA} = 4.75 + 3.81\,x - 1.28\,x^2 \end{cases} \quad \text{(III.30)}$$

$$ZnO_{1-x}Te_x \begin{cases} n(x)^{TP-mBJ} = 1.72 + 1.37\,x - 0.49\,x^2 \\ \varepsilon(x)^{TP-mBJ} = 2.96 + 5.18\,x - 1.37\,x^2 \\ n(x)^{PBE-GGA} = 2.17 + 1.42\,x - 0.63\,x^2 \\ \varepsilon(x)^{PBE-GGA} = 4.75 + 6.78\,x - 2.71\,x^2 \end{cases} \quad \text{(III.31)}$$

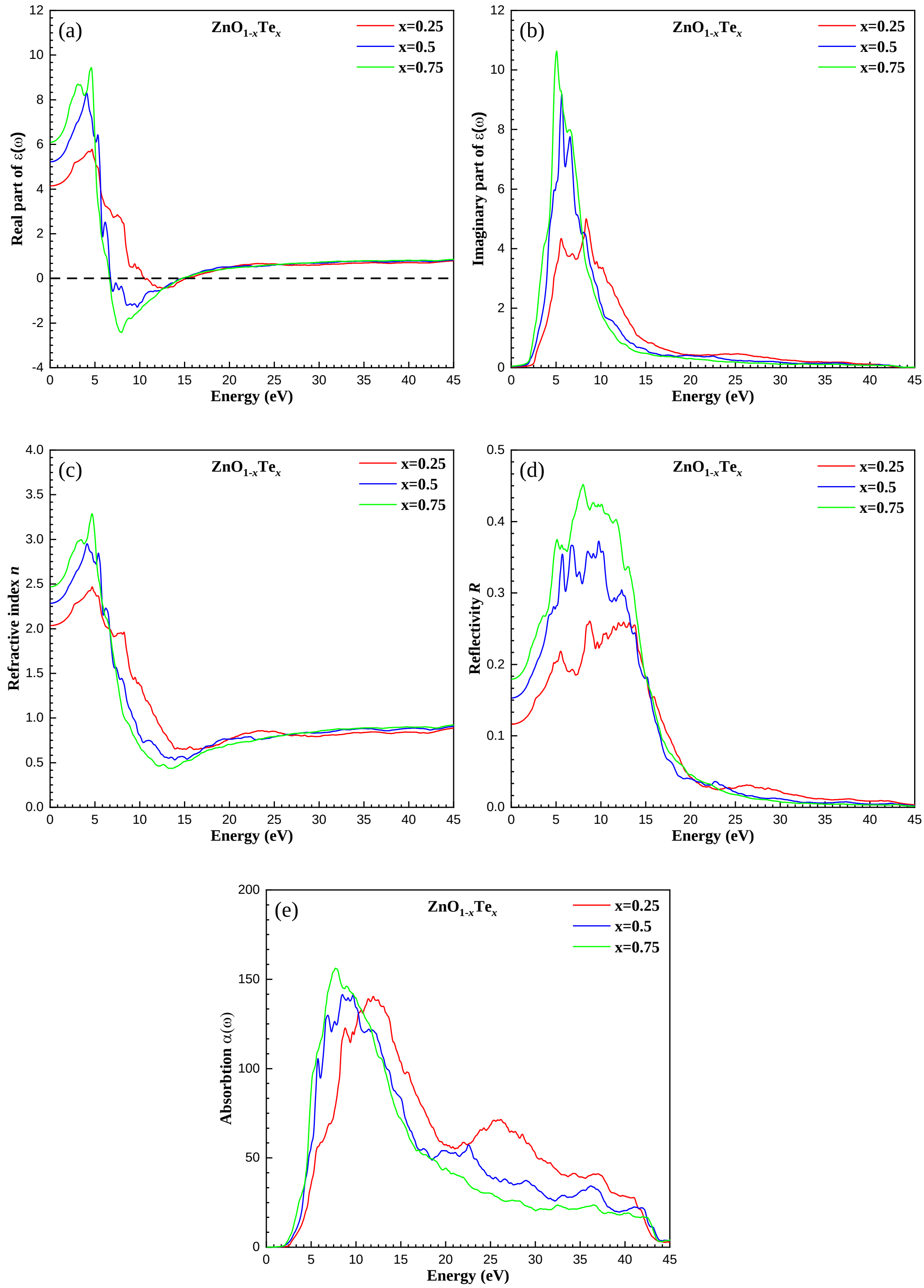

Figure III.18 Real Parts (a), Imaginary Parts (b), Refractive Indices (c), Reflectivity Indices (d), and Absorption Coefficients (e) of $ZnO_{1-x}Te_x$ ternary alloys.

Table III.9 Static dielectric constant and refractive index of $ZnO_{1-x}S_x$, $ZnO_{1-x}Se_x$ and $ZnO_{1-x}Te_x$ ternary alloys.

Alloy	***x***	**Parameters**	**TB-mBJ**	**PBE-GGA**	***S. K. Tripathy* 2015**	***Ravindra, Auluck 1973***	**Theo.**	**Exp.**
$ZnO_{1-x}S_x$	**0.25**	n	1.87	2.31	2.34	2.15	-	-
		ε_1	3.51	5.36	5.48	4.62	-	-
	0.5	n	2.00	2.39	2.29	2.04	-	-
		ε_1	4.00	5.72	5.24	4.16	-	-
	0.75	n	2.08	2.45	2.21	1.86	-	-
		ε_1	4.35	6	4.88	3.46	-	-
$ZnO_{1-x}Se_x$	**0.25**	n	1.93[a]	2.36[a]	2.49	2.40	-	-
		ε_1	3.75[a]	5.58[a]	6.20	5.76	-	3.46[c]
	0.5	n	2.10[a]	2.52[a]	2.61	2.57	-	-
		ε_1	4.43[a]	6.36[a]	6.81	6.60	-	3.94[c]
	0.75	n	2.23[a]	2.61[a]	2.52	2.45	-	-
		ε_1	4.97[a]	6.84[a]	6.35	6.00	-	4.30[c]
$ZnO_{1-x}Te_x$	**0.25**	n	2.04[b]	2.47[b]	2.63	2.60	-	-
		ε_1	4.14[b]	6.13[b]	6.92	6.76	-	-
	0.5	n	2.28[b]	2.73[b]	2.93	2.92	-	-
		ε_1	5.22[b]	7.48[b]	8.58	8.53	-	-
	0.75	n	2.47[b]	2.88[b]	2.83	2.83	-	-
		ε_1	6.10[b]	8.29[b]	8.01	8.01	-	-

[a]**[8]**, [b]**[9]**, [c] **[27]**.

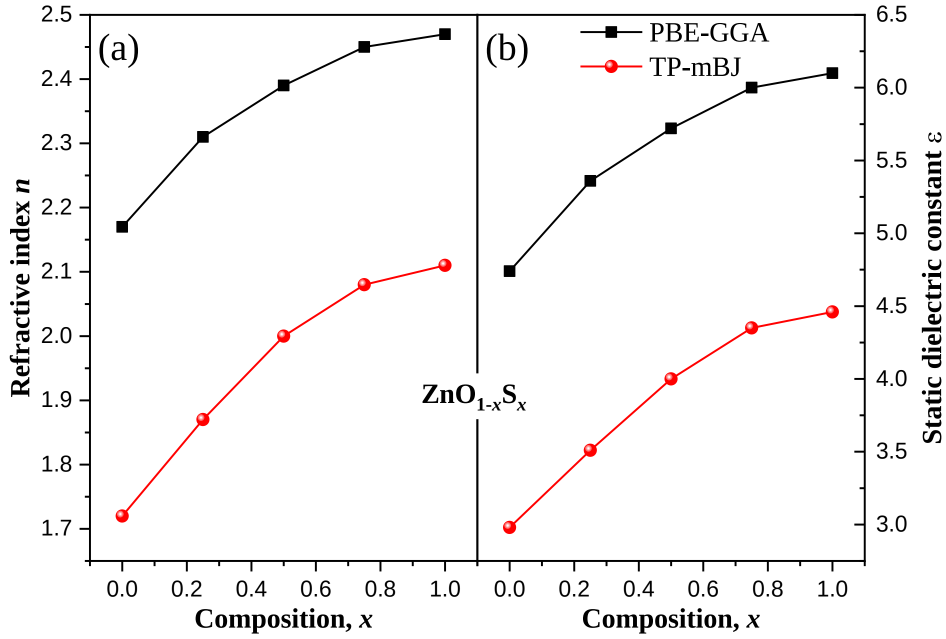

Figure III.19 Changes in: (a) the static dielectric constant and (b) refractive index, as a function of the composition x of $ZnO_{1-x}S_x$ ternary alloys.

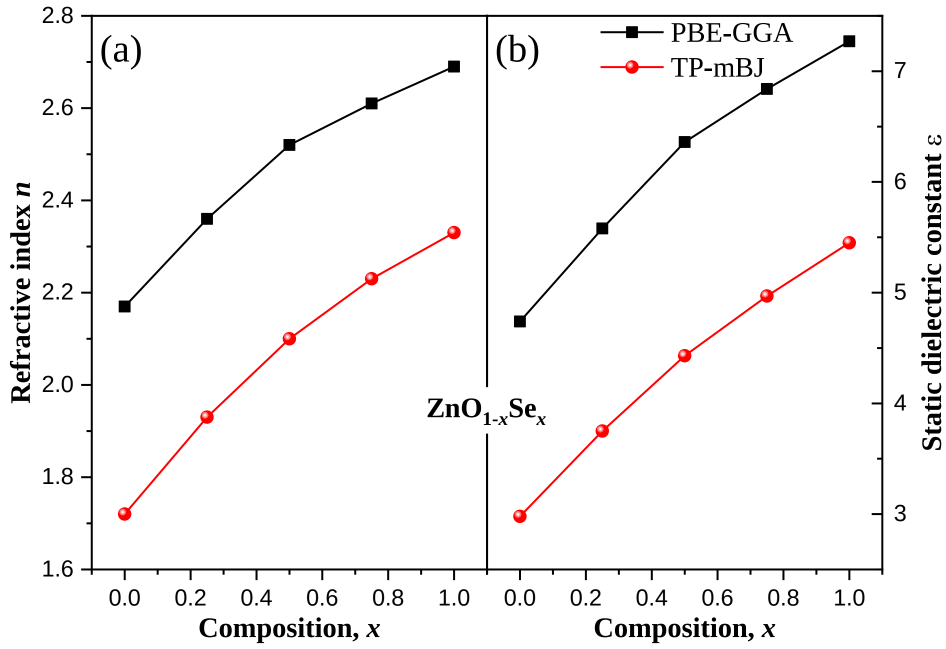

Figure III.20 Changes in: (a) the static dielectric constant and (b) refractive index, as a function of the composition x of $ZnO_{1-x}Se_x$ ternary alloys.

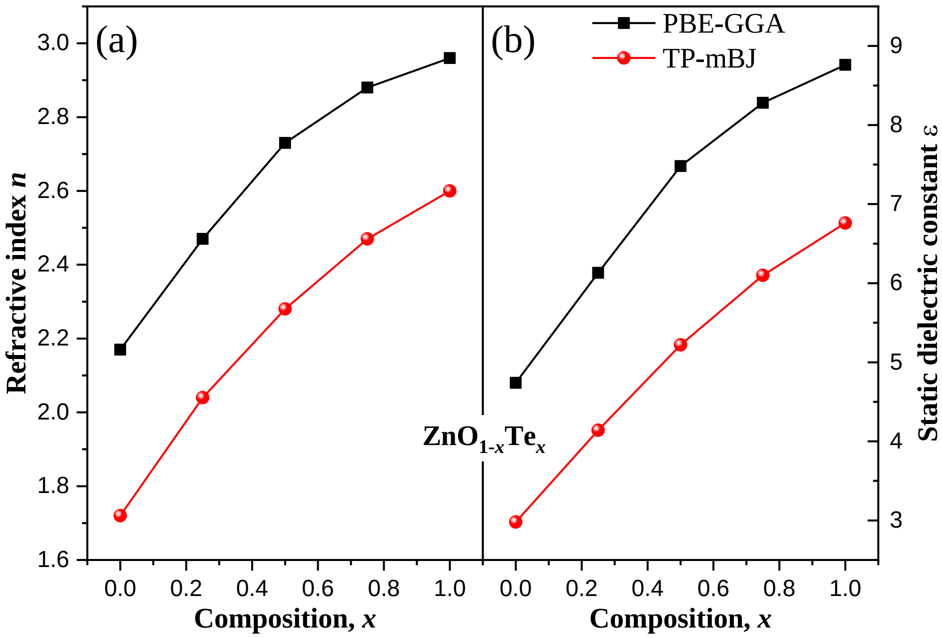

Figure III.21 Changes in: (a) the static dielectric constant and (b) refractive index, as a function of the composition x of $ZnO_{1-x}Te_x$ ternary alloys.

III.6 Elastic properties

The elastic properties of wurtzite $ZnO_{1-x}S_x$, $ZnO_{1-x}Se_x$ and $ZnO_{1-x}Te_x$ and their binary ZnO, ZnS, ZnSe and ZnTe compounds have been investigated using the IRelast tool which can be employed in Wien2k package **[53]**. The knowledge of elastic constants C_{ij} gives important information about response of a material to an external applied strain. For hexagonal crystals, there are five independent components of elastic constant tensor: C_{11}, C_{12}, C_{13}, C_{33}, and C_{55}. In order to calculate the elastic constant C_{ij}, we expand the total energy $E(V,\alpha)$ of the crystal into a Taylor series in terms of the distortion parameters **[54]**:

$$E(V,\delta) = E(V_0,0) + V_0\left(\sum_{i=1}^{6} \tau_i\delta_i + \frac{1}{2}\sum_{i=1}^{6}\sum_{j=1}^{6} C_{ij}\delta_i\delta_j + O(\delta^3)\right) \qquad \text{(III.32)}$$

Where: V_0 is the equilibrium volume of the crystal, τ_i is the stress tensor components and δ_i is the components of the strain tensor.

Since, there are five elastic constants, so there will be five different strains **[55]**. The first distortion can be written as:

$$\begin{pmatrix} 1+\delta & 0 & 0 \\ 0 & 1+\delta & 0 \\ 0 & 0 & 1 \end{pmatrix} \quad \text{(III.33)}$$

It applies a uniform tension in *xy-plane* while keeping the *z-axis* constant. The volume of strain lattice increases, but the symmetry remains hexagonal. The energy for this distortion can be derived by substituting the strain matrix into the energy formula which gives:

$$E(V,\delta) = E(V_0,0) + V_0\delta(\tau_1+\tau_2) + V_0\big((C_{11}+C_{12})\delta^2 + O(\delta^3)\big) \quad \text{(III.34)}$$

The second strain keeps the crystal volume unchanged. The symmetry changes to orthorhombic, and the strain matrix takes the form:

$$\begin{pmatrix} \left(\frac{1+\delta}{1-\delta}\right)^{1/2} & 0 & 0 \\ 0 & \left(\frac{1-\delta}{1+\delta}\right)^{1/2} & 0 \\ 0 & 0 & 1 \end{pmatrix} \quad \text{(III.35)}$$

As a result, **Equation III.32** becomes:

$$E(V,\delta) = E(V_0,0) + V_0\big((C_{11}-C_{12})\delta^2 + O(\delta^3)\big) \quad \text{(III.36)}$$

In third strain, the crystal remains hexagonal and tension is applied along the *z-axis*. In this case, the strain matrix can be written as:

$$\begin{pmatrix} 1 & 0 & 0 \\ 0 & 1 & 0 \\ 0 & 0 & 1+\delta \end{pmatrix} \quad \text{(III.37)}$$

Now, the energy **Equation III.32** becomes:

$$E(V,\delta) = E(V_0,0) + V_0\delta(\tau_3) + V_0\left((C_{33})\frac{\delta^2}{2} + O(\delta^3)\right) \quad \text{(III.38)}$$

The elastic constant C_{55} can be obtained by applying a deformation that causes the crystal structure transition to triclinic symmetry. The strain matrix is then written as:

$$\begin{pmatrix} 1 & 0 & \delta \\ 0 & 1 & 0 \\ \delta & 0 & 1 \end{pmatrix} \quad \text{(III.39)}$$

Where, the **Equation III.32** can be rearranged as:

$$E(V,\delta) = E(V_0,0) + V_0\delta(\tau_5) + V_0\big((2C_{55})\delta^2 + O(\delta^3)\big) \quad \text{(III.40)}$$

Finally, in case of fifth strain, the volume remains conserved and hexagonal symmetry of strained lattice is sustained. This situation can be represented by following relation:

$$\begin{pmatrix} (1+\delta)^{-\frac{1}{3}} & 0 & 0 \\ 0 & (1+\delta)^{-\frac{1}{3}} & 0 \\ 0 & 0 & (1+\delta)^{\frac{2}{3}} \end{pmatrix} \tag{III.41}$$

The energy for this strain can be written as:

$$E(V,\delta) = E(V_0,0) + V_0\left((C_{zz})\frac{\delta^2}{9} + O(\delta^3)\right) \tag{III.42}$$

Whereas, $C_{zz} = C_{11} + C_{12} + 2C_{33} - 4C_{13}$.

When the elastic constants are defined, the other important elastic quantities such as bulk and shear modulus can be determined easily. According to Voigt formula **[56]**, the bulk modulus (*B*) and the shear modulus (*G*) are given by the following relations:

$$B_{\mathrm{V}} = \frac{[2(C_{11}+C_{12}) + 4C_{13} + C_{33}]}{9} \tag{III.43}$$

$$G_{\mathrm{V}} = \frac{M + 12(C_{44}+C_{66})}{30} \tag{III.44}$$

Here, $M = C_{ZZ} = C_{11} + C_{12} + 2C_{33} - 4C_{13}$ and $C_{66} = \frac{1}{2}(C_{11} - C_{12})$.

From Reuss equation **[57]**, the bulk modulus (B) and shear modulus (G) are written in the form:

$$B_{\mathrm{R}} = \frac{C^2}{M} \tag{III.45}$$

$$G_{\mathrm{R}} = \frac{5}{2}\frac{C^2 C_{44} C_{66}}{3B_V C_{44} C_{66} + C^2(C_{44}+C_{66})} \tag{III.46}$$

Where: $C^2 = (C_{11} + C_{12})C_{33} - 2C_{13}^2$.

The average values can be given as **[58]**:

$$B_{\mathrm{H}} = \frac{1}{2}(B_{\mathrm{V}} + B_{\mathrm{R}}) \tag{III.47}$$

$$G_{\mathrm{H}} = \frac{1}{2}(G_{\mathrm{V}} + G_{\mathrm{R}}) \tag{III.48}$$

In addition, the Young modulus (E) and Poisson ratio (v) can also be calculated using the obtained results. These parameters are typically used to determine the hardness of polycrystalline materials. Following equations relate these variables with bulk modulus (B) and the shear modulus (G):

$$E = \frac{9BG}{3B + G} \tag{III.49}$$

$$\upsilon = \frac{3B - 2G}{2(3B + G)} \tag{III.50}$$

Table III.10 shows the calculated values of elastic constants (C_{11}, C_{12}, C_{13}, C_{33}, and C_{55}), bulk modulus (B), shear modulus (G), Young modulus (E), and Poisson ratio (v). Due to the absence of theoretical and experimental data for the examined ternary alloys, the derived elastic constants can be regarded as good predicted values for future work. The mechanical stability of a hexagonal crystal under isotropic pressure can be evaluated using Born stability criteria **[59]**:

$$C_{11} > |C_{12}|;\ 2C_{13}^2 < C_{33}(C_{11} + C_{12});\ C_{44} > 0 \tag{III.51}$$

The obtained results were verified using the above-mentioned equations. The results show that the stability conditions are satisfied and all examined materials are elastically stable in the hexagonal wurtzite structure. In addition, the brittleness and ductility of the materials can be studied using the ratio B/G suggested by Pugh **[60]**. Ductile materials are a type of material that can undergo significant plastic deformation without breaking or fracturing. Brittle materials are a class of materials that exhibit little or no plastic deformation before fracturing or breaking. According to Pugh, Materials with a B/G ratio larger than 1.75 are ductile, whereas Materials with B/G ratio less than 1.75 are considered brittle. We can see from table that we may consider ZnO and ZnTe as ductile while ZnS and ZnSe as brittle. Whereas all ZnOS ternary alloy are ductile. For the ZnOSe alloys, $ZnO_{0.75}Se_{0.25}$ is ductile, whereas $ZnO_{0.5}Se_{0.5}$ and $ZnO_{0.25}Se_{0.75}$ are brittle. Lastly in ZnOTe alloys, the ternary alloy $ZnO_{0.75}Te_{0.25}$ have ductile characteristic. But the rest of ternary alloys $ZnO_{0.5}Te_{0.5}$ and $ZnO_{0.25}Te_{0.75}$ are in brittleness nature.

The Poisson ratio v gives crucial information about the bond natural in the materials. Where a small Poisson's ratio indicates covalent bonding, the typical value of ionic materials is around of 0.25, whereas, for the metallic bonds it is approximately 0.33 **[61]**. As they shown in the **Table III.10**, the Poisson ratio values of the all studied materials are closely to 0.25, indicating the strong presence of ionic bond. This character of alloys can be also confirmed by the using *G/B* ratio, whereas the metallic materials have the value of 0.4, the ionic one's lake the value of 0.6, and the covalent materials obtained by the value of 1.1. The calculated values of *G/B* shown in table are closer to the value 0.6, meaning that the alloys are ionic semiconductors.

Figures III.22(a-c), shows the variation of the elastic constants C_{ij} as a function of the composition for the studied ternary alloy. The variation in elastic constants C_{ij} for $ZnO_{1-x}S_x$, $ZnO_{1-x}Se_x$ and $ZnO_{1-x}Te_x$ alloys is influenced by atomic size and bonding differences. For $ZnO_{1-x}S_x$, the elastic constants show a linear decrease with increasing 'S' composition due to the gradual and uniform substitution of 'S' for 'O', which weakens the lattice bonding consistently. In contrast, $ZnO_{1-x}Se_x$ and $ZnO_{1-x}Te_x$ alloys exhibit parabolic variation due to significant lattice distortions, non-linear atomic interactions, and local strain effects caused by the larger atomic sizes and different bonding characteristics of 'Se' and 'Te'. These non-linear changes can also be attributed to potential local clustering or phase separation, resulting in complex modifications to the overall mechanical properties of the alloys.

Table III.10 Elastic constants (GPa), Bulk modulus B (GPa), Shear modulus G (GPa), Young's modulus E (GPa) and Poisson's ratio υ ratio of $ZnO_{1-x}Y_x$ (Y=S, Se and Te) ternary alloys.

		C_{11}	C_{12}	C_{13}	C_{33}	C_{55}	B	G	B/G	G/B	E	v
ZnO	Pre.	293.31[a,b]	104.24[a,b]	73.55[a,b]	278.27[a,b]	54.63[a,b]	151.6[a,b]	78.04[a,b]	1.94[a,b]	0.52[a,b]	199.84[a,b]	0.28[a,b]
	Exp.	206[c]	117[c]	118[c]	211[c]	44[c]	-	-	-	-	-	-
	Theo.	201[d], 199.7[e]	124.49[d], 104.3[e]	119.57[d], 92.9[e]	235.38[d], 192[e]	34.73[d], 43.2[e]	151.02[d], 130.1[e]	49.8[e]	-	-	-	-
ZnS	Pre.	162.96	52	37.23	191.25	37.52	85.63	50.33	1.70	0.58	126.25	0.25
	Exp.	124[f]	60[f]	45[f]	140[f]	29[f]	-	-	-	-	-	-
	Theo.	125.7[e], 135.46[g]	52.86[e], 65.89[g]	47.5[e], 51.63[g]	135.2[e], 160.77[g]	33.6[e], 29.73[g]	75.8[e]	36.5[e]	-	-	-	-
ZnSe	Pre.	139.58[a]	40.36[a]	29.89[a]	133.5[a]	30.59[a]	68[a]	41.65[a]	1.63[a]	0.61[a]	103.76[a]	0.25[a]
	Exp.	-	-	-	-	-	-	-	-	-	-	-
	Theo.	116.9[e], 98.18[f]	37.4[e], 41.44[f]	37.9[e], 29.99[f]	115.3[e], 117.83[f]	28.7[e], 22.57[f]	63.9[e]	34.8[e]	-	-	-	-
ZnTe	Pre.	288.19[b]	97.81[b]	77.89[b]	273.32[b]	57.48[b]	150.55[b]	79.05[b]	1.90[b]	0.53[b]	201.84[b]	0.27[b]
	Exp.	-	-	-	-	-	-	-	-	-	-	-
	Theo.	-	-	-	-	-	-	-	-	-	-	-
$ZnO_{0.75}S_{0.25}$	Pre.	250.17	92.22	67.16	270.53	47.84	135.99	68.12	1.99	0.50	175.13	0.29
	Theo.	-	-	-	-	-	-	-	-	-	-	-
	Exp.	-	-	-	-	-	-	-	-	-	-	-
$ZnO_{0.5}S_{0.5}$	Pre.	220.66	77.41	54.83	238.73	44.08	117.13	62.14	1.88	0.53	158.41	0.28
	Theo.	-	-	-	-	-	-	-	-	-	-	-
	Exp.	-	-	-	-	-	-	-	-	-	-	-
$ZnO_{0.25}S_{0.75}$	Pre.	194.99	65.84	45.74	215.56	40.66	102.24	56.72	1.80	0.56	143.6	0.27
	Theo.	-	-	-	-	-	-	-	-	-	-	-
	Exp.	-	-	-	-	-	-	-	-	-	-	-
$ZnO_{0.75}Se_{0.25}$	Pre.	205.18[a]	69.56[a]	53.77[a]	234.61[a]	42.66[a]	110.98[a]	59.4[a]	1.87[a]	0.53[a]	151.23[a]	0.27[a]
	Theo.	-	-	-	-	-	-	-	-	-	-	-
	Exp.	-	-	-	-	-	-	-	-	-	-	-
$ZnO_{0.5}Se_{0.5}$	Pre.	82[a]	27.24[a]	17.17[a]	90.43[a]	19.08[a]	41.96[a]	25.18[a]	1.67[a]	0.59[a]	62.95[a]	0.25[a]
	Theo.	-	-	-	-	-	-	-	-	-	-	-
	Exp.	-	-	-	-	-	-	-	-	-	-	-
$ZnO_{0.25}Se_{0.75}$	Pre.	120.47[a]	34.14[a]	22.28[a]	139.42[a]	27.93[a]	59.73[a]	38.42[a]	1.55[a]	0.65[a]	94.91[a]	0.24[a]
	Theo.	-	-	-	-	-	-	-	-	-	-	-
	Exp.	-	-	-	-	-	-	-	-	-	-	-
$ZnO_{0.75}Te_{0.25}$	Pre.	168.40[b]	58.27[b]	39.08[b]	196.80[b]	35.00[b]	89.58[b]	49.24[b]	1.82[b]	0.55[b]	124.85[b]	0.26[b]
	Theo.	-	-	-	-	-	-	-	-	-	-	-
	Exp.	-	-	-	-	-	-	-	-	-	-	-
$ZnO_{0.5}Te_{0.5}$	Pre.	63.56[b]	18.87[b]	12.41[b]	82.73[b]	15.06[b]	32.94[b]	20.68[b]	1.59[b]	0.63[b]	51.30[b]	0.24[b]
	Theo.	-	-	-	-	-	-	-	-	-	-	-
	Exp.	-	-	-	-	-	-	-	-	-	-	-
$ZnO_{0.25}Te_{0.75}$	Pre.	113.46[b]	32.92[b]	21.42[b]	139.54[b]	26.25[b]	57.48[b]	36.38[b]	1.58[b]	0.63[b]	90.12[b]	0.23[b]
	Theo.	-	-	-	-	-	-	-	-	-	-	-
	Exp.	-	-	-	-	-	-	-	-	-	-	-

[a][8], [b][9], [c][62], [d][63], [e][64], [f][18], [g][20]

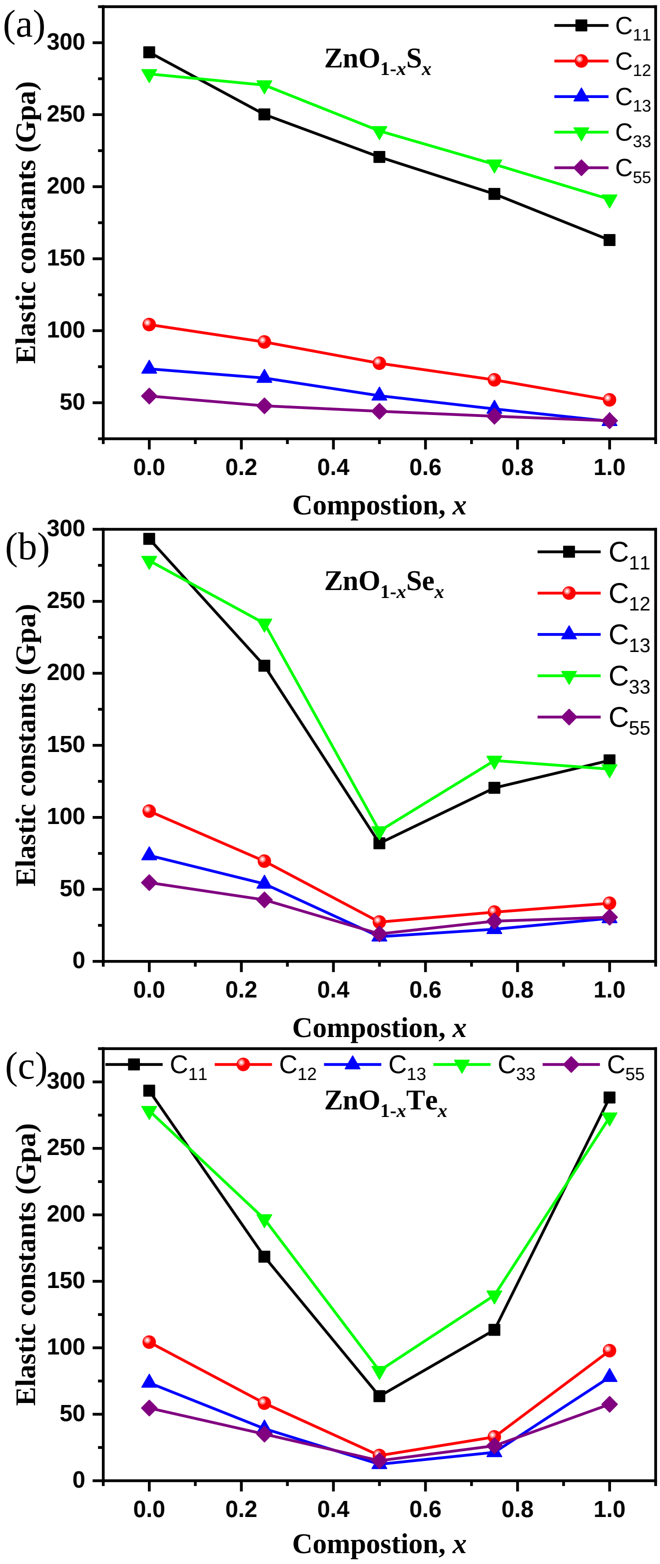

Figure III.22 Changes in the elastic constants as a function of the composition x of the $ZnO_{1-x}S_x$, $ZnO_{1-x}Se_x$ and $ZnO_{1-x}Te_x$ ternary alloys.

III.7 Conclusion

The structural, electronic, optical and elastic properties of wurtzite binary ZnO, ZnS, ZnSe and ZnTe compounds and their ternary $ZnO_{1-x}S_x$, $ZnO_{1-x}Se_x$ and $ZnO_{1-x}Te_x$ alloys have been investigated using the FP-LAPW method within the framework of DFT. The findings of the study can be summarized as follow:

• The computed lattice parameters of the binary compounds using the WC-GGA approximation is the closest to the available experimental and theoretical data.

• The lattice parameters of the ternary alloys exhibit a small deviation from Vegard's law.

• All studied materials are direct bandgap semiconductors.

• The refractive index, reflectivity and absorption coefficient of the ternary alloys shift toward lower energies with increase in composition x.

• The stability conditions for all studied materials are satisfied and they are elastically stable in the hexagonal wurtzite structure.

III.8 References

[1] P Blaha et al., **Comput. Phys. Commun.** 59 (2), 399 (1990).
[2] K Schwarz and P Blaha, **Comput. Mater. Sci.** 28 (2), 259 (2003).
[3] P Blaha et al., **J. Chem. Phys.** 152 (7) (2020).
[4] P Hohenberg and W Kohn, **Phys. Rev.** 136 (3B), B864 (1964).
[5] JP Perdew et al., **Phys. Rev. Lett.** 77 (18), 3865 (1996).
[6] Z Wu and RE Cohen, **Phys. Rev. B** 73 (23), 235116 (2006).
[7] F Tran and P Blaha, **Phys. Rev. Lett.** 102 (22), 226401 (2009).
[8] Y Djalab et al., **J. Mater. Res.** 38 (3), 799 (2023).
[9] R Moussa et al., **Current Applied Physics** 55, 82 (2023).
[10] FD Murnaghan, **American Journal of Mathematics** 59 (2), 235 (1937).
[11] F Birch, **Phys. Rev.** 71 (11), 809 (1947).
[12] N Tit et al., **J. Electron. Mater.** 41 (11), 3111 (2012).
[13] H Karzel et al., **Phys. Rev. B** 53 (17), 11425 (1996).
[14] F Decremps et al., **Phys. Rev. B** 68 (10), 104101 (2003).
[15] A Djelal et al., **Superlattices Microstruct.** 109, 81 (2017).
[16] R John and S Padmavathi, **Cryst. struct. theory appl** 5 (02), 24 (2016).
[17] RR Reeber and GW Powell, **J. Appl. Phys.** 38 (4), 1531 (2004).
[18] S Desgreniers et al., **Phys. Rev. B** 61 (13), 8726 (2000).
[19] EH Kisi and MM Elcombe, **Acta Crystallogr. C** 45 (12), 1867 (1989).
[20] S Ferahtia et al., **Superlattices Microstruct.** 67, 88 (2014).
[21] Z Nourbakhsh, **J. Alloys Compd.** 505 (2), 698 (2010).
[22] O Zakharov et al., **Phys. Rev. B** 50 (15), 10780 (1994).
[23] SZ Karazhanov et al., **Phys. Rev. B** 75 (15), 155104 (2007).
[24] SK Yadav et al., **Phys. Rev. B** 81 (14), 144120 (2010).
[25] J-H Yang et al., **Phys. Rev. B** 79 (24), 245202 (2009).
[26] P Karil et al., **Mater. Today: Proc.** 54, 782 (2022).
[27] S Shabbir et al., **Mater. Sci. Semicond. Process.** 121, 105326 (2021).
[28] G Baldissera and C Persson, **J. Appl. Phys.** 119 (4) (2016).
[29] L Vegard, **Z. Phys.** 5 (1), 17 (1921).
[30] V Srikant and DR Clarke, **J. Appl. Phys.** 83 (10), 5447 (1998).
[31] O Madelung, *Semiconductors: Data Handbook*. (Springer Berlin Heidelberg, 2012).
[32] O Madelung et al., 1999 (unpublished).
[33] SD Kshirsagar et al., **Mater. Sci. Semicond. Process.** 16 (3), 1002 (2013).
[34] M Aazi et al., presented at the 2019 7th International Renewable and Sustainable Energy Conference (IRSEC), 2019 (unpublished).
[35] BK Meyer et al., **Phys. Status Solidi C** 1 (4), 694 (2004).
[36] R Kudrawiec and W Walukiewicz, **J. Appl. Phys.** 126 (14) (2019).
[37] A Belabbes et al., **J. Phys.: Condens. Matter** 19 (45), 456212 (2007).
[38] M Sargolzaei et al., **J. Appl. Phys.** 109 (7) (2011).
[39] C Ambrosch-Draxl and JO Sofo, **Comput. Phys. Commun.** 175 (1), 1 (2006).
[40] M O'Donnell et al., **J. Acoust. Soc. Am.** 69 (3), 696 (1981).
[41] M Fox, *Optical Properties of Solids*. (Oxford University Press, 2001).
[42] SK Tripathy, **Opt. Mater.** 46, 240 (2015).
[43] NM Ravindra et al., **Phys. Status Solidi B** 93 (2), K155 (1979).
[44] D Komaraiah et al., **Mod Res Catal** 5 (4), 130 (2016).
[45] A Baizid et al., **Comput. Condens. Matte** 27, e00558 (2021).
[46] S Shabbir et al., **Optik** 206, 164285 (2020).
[47] S Adachi, *Handbook on Physical Properties of Semiconductors*. (Springer US, 2004).

[48] SA Saoucha et al., **Solid State Commun.** 354, 114897 (2022).
[49] MF Hasaneen et al., **Mater. Res. Express.** 7 (1), 016422 (2020).
[50] T Hattori et al., **Opt. Commun.** 7 (3), 229 (1973).
[51] S Hussain et al., **Mater. Today Commun.** 21, 100672 (2019).
[52] W Benstaali et al., **Mater. Sci. Semicond. Process.** 16 (2), 231 (2013).
[53] J Morteza, *Hex-elastic*. (2013).
[54] LD Landau et al., *Theory of Elasticity: Volume 7*. (Elsevier Science, 1986).
[55] L Fast et al., **Phys. Rev. B** 51 (24), 17431 (1995).
[56] W Voigt, *Lehrbuch der kristallphysik (mit ausschluss der kristalloptik)*, Nachdruck der ersten Aufl. ed. (B.G. Teubner, [J.W. Edwards] Leipzig, Berlin, Leipzig, Berlin, 1928).
[57] A Reuss, **Z Angew Math Mech** 9 (1), 49 (1929).
[58] R Hill, **Proc. Phys. Soc. A** 65 (5), 349 (1952).
[59] M Born and K Huang, *Dynamical Theory of Crystal Lattices*. (Clarendon Press, 1962).
[60] SF Pugh, **Lond. Edinb. Dublin philos. mag. j. sci.** 45 (367), 823 (1954).
[61] J Haines et al., **Annu. Rev. Mater. Res.** 31 (1), 1 (2001).
[62] G Carlotti et al., **J. Phys.: Condens. Matter** 7 (48), 9147 (1995).
[63] F Wang et al., **J. Alloys Compd.** 597, 50 (2014).
[64] LA Valdez et al., **J. Phys. Chem. Solids** 134, 245 (2019).

General conclusion

In this thesis, we carried out a theoretical study on the structural, electronic, optical and elastic properties of the ternary alloys $ZnO_{1-x}S_x$, $ZnO_{1-x}Se_x$ and $ZnO_{1-x}Te_x$ as well as their binary constituents ZnO, ZnS, ZnSe and ZnTe. This study has been done in the so-called wurtzite crystal structure. The calculations were carried out using the ab-initio method of full potential linearized augmented plane waves (FP-LAPW) which is based on the formalization of density functional theory (DFT). Our work is divided into four parts. Where in each part we study a different physical property of the binary and ternary compounds.

The first main step of this work is devoted to the determination of the equilibrium structural properties where the lattice parameters, the bulk modulus and its derivative with respect to the pressure were obtained from the Birch-Murnaghan equation of state. We calculated these parameters using three different approximations. The results obtained show that the lattice parameters of the wurtzite ternary alloys $ZnO_{1-x}S_x$, $ZnO_{1-x}Se_x$ and $ZnO_{1-x}Te_x$ varied in a linear way as a function of the composition with small deviation in some compounds. While the bulk modulus of these alloys shows quadratic variation with respect to the composition. Moreover, for binary compounds, we compared these results with other theoretical and experimental studies available in the literature. However, for ternary alloys, there is a lack of data and our results are predictive and can serve as a reference for future work.

The second part of this work is devoted to the calculations of the electronic properties of the different alloys with their binary constituents. We have calculated the band structure and electronic density of state (DOS) of the materials under consideration. The gap energy, which was computed using the more recent TB-mBJ approach, is the most important property in this step; where significant improvement of its value was noticed using the aforementioned approach. All the materials under study exhibit a direct transition ($\Gamma\rightarrow\Gamma$) along the high symmetry point Γ. The bowing parameter which is corresponds to the deviation of gap energy from linearity, increases with the increase in the electronegativity difference between atoms.

In the third step, we calculated the optical properties of the studied semiconductors. The dielectric function and refractive index are determined using the (FP-LAPW) method compared with other theoretical and empirical models widely used in the calculation of optical properties. For binary compounds, the results are in very good agreement with other experimental work encountered in the literature. And once again, we notice a lack of data in the case of ternary alloys.

The final step of this study involves calculating the elastic properties of the ternary alloys $ZnO_{1-x}S_x$, $ZnO_{1-x}Se_x$ and $ZnO_{1-x}Te_x$ and their binary constituents. The stability conditions for all studied materials are satisfied and they are elastically stable in the (hexagonal) wurtzite structure. We notice some discrepancies between the results found and other data from literatures in the case of binary compounds. While in the case of ternary alloys, there is no data to compare our calculations with it.

We were able to gain a general understanding of the investigated properties of these alloys thanks to this investigation. As a result, this work will undoubtedly make a significant contribution to the literature because there is a lack of experimental data pertaining to these alloys.

Annex 1:

Scientific production

- **Yacine Djalab**, Rabah Moussa, Mostefa Maache, Syed Awais Rouf, Ahmed Abdiche, Rabah Khenata, and Fethi Soyalp, *Theoretical Investigations of Structural, Electronic, Optical and Elastic Properties of Wurtzite* $ZnO_{1-x}Se_x$ *Ternary Alloys Using First Principle Method*, Journal of Materials Research 38 (2022) 799–813.

- Rabah Moussa, **Yacine Djalab**, Mostefa Maache, Rabah Khenata, Saad Bin-Omran, Syed Awais Rouf, Muhammad Waqas Iqbal, Ahmed Abdiche, Waleed Ahmed, and Mumtaz Manzour, *An Investigation Using DFT Methods on the Electronic and Optical Properties, and Mechanical Behavior of the Wurtzite* $ZnO_{1-x}Te_x$ *Ternary Alloy.*
Current Applied Physics 55 (2023) 82–92.

Annex 2:

National and international communications

- **Yacine Djalab**, Rabah Moussa, Mostafa Maache, Yazid Benbouzid, Abderrazak Djenidi and Loumafak Hafaifa, *Theoretical prediction of physical and chemical properties of the* $ZnO_{1-x}Se_x$ *ternary alloy*, 1st international conference on chemical matters and environment preservation IC-CMEP'22 March 09-10, 2022, Ouargla-Algeria.

- Rabah Moussa, **Yacine Djalab**, Mostefa Maache and Rabah Khenata, *Fundamental physical properties of the wurtzite* $ZnO_{1-x}Te_x$ *ternary alloy: A first principle study*, The First National Conference Of Materials Sciences And Renewable Energy CMSRE23 November 22-23, 2023, Relizane, Algeria.

- **Yacine Djalab**, Rabah Moussa, Mostafa Maache and Mohamed Kharroubi, *Ab-initio study on the structural and electronic properties of the* $ZnO_{1-x}S_x$ *ternary alloys*, The first National Conference on Matter Sciences NCSM2023 December 20, 2023, Djelfa, Algeria.